Electronic Thesis and Dissertation Repository

9-28-2015 12:00 AM

Optimization of Cu2ZnSnS4 Nanocrystal Composition and Thin Film Fabrication for Photovoltaic Applications

Saghar Khoshmashrab
The University of Western Ontario

Supervisor
Dr. Zhifeng Ding
The University of Western Ontario

Graduate Program in Chemistry
A thesis submitted in partial fulfillment of the requirements for the degree in Master of Science
© Saghar Khoshmashrab 2015

Follow this and additional works at: https://ir.lib.uwo.ca/etd

Part of the Analytical Chemistry Commons

Recommended Citation

Optimization of Cu$_2$ZnSnS$_4$ Nanocrystal Composition and Thin Film Fabrication for Photovoltaic Applications

Monograph

by

Saghar <u>Khoshmashrab</u>

Graduate Program in Chemistry

A thesis submitted in partial fulfillment
of the requirements for the degree of
Master of Science

The School of Graduate and Postdoctoral Studies
The University of Western Ontario
London, Ontario, Canada

Abstract

In this work Cu_2ZnSnS_4 (CZTS) nanocrystals (NCs) were prepared via a solvothermal, one-pot method. Given that the composition affects the electronic properties of this p-type semiconductor, comparative compositional analysis was done from various designed and synthesized analogues. EXAFS studies indicated that the stoichiometries with lower Cu-contents (Cu/Sn+Zn <1) contained a more conserved crystal structure vs. the compositions with higher Cu concentrations.

The effects of Cu were further studied, using Cu-poor and Cu-stoichiometric NCs. This time the precursor content of Zn was also increased to yield samples with Zn rich compositions. NCs in which the Cu concentration was below stoichiometric ($Cu_{1.8}Zn_{1.1}Sn_{1.0}S_{4.8}$) were more crystalline and yielded a higher photoresponse (~53 $\mu A/cm^2$).

The compositionally optimized CZTS NCs were then deposited using four experimental approaches to yield CZTS thin films: (1) drop cast, (2) joule heating, (3) dip coating and (4) spin coating. The depositions were carried out on FTO and Mo-coated substrates. Comparably, films fabricated using the spin coat method, consistently exhibited a good photoresponse (FTO=69-75 $\mu A/cm^2$, Mo=60-77 $\mu A/cm^2$), along with smoother surfaces with less carrier traps. The NCs deposited in this manner were further used for device fabrication. The preliminary results of the final device yielded a low efficiency indicating that optimization of the processes post-deposition, are required.

Keywords

Co-Authorship Statement

This thesis contains the work of one published manuscript, which is found in Chapter 3.

S. Khoshmashrab, M.J. Turnbull, D. Vaccarello, Y. Nie, S. Martin, D.A. Love, P.K. Lau, X. Sun , Z. Ding (2015). The experimental approach was proposed by SK, DAL and ZD. Experimental design proposed by SK and ZD. Synthesis was performed by SK and MJT. Electrochemical studies were performed by SK and SM. Raman and UV-Vis studies were done by SK and DV. Selected area electron diffraction was performed by YN, PKL and XS. Data analysis and manuscript written by SK. The manuscript was edited by MJT, DV and ZD and finalized by ZD.

Acknowledgments

First and foremost I would like to thank my supervisor, Dr. Zhifeng Ding for his invaluable guidance, patience and support throughout my research. His suggestions and insightful ideas for the past two years, allowed me to complete my project. His dedication towards research has truly been inspiring.

I would like to express my sincere gratitude to all of my colleagues, specifically Daniel Vaccarello, Amy Tapley, Michelle Li, Mathew J. Turnbull, Fraser Filice and Mahdi Hesari, for their expertise and endless encouragement. You all created a helpful and positive environment that kept me motivated

To my best friends, Dalia, Diana, Adriana and Zena, thank you for being emotionally present during my absence and for always being by my side.

I truly thank my parents, brother and of course Hisham for being a foundation of love, support and strength, not just for the past two years but throughout my life and career. Without your presence, the completion of this thesis would not be possible. This dissertation is as much yours as it is mine.

Table of Contents

List of Tables

List of Figures

List of Abbreviations

AC	Alternating Current
ALD	Atomic Layer Deposition
AM1.5	Air Mass 1.5 (corresponds to the standard solar spectrum)
AZO	Aluminum-doped ZnO
CB	Conduction Band
CdTe	Cadmium Telluride
Chrono	Chronoamperometry
CIGS	$CuInGaS_2$
CIS	$CuInS_2$
CZTS	Cu_2ZnSnS_4
CZTSe	$Cu_2ZnSnSe_4$
DC	Direct Current
ED	Energy Dispersive
EDX	Energy-dispersive X-ray Spectroscopy
EG	Ethylene Glycol
EXAFS	Extended X-ray Absorption Fine Structure
FF	Fill Factor
FTO	Fluorine-doped Tin Oxide
HRTEM	High Resolution Transmission Electron Microscopy
i:ZnO	Intrinsic ZnO
IMPS	Intensity Modulated Photocurrent Spectroscopy

IV	Current-Voltage
MPP	2-mercapto-5-n-propylpyrimdine
NC(s)	Nanocrystal(s)
p-n	p-type and n-type
PEC	Photoelectrochemical
PED	Pulsed Electron Deposition
PV	Photovoltaic
SAED	Selected Area Electron Diffraction
SCE	Saturated Calomel Electrode
SCR	Space Charge Region
SEM	Scanning Electron Microscopy
TEM	Transmission Electron Microscopy
VB	Valence Band
XAFS	X-ray Absorption Fine Structure
XANES	X-ray Absorption Near Edge Structure
XAS	X-ray Absorption Spectroscopy
XRD	X-Ray Diffraction
XRF	X-Ray Fluorescence

List of Symbols

2θ	Scattering angle
A	Ampere
a, b, c	Crystal unit cell parameters
C	Capacitance
Cu_{zn}	Occupation of Cu at the Zn site
d	Distance
e^-	Electron
E_g	Band gap
Ev	Electron volt
F	Faraday constant
g_1	Flux of minority carriers
h^+	Hole
hv	Photon energy
I	Intensity of transmitted X-ray
I_0	Incident intensity
I_{sc}	Short-circuit current
J	Current density
J_{sc}	Short-circuit current density
k	Magnitude of the photoelectron wave vector
k_{ps}	Rate of charge separation
k_{rec}	Rate of recombination
$K\alpha, K\beta$	Characteristic X-ray emission lines

R	Resistance (Chapter 3)
R	Distance (Chapter 2)
R_s	Solution resistance
R_{sh}	Shunt resistance
$sccm$	Standard cubic centimeters per minute
Sn_{Zn}	Occupation of Sn on a Zn site
V	Voltage
V_{Cu}	Vacancy at the Cu site
V_{oc}	Open-circuit potential
Zn_{Cu}	Occupation of Zn at the Cu site
α	Absorption coefficient
η	Power conversion efficiency
θ	Bragg diffraction angle
λ	Wavelength
μ	Linear absorption coefficient
σ	Debye-Waller factor
χ	EXAFS interference function
ω	Angular frequency

xvi

Chapter 1. Introduction

Solar cells have become one of the most promising sources of renewable energy; however, one of the most challenging tasks has been the development of cost-effective, non-toxic, efficient devices via a low energy and waste procedural method. This thesis will focus on addressing these challenges by synthesizing Cu_2ZnSnS_4 (CZTS) light absorbing layers via a solvothermal, one-pot method in the absence of toxic solvents. CZTS is an abundant, non-toxic quaternary semiconductor with a high absorption coefficient ($10^4\,cm^{-1}$) and a direct energy band gap of ~1.5 eV, which is in alignment with the solar spectrum.[1-3] These properties among others make them ideal candidates for device applications.

1.1. Solar Energy

Currently, the primary source of energy arises from the use of fossil fuels, which are limited. As the world's energy consumption increases, the consequences associated with the use of petroleum, coals and gases become of greater concern. Our dependency on these non-renewable resources also has an economic impact as imports create reliance and further inflate costs. Their uses have caused various adverse effects, such as greenhouse gas emissions, water pollutants and acid rain, to list a few. Numerous international policies have been implemented to stimulate the development of green technologies for environmental protection, as long term use of these developments will reduce environmental damage.[4-5] For instance, the Kyoto Protocol was created to reduce global pollution. All of its members committed to decrease their production of greenhouse gas emissions by 18% below 1990 levels (62 Mt of CO_2 emissions per capita), by the year 2020.[6-8]

The long-term solution is to use cleaner sources of energy such as hydropower, geothermal, wind and solar, to list a few. These renewable sources of energy are beneficial as they allow a society to be more independent and less reliant on imports. This introduces energy security as the required energy is generated on site and the source of energy is unlimited. Further, they can reduce the consumption of non-renewable resources, by generating and storing energy.

Among these sources, solar radiation is of particular interest, as it currently supplies the earth with 10,000 times more energy than is consumed yearly.[9] In theory, that would

mean that if 0.1% of the Earth's surface were covered with solar cells that contained an efficiency of 10%, the current energy needs of the population would be satisfied.[8] Solar energy is abundant, environmentally friendly and a sustainable resource. Solar power can be generally divided into two categories: thermal and electrical.[10] Thermal refers to the use of sunlight to produce heat; this can be collected using mirrors or dishes, which focus light and convert it into heat. Electrical energy, uses photovoltaic (PV) devices to convert light energy into electrical. This has wide applications, as approximately 30% of produced energy is consumed via electricity.[11]

PVs have become one of the most promising sources of renewable energy, as they are inexhaustible. The only issue that remains is that current PVs have not been able to compete with fossil fuels due to their high production costs, low efficiencies and the presence of some toxic compounds within their materials.[12-15] As a result, the only challenge that persists is the development of cost-effective, non-toxic, efficient devices via low energy and waste procedural methods. In Canada alone it is expected that electricity consumption is to grow at a rate of 1.5 to 2%, annually;[16] in turn, the demand for cheap and efficient PV systems is the focus of many sectors.

1.2. Theory Behind Photovoltaic Cells

1.2.1. Semiconductor Materials

The most common PV devices are made from semiconductor materials in which enable the conversion of sunlight to electrical energy. As shown in Figure 1.1, semiconductors exist in three forms: intrinsic, p-type and n-type.[17] Intrinsic (i-type) semiconductors are pure enough that impurities do not appreciably affect their electrical behavior, an example being silicon. It contains an equal number of electrons and holes.
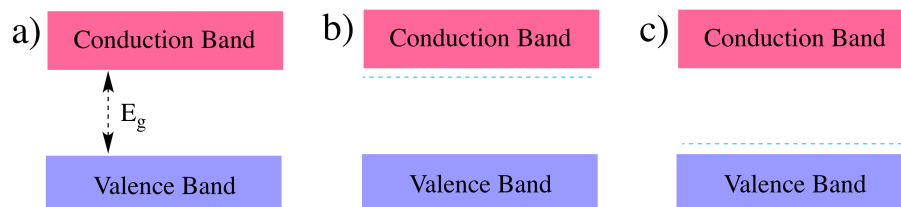
Figure 1.1. The band structures of the three different semiconductors (a) i-type, (b) n-type and (c) p-type.

It simply consists of a valence band (VB) and a conduction band (CB) with no other energy levels in between (Figure 1.1 (a)). The VB is the energy level in which the electron is bound and when promoted to the CB it is considered to be in a free state. The region in between the VB and CB is termed the energy band gap (E_g), which is the minimum change in energy that is required to excite an electron from the VB to the CB.

An n-type semiconductor is doped with impurity atoms in order increase the materials conductivity via the addition of an extra energy level (Figure 1.1 (b)). Specifically, extra electrons are introduced in the material via electron donor dopants; an example would be Cr-doped CdS.[18] This introduces an extra electron energy level near the CB to allow for easier promotion of electrons to the CB. Lastly, a p-type semiconductor is doped with acceptor impurities (Figure 1.1 (c)). The additional empty energy level is near the VB, lowering the energy required for electrons to be excited from the VB.

1.2.2. p-n Junctions in Semiconductors

The first step required for the production of majority of solar devices is via contact of a p-type and an n-type semiconductor, to form what is called a p-n juntion (Figure 1.2).[19] As shown a p-type semiconductor is electron poor while an n-type semiconductor is electron rich (Figure 1.2 (a)). The different charges allows for greater conductivity within the material as it creates charge mobility. The fact that the charges are able to move freely permits them to carry an electrical current.

Upon contact, electrons diffuse from the n-type to the p-type semiconductor (Figure 1.2 (a)). This creates a region at the interface called the space charge region (SCR), in which the n-type semiconductor is electron poor and the p-type is electron rich (Figure 1.2 (b)). At this point an electric field exists across the SCR due to the charge separation. When photons from light strike the surface of the PV cell a mobile electron-hole pair is generated (Figure 1.2 (c)). The electric field causes the electron to diffuse to the n-type semiconductor and the hole to "flow" to the p-type semiconductor, resulting in a potential difference or voltage. Once the cell is connected to an external circuit the holes and electrons driven around the circuit can form a current.
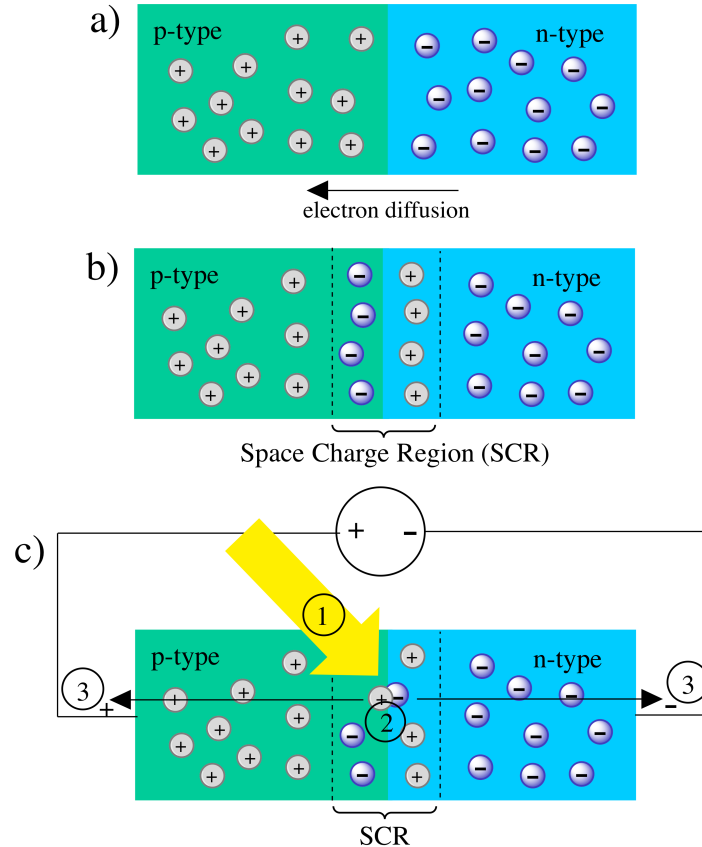
Figure 1.2. The p-n junction in a solar cell (a) p-type and n-type semiconductor after contact, (b) the formation of the space charge region (SCR), (c) upon light exposure ① an electron hole pair is formed ② and when a potential is applied the electron and hole are separated ③.

1.3. Three Generations of Photovoltaic Devices

There exists a large scale of semiconductor materials suitable for the production of solar cells. The difference in material largely affects the overall cost and efficiency of the device. PV devices can be classified into three generations. The first are based on crystalline silicon, which is currently the dominant solar cell technology. The cost of crystalline silicon is considered relatively high, primarily because of the energy-intensive processes required for its production. An essential step in its fabrication requires heating of the material at 1500°C, to ensure purity.[20] Furthermore, the required thickness of the material (200 - 250 μm) adds an additional cost to the device. Although the efficiency has reached 25.6%[21], the heavy weight of the material results in a final cost of $3.40/W, after installation and labor fees.[22] This is double the initial cost of just the material ($1.70/W).[22]

The production of second generation solar cells were introduced to overcome the cost of the first generation. These are based on thin film materials, the most common being: amorphous silicon, $CuInGaS_2$ (CIGS) and CdTe. They have reached efficiencies of 10.2%, 21.7%, 21.0%, respectively.[21, 23] While thin films are only a few micrometers thick, they can achieve similar efficiencies as ones seen for crystalline silicon. It is important to note that the theoretical efficiency of a solar cell with a single p-n junction is limited to 33.7%, according to the Shockley-Queisser limit.[24] This is primarily due to three reasons: the first being that some of the energy of photons is lost when their energy is greater than the band gap of the semiconductor, the second is due to the loss of photons that contain a lower energy than the band gap of the PV material and the third refers to recombination losses. The calculated maximum limit corresponds to a semiconductor with an energy band gap of 1.4 eV.

Third generation solar cells were created to overcome the Shockley-Queisser limit and further increase the efficiency of PVs. These are commonly known as multijunction solar cells. They use a combination of thin films, such as GaInP/GaAs/Ge,[25] in order to utilize the multiple band gaps present in the different absorbing layers such that the device can absorb photons of various energies. The p-n junctions of these materials are electrically connected in series; therefore appropriate bandgaps are selected to ensure similar currents are generated.[26] It is important to note that these PVs continue to use scarce/toxic elements. The fabrication costs of these solar cells are estimated to be $5-8/cm^2.[27] Although the current world record efficiency for multijunction devices is 43%, the cost has made them uneconomical for mass production.[27-28]

1.4. Cu_2ZnSnS_4 Thin Film Solar Cells

1.4.1. Properties and Overview

Second generation thin films have shown to be a cheap alternative to first generation solar cells, with comparable efficiencies. As previously indicated CIGS thin films are one of the most commonly used second-generation solar cells. Their large-scale commercialization has been limited to their high cost and scarce availability of In and Ga; in turn, increasing research interests have been dedicated towards the production of thin films made with earth-abundant materials.

Since the late 2000s, $Cu_2ZnSn(S,Se)_4$ (CZTS/CZTSe) light absorbing thin films (1-2 μm thick) have drawn great attention, as they are composed of elements richly distributed in

the earth's crust.[29] Derived from CIGS, the group III elements, In and Ga, are substituted with Zn and Sn, generating I_2-II-IV-VI_4 CZTS. These low cost, non-toxic elements were an attractive alternative to the former. Further, their ideal properties made them promising materials for photovoltaic applications.

CZTS/CZTSe are quaternary chalcogenide p-type semiconductors that have a high absorption coefficient of 10^4 cm^{-1}; allowing 90% absorption of the incident light.[1-3] The ground-state structure consists of alternating Cu/Zn and Cu/Sn layers with S atoms coordinated in between.[30] CZTS and CZTSe contain a band gap of approximately 1.5 eV and 0.9 eV, respectively.[1-3, 31] From an environmental view the use of CZTS is preferable over CZTSe, due to the absence of Se. The higher band gap also makes it a more desirable option.

The schematic diagram of the layers of a full device is shown in Figure 1.3. The absorbing layer can be deposited on various conductive coated substrates such as fluorine-doped tin oxide (FTO), indium-doped tin oxide (ITO) or Molybdenum. These coatings provide an electrical contact with the CZTS layer. The n-type semiconductor of the device consists of a buffer layer and a window layer. The CdS is an n-type buffer layer, which is usually deposited by a chemical bath deposition method.[32-34] ZnO and aluminum-doped zinc oxide (ZnO:Al) are n-type window layers and are commonly deposited by sputtering.[35-37] The Photovoltaic (PV) effect, which is the phenomenon that occurs after light strikes a film and causes current to flow in one direction, takes place between the CZTS and n-type junction.[38]

Front contact
AZO (100-150 nm)
ZnO (50 nm)
CdS (50 nm)
CZTS (1-2 μm)
Back contact
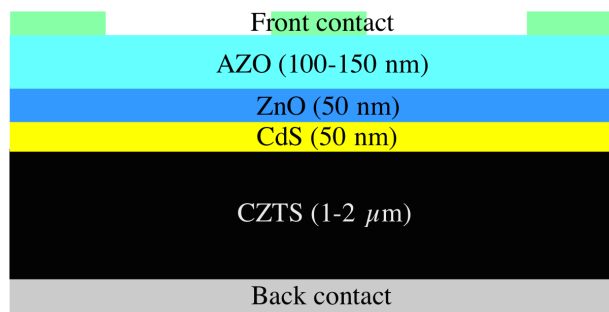
Figure 1.3. Layers of a CZTS solar cell device.

1.4.2. History of Cu$_2$ZnSnS$_4$ Devices

The first report of the photovoltaic properties of CZTS was in 1988 by Ito and Nakazawa, whom fabricated the thin film via sputtering.[39] The device demonstrated an open-circuit voltage (Voc) of 165 mV, confirming its PV effects. Thereafter, increasing research led to a series of improvements in the device. Katagari and coworkers did extensive work which lead to an initial device efficiency of 2.62%[40] in 2001, 5.45%[41] in 2003 and 6.7%[42] in 2008. Their highest performing device (2008) was deposited on Mo-coated glass and consisted of CdS as the n-type buffer layer and ZnO:Al as the window region. The films were prepared via an initial sputtering of the precursors, followed by thermal sulfurization at 580°C for 3 hrs.

In recent years Solar Frontier announced device efficiencies of 9.7%,[43] 11.1%[44] and 12.6%[15] in 2010, 2012 and 2013, respectively. The fabrication of the films were done using a non-vacuum based approach. The authors used a hydrazine pure-solution to spin coat the samples onto an Mo-coated glass. The samples, comprising of Se and S were annealed at 500°C to fabricate Cu$_2$ZnSn(Se,S)$_4$.

Overall, both vacuum and non-vacuum based techniques have been used to fabricate high quality CZTS films. In comparison, the fabrication using the latter has demonstrated to be more cost effective and less energy intensive. To date, the highest efficiency CZTS devices have used non-vacuum based approaches. These are generally known as solution based fabrication techniques,[45] some of which include: spray pyrolysis,[46] electro- and photo-chemical deposition,[47-48] sol-gel technique,[49] spin-coating method[50] and electrodeposition.[51]

1.5. Aims and Objectives of This Thesis

Despite the recent advancements, CZTS devices remain commercially unavailable primarily due to long durations of high temperature treatments (400°C – 550°C) and/or the use of toxic solvents for their synthesis. The aim of this work has focused on synthesizing CZTS light absorbing layers via a solvothermal, one-pot method without the use of toxic solvents and at atmospheric pressure. The goal is to maintain a low fabrication cost in which is non-energy intensive to make it an attractive option for mass production. Ultimately, the successful development of a working device would not only be a cheap and viable breakthrough for second generation solar cells but also the third generation, as it could be used in multi-junction devices.

The objectives of this work were to: (1) determine the effects of composition/stoichiometry on CZTS crystallinity and overall film quality; (2) Use electrochemical measurements to characterize compositional differences and further provide kinetic information based on variations; (3) Investigate non-vacuum based techniques to produce a film of uniform composition while maintaining a cost effective procedure; (4) Fabricate a device using the most ideal deposition method and determine its optoelectronic properties.

1.6. Techniques for CZTS Characterization

1.6.1. Photoelectrochemical Measurements

Electrochemical measurements are frequently used for the study of chemical systems. These systems involve the transfer of charge across the interface of an ionic conductor and an electrical conductor.[52] Ionic conductors involve solutions containing electrolytes and materials typically used as electrical conductors include metals and semiconductors. Generally in an electrochemical cell, two electrodes are immersed in solution and then connected to an external circuit. When sufficient potential is applied, electrons flow at the solid/solution interface, creating a current. In photoelectrochemical (PEC) experiments, the current produced is referred to as 'photocurrent' due to the fact that light is used to irradiate the electronic conductor. Essentially, the light is converted to electrical and chemical energy.

A typical three-electrode PEC set-up includes a working, counter and reference electrode. The working electrode is the reaction site; in our case it would refer to the CZTS thin film. The reference electrode contains a known potential; therefore the potential of the working electrode is defined with respect to the reference. The reference electrode used in our PEC studies was the saturated calomel electrode (SCE), due the fact that it is not photoactive. The counter (or auxiliary) electrode is the site in which the electrons transfer to, from the working electrode. This flow of current completes the cell circuit. The auxiliary electrode predominantly used is pt. This was also used in our measurements because of its stability in the electrolyte solution and more importantly its large surface area, permitting it to support the current produced.

1.6.2. Intensity Modulated Photocurrent Spectroscopy

Intensity modulated photocurrent spectroscopy (IMPS) is a complementary technique

to PEC measurements as it provides information on the kinetics of the charge transfer taking place at the semiconductor/solution interface. The effect of electron-hole recombination can also be quantitatively determined via IMPS. This technique involves the AC modulation of the incident light at a constant potential. The periodic changes of the photocurrent response are then measured with respect to a wide range of frequencies.

1.6.3. Current-Voltage Measurements

The efficiency of a PV device is determined using current-voltage (IV) measurements. Upon connection of the electrodes to the top and bottom contacts, the voltage is varied while the output current is measured. The power conversion efficiency (abbreviated as **η**) of a solar cell is defined as the ratio of the output power (P_{out}) also known as the maximum power output (P_{max}), to the input power (P_{in})[53],

$$\eta = \frac{P_{max}}{P_{in}}$$

P_{in} is the incident light intensity, under standard test conditions this is measured as 100 mW/cm^2 (1 sun, AM1.5G). The quality of the device can also be determined using what is known as Fill Factor (FF)[54],

$$FF = \frac{I_{mp} \text{x} V_{mp}}{I_{sc} \text{x} V_{oc}}$$

The current and voltage at P_{max} are denoted as I_{mp} and V_{mp}, respectively. I_{sc} is the short-circuit current (current when voltage=0) and V_{oc} corresponds to the open-circuit voltage (voltage when current=0). As will be discussed in Chapter 4, these parameters among others influence the overall conversion efficiency of a PV device.

1.6.4. Scanning Electron Microscopy

Scanning Electron Microscopy (SEM) is a technique whereby samples are magnified and visualized in situ. The way it works is via the use of electrons. An incident beam of electrons hits the sample of interest and generates a signal, produced by secondary electrons, backscattered electrons or X-rays. Secondary electrons are formed when electrons from the beam collide with an atoms valence electrons, causing them to be ejected and consequently detected. The information is used to form an image of the surface features and morphology. Backscattering occurs when the initial electrons from the incident beam are reflected off from deeper within and the surface of the sample. These provide the topographical contrast

of an image.

1.6.5. Energy-Dispersive X-ray Spectroscopy and X-ray Fluorescence

Energy-dispersive X-ray spectroscopy (EDX) is typically integrated into SEM. X-rays are produced when the incident beam strikes an inner electron of an atom and creates a vacancy. This creates instability within the atom and as a result an electron from an outer shell falls to a lower energy level, filling the vacancy. The energy transition from the outer to the inner shell is characteristic of a certain element. The difference between the two binding energies is given off as an X-ray, which is then detected. X-ray Fluorescence (XRF) works in a similar manner, the only difference being that an X-ray beam is used instead of an electron beam. Both of these techniques provide quantitative elemental analysis.

1.6.6. X-ray Diffraction

X-Ray Diffraction (XRD) can be used to characterize crystalline materials. It is mathematically expressed using Bragg's law:

$$n\lambda = 2d \sin\theta$$

In principle X-rays of a known wavelength (λ) are incident on the sample of interest. X-rays at an angle (θ) are reflected from the crystal planes of a sample. The sum of the angle of diffraction and the angle of the incidence is 2θ, as the angles are equal. The planes in the atomic lattice are separated by a distance (d), which reflects the angles at which the X-rays are diffracted. The constructive wave interference of the reflected waves produces the diffraction results, which provide information on the crystal structures within a sample.

1.6.7. Selected Area Electron Diffraction

Selected Area Electron Diffraction (SAED) utilizes a transmission electron microscope (TEM) to obtain information from a single crystal in a sample. TEM is a technique whereby scattered electrons produced, after transmission through the sample, lead to the production of an image. In SAED, the diffraction pattern from a single crystal within the sample is detected.

1.6.8. Raman Spectroscopy

Raman Spectroscopy is based on inelastic scattering. When monochromatic radiation interacts with a sample, it causes vibrational motions within the molecule. These vibrations, which are characteristic of the chemical structures within a sample, are then detected. A

spectrum of the scattering intensity with respect to the wavelength of the scattered photons is then reported.

1.7. Structure of This Thesis

The research presented in this dissertation is divided into three chapters. Each chapter will begin with a brief introduction discussing relevant theory, followed by an experimental section, in reference to the studies. The results of the research will then be presented along with conclusions drawn from the findings. Chapter 2 concerns with the use of X-ray Fluorescence for compositional analysis, alongside X-ray Absorption, to probe variations of an atoms physical/chemical state based on stoichiometry differences. Chapter 3 will include a close analysis comparing the electrochemical differences and overall crystallinity of two samples with varying compositions. Chapter 4 will demonstrate three specific deposition techniques and show the preliminary results of a full device. Final conclusions and recommendations for future studies will be presented in Chapter 5.

1.8. References

1.   Katagiri, H.; Jimbo, K.; Maw, W. S.; Oishi, K.; Yamazaki, M.; Araki, H.; Takeuchi, A., Development of CZTS-based thin film solar cells. *Thin Solid Films* **2009,** *517*, 2455.

2.   Siebentritt, S.; Schorr, S., Kesterites-a challenging material for solar cells. *Progress in Photovoltaics: Research and Applications* **2012,** *20*, 512.

3.   Mitzi, D. B.; Gunawan, O.; Todorov, T. K.; Wang, K.; Guha, S., The path towards a high-performance solution-processed kesterite solar cell. *Solar Energy Materials and Solar Cells* **2011,** *95*, 1421.

4.   Carraro, C.; Siniscalco, D., Strategies for the international protection of the environment. *Journal of Public Economics* **1993,** *52*, 309.

5.   Sands, P.; Peel, J.; Aguilar, A. F.; MacKenzie, R., *Principles of International Environmental Law*. Cambridge University Press: New York, 2012.

6.   Boer, Y. D. *Kyoto Protocol Reference Manual*. United Nations: Germany, 1998.

7.   Levin, K.; Bradley, R. *Comparability of Annex I Emission Reduction Pledges*; World Resources Institute: Washington, 2009.

8.   *The World Bank*. CO2 emissions (metric tons per capita). http://data.worldbank.org (accessed June 12, 2015).

9.   Gratzel, M., Photoelectrochemical cells. *Nature* **2001,** *414*, 338.

10.   Cameron, A., *Desert Energy: A Guide to the Technology, Impacts and Opportunities*. Taylor & Francis: New York, 2012.

11.   Chu, Y.; Meisen, P. *Review and comparison of different solar energy technologies*. Global Energy Network Institute (GENI): San Diego, 2011.

12.   Harati, M.; Jia, J.; Giffard, K.; Pellarin, K.; Hewson, C.; Love, D. A.; Lau, W. M.; Ding, Z., One-pot electrodeposition, characterization and photoactivity of stoichiometric copper indium gallium diselenide (CIGS) thin films for solar cells. *Physical Chemistry Chemical Physics* **2010,** *12*, 15282.

13.   Ananthoju, B.; Sonia, F. J.; Kushwaha, A.; Bahadur, D.; Medhekar, N. V.; Aslam, M., Improved structural and optical properties of Cu_2ZnSnS_4 thin films via optimized potential in single bath electrodeposition. *Electrochimica Acta* **2014,** *137*, 154.

14.   Valdes, M.; Modibedi, M.; Mathe, M.; Hillie, T.; Vazquez, M., Electrodeposited Cu_2ZnSnS_4 thin films. *Electrochimica Acta* **2014,** *128*, 393.

15. Wang, W.; Winkler, M. T.; Gunawan, O.; Gokmen, T.; Todorov, T. K.; Zhu, Y.; Mitzi, D. B., Device characteristics of CZTSSe thin-film solar cells with 12.6% efficiency. *Advanced Energy Materials* **2014,** *4*, 1301465.

16. Power generation in Canada. *Canadian Electricity Association*: Ottawa, 2006.

17. Chubb, D., *Fundamentals of Thermophotovoltaic Energy Conversion*. Elsevier: Amsterdam, 2007.

18. Wei-Hua, T.; Xiu-Li, F.; Zhi-Yong, Z.; Ling-Hong, L., Electronic and luminescent properties of Cr-doped cadmium sulfide nanowires. *Chinese Physics* **2006,** *15*, 773.

19. Guo, K. W., Green nanotechnology of trends in future energy: a review. *International Journal of Energy Research* **2012,** *36*, 1.

20. Flamant, G.; Kurtcuoglu, V.; Murray, J.; Steinfeld, A., Purification of metallurgical grade silicon by a solar process. *Solar Energy Materials and Solar Cells* **2006,** *90*, 2099.

21. Green, M. A.; Emery, K.; Hishikawa, Y.; Warta, W.; Dunlop, E. D., Solar cell efficiency tables (Version 45). *Progress in Photovoltaics: Research and Applications* **2015,** *23*, 1.

22. *U.S. Department of Energy.* $1/W Photovoltaic Systems: White Paper to Explore a Grand Challenge for Electricity from Solar. http://www1.eere.energy.gov/solar/sunshot/ (accessed September 3, 2014).

23. Vasekar, P. S.; Dhakal, T. P., Thin film solar cells using earth-abundant materials. In *Solar Cells - Research and Application Perspectives*, Morales-Acevedo, A., Ed. InTech: Rijeka, 2013.

24. Shockley, W.; Queisser, H. J., Detailed balance limit of efficiency of p-n junction solar cells. *Journal of Applied Physics* **1961,** *32*, 510.

25. Espinet-González, P.; Rey-Stolle, I.; Ochoa, M.; Algora, C.; García, I.; Barrigón, E., Analysis of perimeter recombination in the subcells of GaInP/GaAs/Ge triple-junction solar cells. *Progress in Photovoltaics: Research and Applications* **2014,** *23*, 874.

26. Ginley, D.; Green, M. A.; Collins, R., Solar energy conversion toward 1 terawatt. *MRS Bulletin* **2008,** *33*, 355.

27. Jones, R. K.; Ermer, J. H.; Fetzer, C. M.; King, R. R., Evolution of multijunction solar cell technology for concentrating photovoltaics. *Japanese Journal of Applied Physics* **2012,** *51*, 1.

28.   Kurtz, S. *Opportunities and challenges for development of a mature concentrating photovoltaic power industry*; National Renewable Energy Laboratory: Colorado, 2009.

29.   Yin, W.-J.; Wu, Y.; Wei, S.-H.; Noufi, R.; Al-Jassim, M. M.; Yan, Y., Engineering grain boundaries in $Cu_2ZnSnSe_4$ for better cell performance: a first-principle study. *Advanced Energy Materials* **2014,** *4*, 1300712.

30.   Chen, S.; Gong, X. G.; Walsh, A.; Wei, S.-H., Defect physics of the kesterite thin-film solar cell absorber Cu_2ZnSnS_4. *Applied Physics Letters* **2010,** *96*, 021902.

31.   Zoppi, G.; Forbes, I.; Miles, R. W.; Dale, P. J.; Scragg, J. J.; Peter, L. M., $Cu_2ZnSnSe_4$ thin film solar cells produced by selenisation of magnetron sputtered precursors. *Progress in Photovoltaics: Research and Applications* **2009,** *17*, 315.

32.   Akhavan, V. A.; Goodfellow, B. W.; Panthani, M. G.; Steinhagen, C.; Harvey, T. B.; Stolle, C. J.; Korgel, B. A., Colloidal CIGS and CZTS nanocrystals: A precursor route to printed photovoltaics. *Journal of Solid State Chemistry* **2012,** *189*, 2.

33.   Ahmed, S.; Reuter, K. B.; Gunawan, O.; Guo, L.; Romankiw, L. T.; Deligianni, H., A high efficiency electrodeposited Cu_2ZnSnS_4 solar cell. *Advanced Energy Materials* **2012,** *2*, 253.

34.   Shin, B.; Gunawan, O.; Zhu, Y.; Bojarczuk, N. A.; Chey, S. J.; Guha, S., Thin film solar cell with 8.4% power conversion efficiency using an earth-abundant Cu_2ZnSnS_4 absorber. *Progress in Photovoltaics: Research and Applications* **2013,** *21*, 72.

35.   Collier, J.; Wu, S.; Apul, D., Life cycle environmental impacts from CZTS (copper zinc tin sulfide) and Zn_3P_2 (zinc phosphide) thin film PV (photovoltaic) cells. *Energy* **2014,** *74*, 314.

36.   Kim, J.; Park, C.; Pawar, S. M.; Inamdar, A. I.; Jo, Y.; Han, J.; Hong, J.; Park, Y. S.; Kim, D. Y.; Jung, W.; Kim, H.; Im, H., Optimization of sputtered ZnS buffer for Cu_2ZnSnS_4 thin film solar cells. *Thin Solid Films* **2014,** *566*, 88.

37.   Jheng, B.-T.; Liu, P.-T.; Wang, M.-C.; Wu, M.-C., Effects of ZnO-nanostructure antireflection coatings on sulfurization-free Cu_2ZnSnS_4 absorber deposited by single-step co-sputtering process. *Applied Physics Letters* **2013,** *103*, 052904.

38.   Scragg, J. J., *Copper Zinc Tin Sulfide Thin Films for Photovoltaics: Synthesis and Characterisation by Electrochemical Methods*. Springer: Berlin, 2011.

39.   Ito, K.; Nakazawa, T., Electrical and optical properties of stannite-type

quaternary semiconductor thin films. *Japanese Journal of Applied Physics* **1988,** *27*, 2094.

40.   Katagiri, H.; Saitoh, K.; Washio, T.; Shinohara, H.; Kurumadani, T.; Miyajima, S., Development of thin film solar cell based on Cu_2ZnSnS_4 thin films. *Solar Energy Materials and Solar Cells* **2001,** *65*, 141.

41.   Katagiri, H.; Jimbo, K.; Moriya, K.; Tsuchida, K. Solar cell without environmental pollution by using CZTS thin film, *Photovoltaic Energy Conversion* **2003,** *3*, 2874.

42.   Katagiri, H.; Jimbo, K.; Yamada, S.; Kamimura, T.; Maw, W. S.; Fukano, T.; Ito, T.; Motohiro, T., Enhanced conversion efficiencies of Cu_2ZnSnS_4-based thin film solar cells by using preferential etching technique. *Applied Physics Express* **2008,** *1*, 041201.

43.   Todorov, T. K.; Reuter, K. B.; Mitzi, D. B., High-efficiency solar cell with earth-abundant liquid-processed absorber. *Advanced Materials* **2010,** *22*, E156.

44.   Todorov, T. K.; Tang, J.; Bag, S.; Gunawan, O.; Gokmen, T.; Zhu, Y.; Mitzi, D. B., Beyond 11% efficiency: characteristics of state-of-the-art $Cu_2ZnSn(S,Se)_4$ solar cells. *Advanced Energy Materials* **2013,** *3*, 34.

45.   Abermann, S., Non-vacuum processed next generation thin film photovoltaics: Towards marketable efficiency and production of CZTS based solar cells. *Solar Energy* **2013,** *94*, 37.

46.   Kamoun, N.; Bouzouita, H.; Rezig, B., Fabrication and characterization of Cu_2ZnSnS_4 thin films deposited by spray pyrolysis technique. *Thin Solid Films* **2007,** *515*, 5949.

47.   Zhang, X.; Shi, X.; Ye, W.; Ma, C.; Wang, C., Electrochemical deposition of quaternary Cu_2ZnSnS_4 thin films as potential solar cell material. *Applied Physics A* **2008,** *94*, 381.

48.   Moriya, K.; Watabe, J.; Tanaka, K.; Uchiki, H., Characterization of Cu_2ZnSnS_4 thin films prepared by photo-chemical deposition. *Physica Status Solidi (C)* **2006,** *3*, 2848.

49.   Zhang, K. Z.; Tao, J. H.; He, J.; Wang, W. J.; Sun, L.; Yang, P. X.; Chu, J. H., Composition control in Cu_2ZnSnS_4 thin films by a sol-gel technique without sulfurization. *Journal of Materials Science* **2014,** *25*, 2703.

50.   Tanaka, K.; Moritake, N.; Uchiki, H., Preparation of thin films by sulfurizing sol–gel deposited precursors. *Solar Energy Materials and Solar Cells* **2007,** *91*, 1199.

51.   Scragg, J. J.; Dale, P. J.; Peter, L. M.; Zoppi, G.; Forbes, I., New routes to sustainable photovoltaics: evaluation of Cu_2ZnSnS_4 as an alternative absorber material. *Physica Status Solidi (B)* **2008,** *245*, 1772.

52.   Bard, A. J., *Electrochemical Methods: Fundamentals and Applications.* Wiley: New York, 1990.

53.   Rauschenbach, H. S., *Solar Cell Array Design Handbook: The Principles and Technology of Photovoltaic Energy Conversion.* Springer: New York, 2012.

54.   Razeghi, M., *The MOCVD Challenge: A Survey of GaInAsP-GaAs for Photonic and Electronic Device Applications.* Taylor & Francis: Florida, 2011.

Chapter 2. Compositional Analysis Using X-Ray Fluorescence and X-ray Absorption Spectroscopy

One of the most important techniques for characterization of thin film solar cells is via the use of X-ray Fluorescence (XRF). Section 2.1 will discuss the theory behind XRF and its importance for compositional analysis. It will also examine the principles and properties of synchrotron radiation for X-ray Absorption Spectroscopy studies. Section 2.2 will include the experimental procedures used for the related research in this chapter. Section 2.3 involves the XRF calibration procedures examined and the final compositional data for the samples of interest. This section will also include the corresponding results obtained for the varying Cu_2ZnSnS_4 (CZTS) nanocrystals (NCs) using X-ray Absorption Spectroscopy.

2.1. CZTS composition

The photoresponse of CZTS NCs has been found to depend on the compositional ratio of the elements of the preferred crystal structure. The Cu content in CZTS samples is primarily important because a series of secondary phases and defects can result from excess Cu contents. For example the dominant Cu_{Zn} antisite (acceptor defect) has the lowest energy of formation and samples with Cu-rich contents are more likely to yield this kind of defect.[1] Furthermore, ternary phases such as Cu-Sn-S (i.e Cu_2SnS_3) are responsible for the low open-circuit voltage (V_{OC}) seen in Cu-rich devices.[2] In turn, the Cu content can vastly affect the electronic properties of this p-type semiconductor. XRF and XAFS were techniques used to determine the final compositions of samples with varying Cu-concentrations and their structural properties, respectively.

2.2. General Theory Behind the Production of X-rays

2.1.1. Background: X-ray Absorption and Fluorescence

In 1985, Wilhelm Conrad Röntgen became the first person to systematically study electromagnetic radiation in a wavelength range now commonly known as X-rays.[3] Two of the common ways in which X-rays can be produced are via Bremsstrahlung radiation and synchrotron radiation. The former occurs when energetic electrons are decelerated upon contact with a metal target in X-ray tubes. The latter can precede when electrons are

accelerated in circular orbits. Synchrotrons generate beams of X-rays that are higher in brightness and polarization than ones produced from conventional X-ray tubes. This is because they allow the spatial resolution to be reduced down to the micrometer level.[4] Third generation synchrotrons contain an insertion device (wigglers or undulators) that accelerate charged particles and give rise to a much higher X-ray intensity than ones seen from conventional X-ray systems. As a result, this technique has been extensively used for X-ray Absorption Spectroscopy (XAS) measurements.[5]

Experimentally, data is obtained for a given element when the energy of the incoming X-ray is larger than the binding energy of the electron in the core level of the atom. This causes the ejection of the electron from its quantum level. The probability of absorption is defined using the Beer-Lambert law:[6]

$$I = I_0 e^{-\mu t}$$

where I is the intensity of the transmitted X-ray, I_0 is the incident beam intensity, the absorption is expressed as 'μ', which is known as the absorption coefficient (cm^{-1}) and t is the thickness of the sample (cm). The energy of the X-ray will determine how strongly it will be absorbed; thereby affecting the value of the absorption coefficient. Generally, a common feature in experimental measurements involves a decrease in μ with an increase in energy. The details pertaining to an X-ray absorption spectra are defined under X-ray absorption fine structure (XAFS).

2.1.2. X-ray Absorption Fine Structure

XAFS is commonly used as an element-specific method to probe the physical and chemical states of atoms. When the X-ray photon energy corresponds to the binding energy of the core electron on the K or L shell, a sharp increase in the absorption coefficient is observed.[5] As shown in Figure 2.1, this is defined as the absorption edge. The variation in the binding energies and absorption edges of every element provides specific characterization at an atomic level. The region referred to as X-ray absorption near-edge structure (XANES) in Figure 2.1, includes the pre-edge and ~ 50 eV above the absorption edge region.[5] The peaks in XANES are influenced by the oxidation state and coordination geometry (e.g., tetrahedral, octahedral coordination) of the absorbing atom.
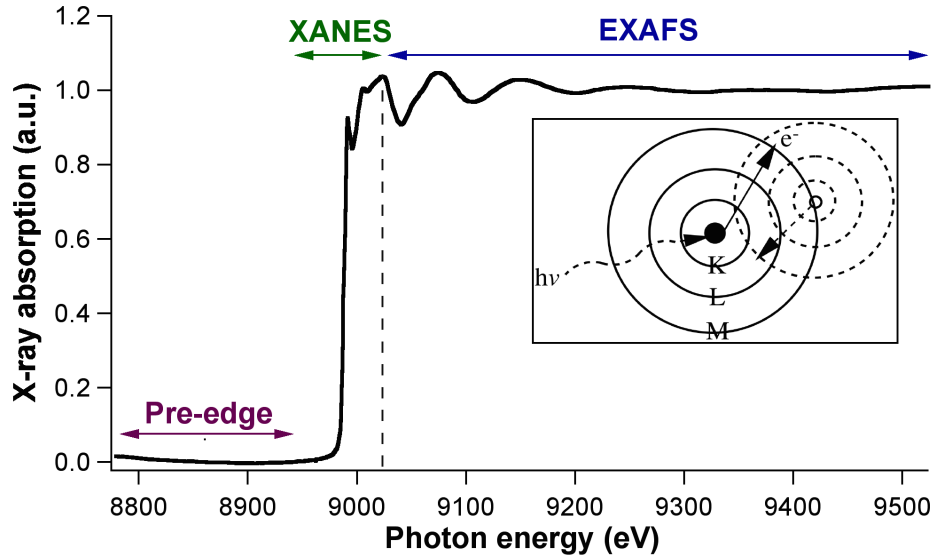
Figure 2.1. A typical X-ray Absorption Schematic shown using Cu. The inset pertains to the cause of the oscillations in the EXAFS region.

If the absorbing atom is not isolated, a wave behavior is seen following the XANES region. This is known as the extended X-ray absorption fine structure (EXAFS) region and is described in the inset seen in Figure 2.1. The initial absorption causes the ejection of an electron, known as the photoelectron. The outgoing wave of the photoelectron becomes backscattered by surrounding atoms and gives rise to an incoming wave. The interference of these waves results in sinusoidal modulations indicated in the absorption rate. The difference in frequency of the wave signal relates to the inter-atomic distance between the absorbing atom and the neighboring atom.[6] The amplitude of the modulation corresponds to the bonding and the types of atoms surrounding the absorption atom; in turn, EXAFS information cannot be extracted if a free atom is used, as no surrounding atoms are present.

The EXAFS region can be interpreted in accordance with the following equation:[7]

$$\chi(k) = \sum_j \frac{N_j f_j(k) e^{-2k^2\sigma_j^2}}{kR_j^{\,2}} \sin[2kR_j + \delta_j(k)]$$

where χ is the expression used to describe EXAFS, j is the number of shells of all of the atoms, N is the number of neighboring atoms, R is the distance between neighboring atoms, σ^2 is the Debye-Waller factor (disorder in the neighbor distance due to thermal effects), $f(k)$ is

the backscattering amplitude and δ(*k*) is the phase-shift of the central atom. Once the f(*k*) and δ(*k*) scattering parameters are determined, the *R*, σ² and *N* can be quantified. Using the intensity of the scattering and oscillations EXAFS provides information on the neighboring atoms.

2.1.3. X-ray Fluorescence

Upon the photoelectron ejection that occurs when an X-ray strikes an atom, a core-hole is left behind. This creates instability within the atom and as a result, an electron from an outer shell falls to a lower energy level to fill that vacancy.[8] Figure 2.2 displays the different electron transitions (inset) and their corresponding peaks. The most frequent electron transitions occur from the L-shell to the K-shell (K∝). This transition can be seen in the inset of Figure 2.2. This transfer leads to the most intense peak seen in an XRF spectrum (Figure 2.2). The next commonly classified transition occurs from the M-shell to the K-shell (Kβ). Lastly, electrons can also move down to the L-shell from either the M-shell (L∝) or the N-shell (Lβ).[8]
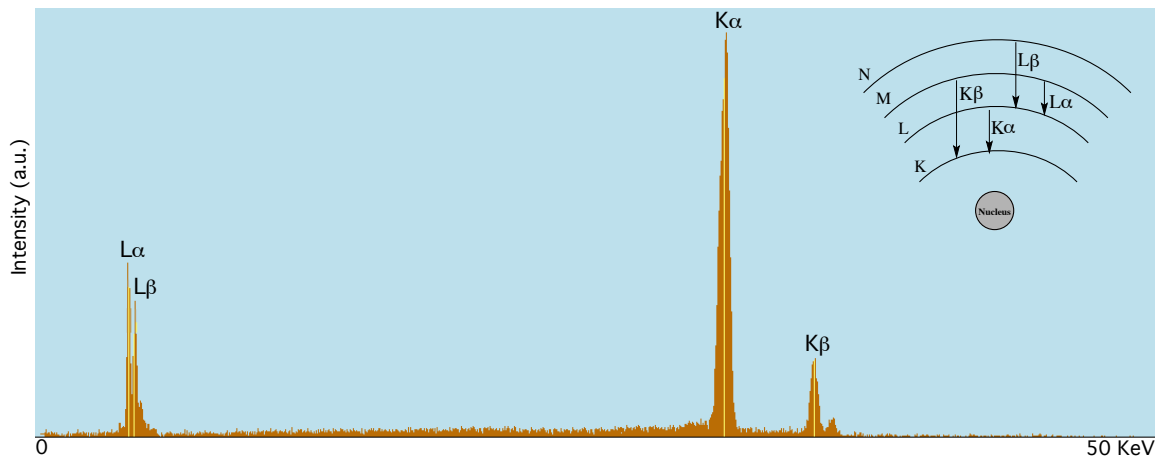
Figure 2.2. Energy dispersive XRF spectrum of Sn, including all transitions. The characteristic x-ray lines (K, L, M, N) and specific energy transitions in an atom are displayed in the inset.

The energy transition from the outer to the inner shell is characteristic of a certain element. The difference between the two binding energies is given off as an X-ray, which is then detected. This process is known as X-ray Fluorescence. The instrument collects the emitted X-rays that are characteristic of the elements in the sample and produces a spectrum (intensity vs. photon energy). The X-ray intensity is dependent on the concentration of the

element; the higher the concentration, the higher the count number. This technique is commonly used as a non-destructive method to determine the elemental composition/concentration of various samples, in either powder, solid or liquid form.[1]

2.3. Experimental

2.2.1. Chemicals

Copper (II) acetylacetonate (≥99.99%), zinc (II) acetylacetonate hydrate, gallium (III) nitrate hydrate (99.9%) and thiourea (≥99.0%) were purchased from Sigma-Aldrich. Tin (II) chloride (99%), benzyl alcohol (99+%) and 2-mercapto-5-n-propylpyrimdine (MPP) were the products of Alfa Aesar. All products were of analytical grade and used without further purification. Water was obtained from a Millipore Milli-Q system (resistivity of 18.3 M Ω cm).

2.2.2. Preparation of the CZTS Nanocrystals

CZTS NCs were synthesized using a one-pot solvothermal method. The precursor mixture was prepared by the addition of 3mL of benzyl alcohol to the metal salts. The mixture was then heated in a silicon oil bath (usable range from -40°C to + 200°C, Alfa Aesar) at 160 °C for 2 min, to dissolve the salts. Thiourea (dissolved at 0.2 M in benzyl alcohol) was then added, followed by addition of the capping ligand, MPP. The mixture was then heated at 180 °C for 10 min, then left to cool until room temperature. The CZTS nanoparticles were then centrifuged at 12.0×10^3 times gravity. The supernatant was decanted and the NCs were washed using acetone twice. The nanoparticles were then dispersed in acetone via sonication for 10 min. The mixture was centrifuged again and the resulting precipitates were left to air dry.

2.2.3. Characterization

Composition analysis was carried out using XRF (Horiba XGT-5000) at an operating voltage of 50 kV. For XRF measurements, the NCs were digested in 10 mL of concentrated HNO_3 (about 15.6 M) and the solutions were placed in XRF sample cups (Delta Scientific) and covered using a Mylar film (Delta Scientific). A standard solution containing 1000 μg/mL Cu, Zn, Sn and S (MES-062014-UWO1, Delta Scientific) was used for XRF calibration.

The K-edge EXAFS measurements were completed at the PNC/XSD 20-BM beamline of the Advanced Photon Source (APS) at Argonne National Laboratory (Illinois, USA). This instrument contained a 13-element Canberra detector (Intel 120 CPS) and a Si(1 1 1) monochromator. The NCs were placed on Kapton tape with a thickness of about 1-2 absorption lengths. The samples were then placed at 45° while the fluorescence detector was placed at 90°, with respect to the incident photons. In order to prevent detector saturation, the count rate of the detector was kept below 50,000. Reference foils (50 μm, EXAFS Materials Inc.) were used for energy calibration. The reference foils were placed downstream of the samples and measured in transmission mode.

Note: These measurements were carried out by Matthew J. Turnbull.

For the data analysis Athena software was first used to plot the spectra. The pre-edge and post-edge backgrounds were subtracted and the absorptions were normalized to the incident intensity for all of the spectra. The normalized spectra were then converted to k-space. Using a k^2 weighting and a k-range of 2.5 to 10 $Å^{-1}$, fourier transform was performed to obtain the R-space spectra.

2.4. Results and Discussion

2.3.1. XRF Calibration

XRF calibration involved the use of a commercial reference that contained known concentrations of the elements of interest. This was done to ensure the reported compositions were representative of the specific CZTS samples. All XRF measurements were performed on a conventional Energy Dispersive XRF (ED-XRF) instrument.

Prior to the aforementioned calibration procedure, two other methods were assessed. The first involved the use of prepared calibration samples in solution form and the second included the use of an internal standard prior to sample drying. Figure 2.3 shows the first set of calibration standards that were prepared and measured in solution form.
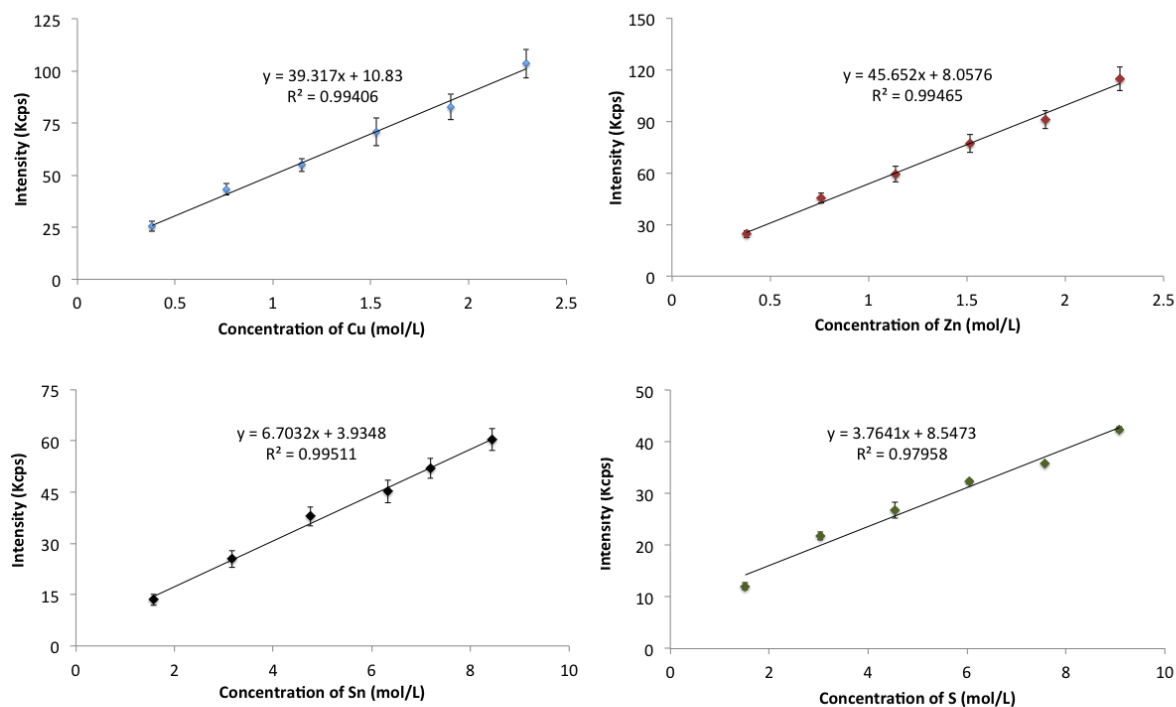
Figure 2.3. Calibration plots for Cu, Zn, Sn and S.

The concentrations for Sn and S ranged from 1.5-9.0 mol L^{-1}. The range for Cu and Zn was lower, as it was from 0.4-2.3 mol L^{-1}. A set of 6 standards were prepared for each element and each data point was measured a minimum of 4 times. As shown in Figure 2.3, the intensity of the elements were linearly proportional to their concentrations. Despite the high correlation of the metals, when determining the composition of the synthesized CZTS samples, the final compositions were not reflective of their respective intensities. This is because the intensity responses were well below the linear range of the calibration graphs. For the second calibration method these concentrations were drastically reduced.

The second calibration procedure, involved the use of dried samples and the addition of Gallium as an internal standard. As shown in Figure 2.4 the calibration curve is a plot of the intensity ratio of the element over the intensity of the internal standard vs. the mass of the desired element over the mass of the internal standard. The measurements indicate high correlation as $R^2 > 0.99$. It is important for the sample of interest to maintain the same physical and chemical properties as the standards; in turn, the CZTS NCs were digested in nitric acid, dropcast and left to dry. The line was extrapolated to 0 in order to determine the concentration of the unknown CZTS samples (not shown). Again, the final composition of the ratios was not reflective of their respective intensities (see Appendix). One of the main

reasons for this discrepancy is due to the fact that the solidified films were not completely homogeneous. Deviations were also noted when different regions on the same sample were measured. This suggests that the non-uniformity in the thickness and morphology of the films could be the reason for the variations.
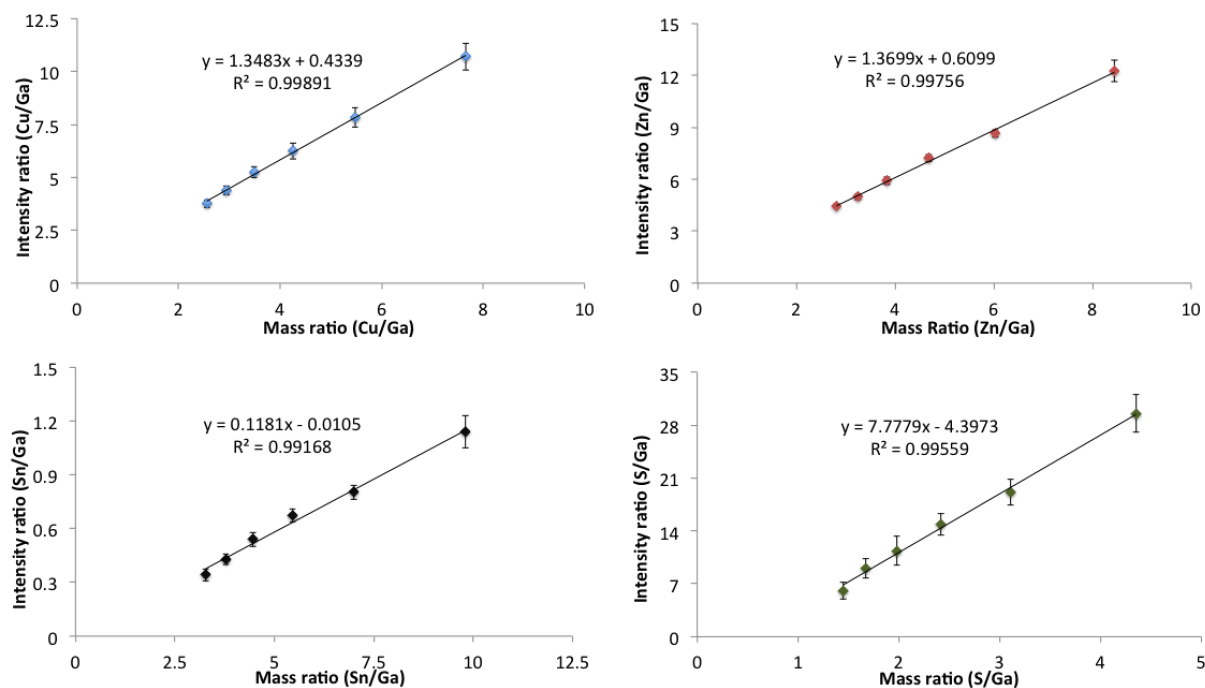
Figure 2.4. Calibration graphs plotted using Gallium as an internal standard for Cu, Zn, Sn and S.

The final calibration procedure involved the use of samples in solution. This was done to eliminate the deviation in results caused by heterogeneity. A multi-element reference standard containing known concentrations of Cu, Zn, Sn and S was purchased from Delta Scientific. Upon measuring the standard, the composition of five CZTS samples was determined using their respective intensities. It is important to note that once the CZTS NCs were digested in concentrated HNO_3 an apparent gas was observed. Cu, Sn and Zn metals are oxidized in the presence of concentrated nitric acid; this reaction produces nitrogen dioxide gas.[9-10] Thiourea and MPP are both incompatible with strong oxidizing agents; their reaction causes the formation of sulfur dioxide and other gases.[11-12] The result of this caused lower sulfur contents to be detected, than what is represented in the sample. To circumvent inaccuracy and reduce error, additional standards were prepared containing thiourea and MPP; both of which are used in the CZTS synthesis. The differences in results were then

compared and discrepancies between the compounds and the reference standard were then accounted for.

Upon calibration, the compositions of five samples were quantified. The results are summarized in Table 2.1. The stoichiometry of CZTS was changed, via an increase in the initial Cu content, from samples 1 to 5, respectively. This variation resulted in a final Cu/Zn stoichiometric ratio of 1.7, 1.9, 2.0, 2.2 and 2.4 for CZTS NCs 1 to 5, respectively.

Table 2.1. Starting and final compositions of CZTS NCs with increasing Cu-content. The final ratios were determined using XRF.

CZTS	Starting ratio Cu:Zn:Sn:S	Final ratio	$\dfrac{Cu}{(Zn+Sn)}$	$\dfrac{Zn}{Sn}$
1	0.82:1.42:1.00:3.79	$Cu_{1.7\pm0.1}Zn_{1.0\pm0.1}Sn_{1.0\pm0.1}S_{4.9\pm0.5}$	0.85	1.00
2	0.90:1.42:1.00:3.79	$Cu_{1.9\pm0.1}Zn_{1.0\pm0.1}Sn_{1.1\pm0.1}S_{4.7\pm0.3}$	0.90	0.91
3	0.96:1.42:1.00:3.79	$Cu_{2.0\pm0.1}Zn_{1.0\pm0.1}Sn_{1.1\pm0.1}S_{4.5\pm0.7}$	0.95	0.91
4	1.03:1.42:1.00:3.79	$Cu_{2.2\pm0.1}Zn_{1.0\pm0.1}Sn_{1.1\pm0.1}S_{4.3\pm0.4}$	1.04	0.91
5	1.11:1.42:1.00:3.79	$Cu_{2.4\pm0.2}Zn_{1.0\pm0.1}Sn_{1.0\pm0.1}S_{4.8\pm0.7}$	1.20	1.00

The Zn, Sn and S ratios remained relatively consistent in all samples, as equal quantities of these elements were used in the synthesis. The measured Cu/Zn+Sn and Zn/Sn compositional ratios were between 0.85-1.2 and 0.9-1.0, respectively. A ratio of 1, for both, would represent a stoichiometric sample. In the data shown, sample 3 would be considered stoichiometric and 4 would be considered near stoichiometric, as the minimal deviation is within the error of margin. NCs 1 and 2 would be considered Cu-poor, as the Cu/Zn ratio falls below 2 and the Cu/Zn value of 2.4 for CZTS 5, suggests a Cu-rich composition.

The variation in the Cu precursor, ultimately affected the final Cu composition in the samples. Stoichiometry plays an important role in the quality of a CZTS thin film; in turn differences in compositions need to be accurately detected. As indicated, this can only achieved once the instrument is calibrated correctly.

2.3.2. X-ray Absorption Spectroscopy: XANES

The XANES region provides information about the electronic structure and geometry of the target element. Changes in the XANES region can provide information on deviations that exist within the local structure of a specific atom. Figure 2.5 displays the XANES of Cu,

Zn and Sn.

These spectra display a sharp rise in the absorption edge, which is due to the 1s→4p dipole transition.[13] Following the edge is the post-edge region, consisting of broader features originating from transitions of 1s electrons to unbound molecular orbitals. At the Cu K-edge, the intense peak is seen at ~8979 eV (Figure 2.5 (a)), for all of the corresponding samples. The spectra appear similar with overlapping features, suggesting that the Cu environments are unaffected by the compositional changes.

Small variations appear in the Zn XANES (Figure 2.5 (b)). The position of the K-edge absorption energy is seen at ~ 9659 eV for Zn. Slight differences are noted in the amplitude of the initial peak and post-edge features, as they appear higher for CZTS 3 ($Cu_{2.0}Zn_{1.0}Sn_{1.1}S_{4.5}$) and 5 ($Cu_{2.4}Zn_{1.0}Sn_{1.0}S_{4.8}$); however, the number of features are the same indicating similar number of scattering pathways as a result of analogous coordination numbers. Also, the positions of the features are in parallel, implying similar interatomic distances between the absorbing atom and surrounding neighbors. The minor differences in amplitudes could be due to the background function as a result of multiple scattering. It appears as a smooth curve across the spectrum and this can vary between samples. For analysis this is subtracted from the data and normalized, which can cause slight variations between spectrums.

a) **Cu**

Cu K Absorbance

$Cu_{1.7}Zn_{1.0}Sn_{1.0}S_{4.9}$
$Cu_{1.9}Zn_{1.0}Sn_{1.1}S_{4.7}$
$Cu_{2.0}Zn_{1.0}Sn_{1.1}S_{4.5}$
$Cu_{2.2}Zn_{1.0}Sn_{1.1}S_{4.3}$
$Cu_{2.4}Zn_{1.0}Sn_{1.0}S_{4.8}$

b) **Zn**

c) **Sn**
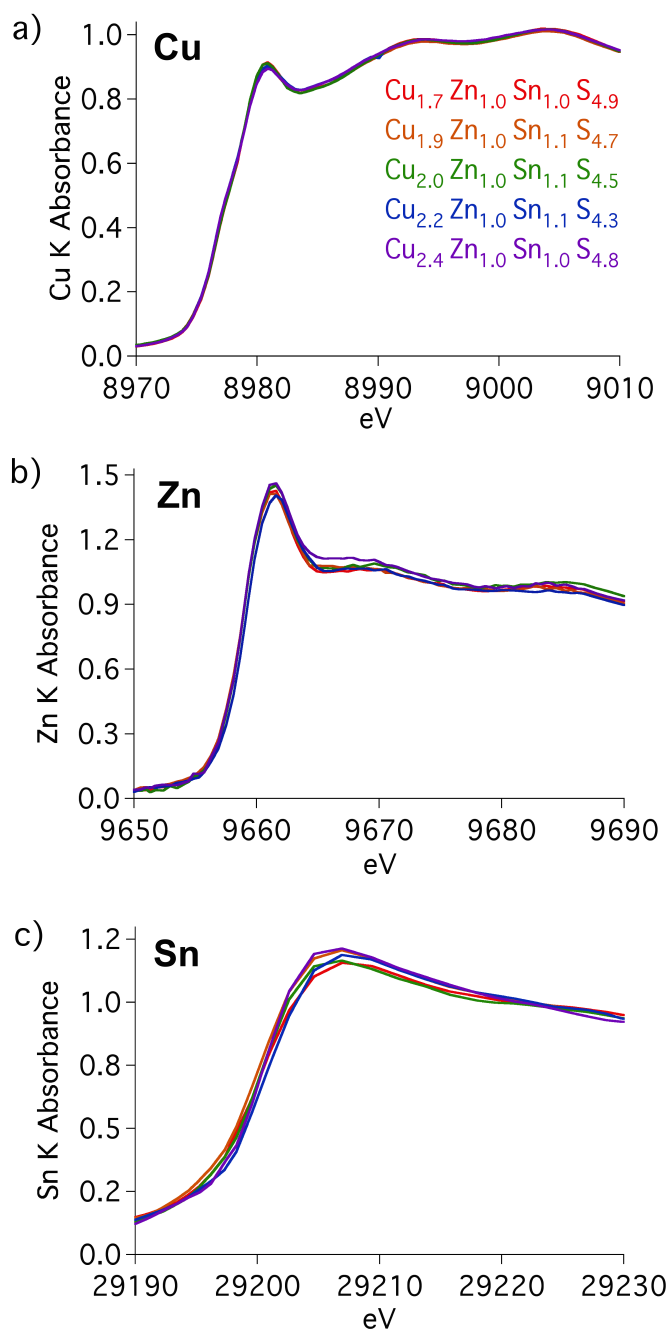
Figure 2.5. XANES spectra of the K-edge for (a) Cu, (b) Zn and (c) Sn.

Figure 2.5 (c) displays the Sn XANES with a K-edge of 29200 eV. The higher absorption edge for Sn vs. Cu and Zn, causes less features and more broadening due to the increase in the core-hole lifetime width. In theory an element with a greater atomic number will have a shorter lifetime, causing enhanced broadening. Small shifts in the absorption edge are noted and more apparent between CZTS 4 and CZTS 2 (~1eV difference). The edge for the higher Cu content sample is at a greater energy than the latter. The shifts could also be

due to the broadening, as the overall spectral weights appear analogous. A bigger difference in amplitude is seen between the samples than previously shown for Zn. This pertains to the bond distance between the absorbing atom and the nearest neighbor. According to the spectra, the bond distance between Sn-S is shorter for CZTS 1, 3 and 4 vs. CZTS 2 and 5. An important feature that is noted is the difference in the shape of the nodes past the absorption edge for the Cu rich sample (CZTS 5). This could be due to a change in either the arrangement or number of neighboring shells. As these spectra are not well resolved, further analysis via EXAFS is required.

2.3.3. X-ray Absorption Spectroscopy: EXAFS

In order to extract the EXAFS (χ) data, from the absorption (μ), the energy is converted to k-space (wave vector k). $\chi(k)$ is then multiplied by k^n (n=1,2 or 3) to emphasize the oscillations.[7] Figure 2.6 shows the k^2 weighted $\chi(k)$ function of Cu, Zn and Sn.
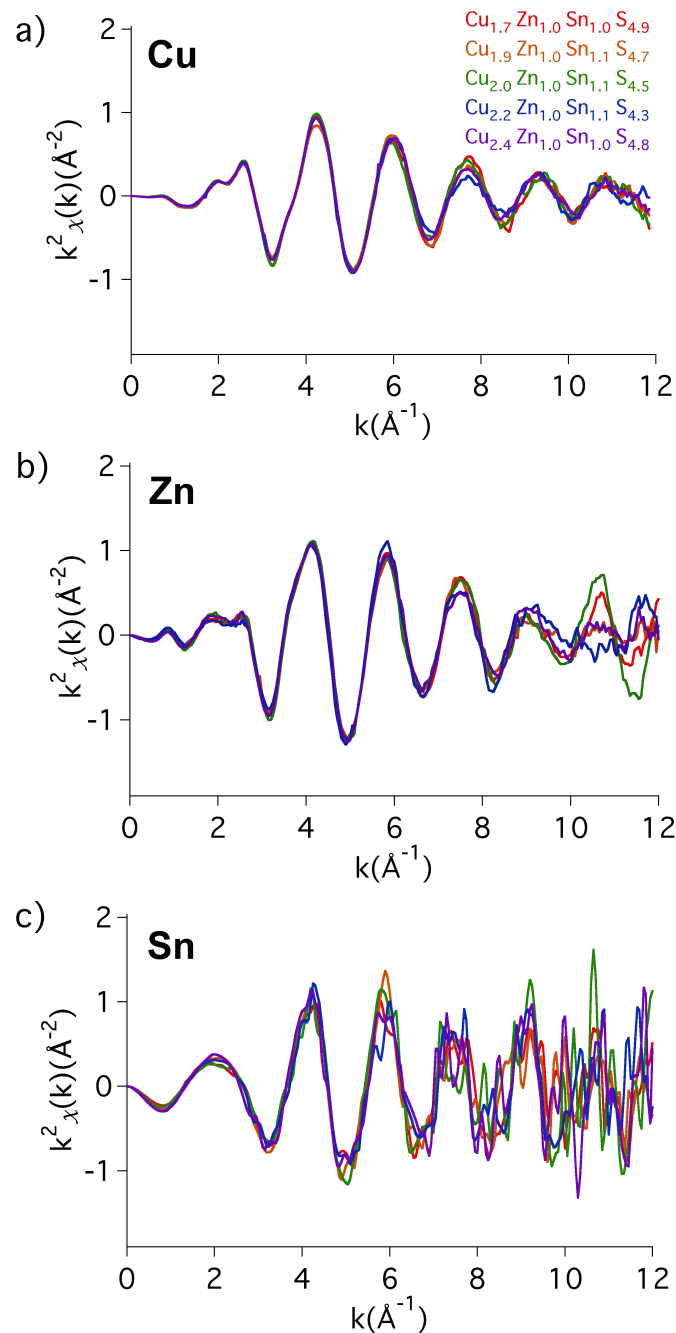
Figure 2.6. The k^2 weighted EXAFS data at the K-edge of (a) Cu, (b) Zn and (c) Sn for the five CZTS samples.

The sinusoidal function represents the contributions of the coordination shells and the frequency is relative to the distance between the absorbing and scattering atoms. Figure 2.7 displays the crystal structure of CZTS, the nearest neighbor and the third shell for all of the metals is S. The second shell surrounding the Cu and Zn environments are Cu, Sn and Zn/Cu atoms. For Sn, the second nearest neighbor is Cu and Zn.
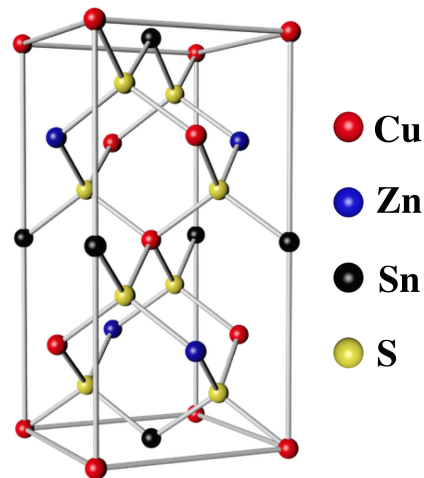
Figure 2.7. Kesterite structure of Cu₂ZnSnS₄.

In reference to Cu (Figure 2.6 (a)), the spectra consist of a single sinusoidal wave for each sample, which decrease in amplitude with an increase in k. The initial oscillations correspond to the nearest neighbor of Cu, which is S. The waves at higher k values relate to the second and third neighbors, which is why a decrease in amplitude is seen.

A somewhat similar trend is seen with Zn (Figure 2.6 (b)). The difference noted here is the increase in amplitude for CZTS 3 past 10 Å. This suggests that past the nearest neighbor, for this sample, a different second shell is detected, in comparison to the other samples. In reference to the theoretical backscattering amplitudes of various elements, the scattering amplitude of Sn is higher than Cu and Zn, past 10Å.[14] Overall, Sn is a heavier element, causing a more profound impact on the oscillation signal, implying that for this sample, Sn is the detected second shell neighbor. It is also important to note that a Sn_{Zn} antisite (occupation of Sn on a Zn site) could occur. As shown using XRF, the composition of this sample is Cu-stoichiometric, Sn-rich and Zn-poor (Zn/Sn = 0.91), meaning that higher concentrations of Sn could have induced this defect. One of the primary reasons Cu-poor, Sn-poor and Zn-rich compositions are ideally used is to decrease/prevent this kind of substitution, among others.[15-17] CZTS 1 shows a similar trend but with a lower intensity past 10 Å. The difference in intensities could be due to different metal-metal interactions. The composition of this sample is Cu-poor with stoichiometric levels of Zn and Sn (Zn/Sn=1). It is important to note that under these conditions a V_{Cu} (vacancy at the Cu position) and/or a Cu_{Zn} (occupation of Cu at the Zn site) antisite could form; however the detection of these

defects would be difficult, solely using EXAFS.[16, 18-19] As for the Sn spectra (Figure 2.6 (c)), a clear overlap in the oscillations is seen for the different samples; however, due to the high level of noise, interpretation past 10 Å is difficult.

To isolate the different shells, Fourier transform from $\chi(k)$ into R-space $\chi(R)$ was completed. Figure 2.8 displays the modulus of the Fourier transform for Cu, Zn and Sn.
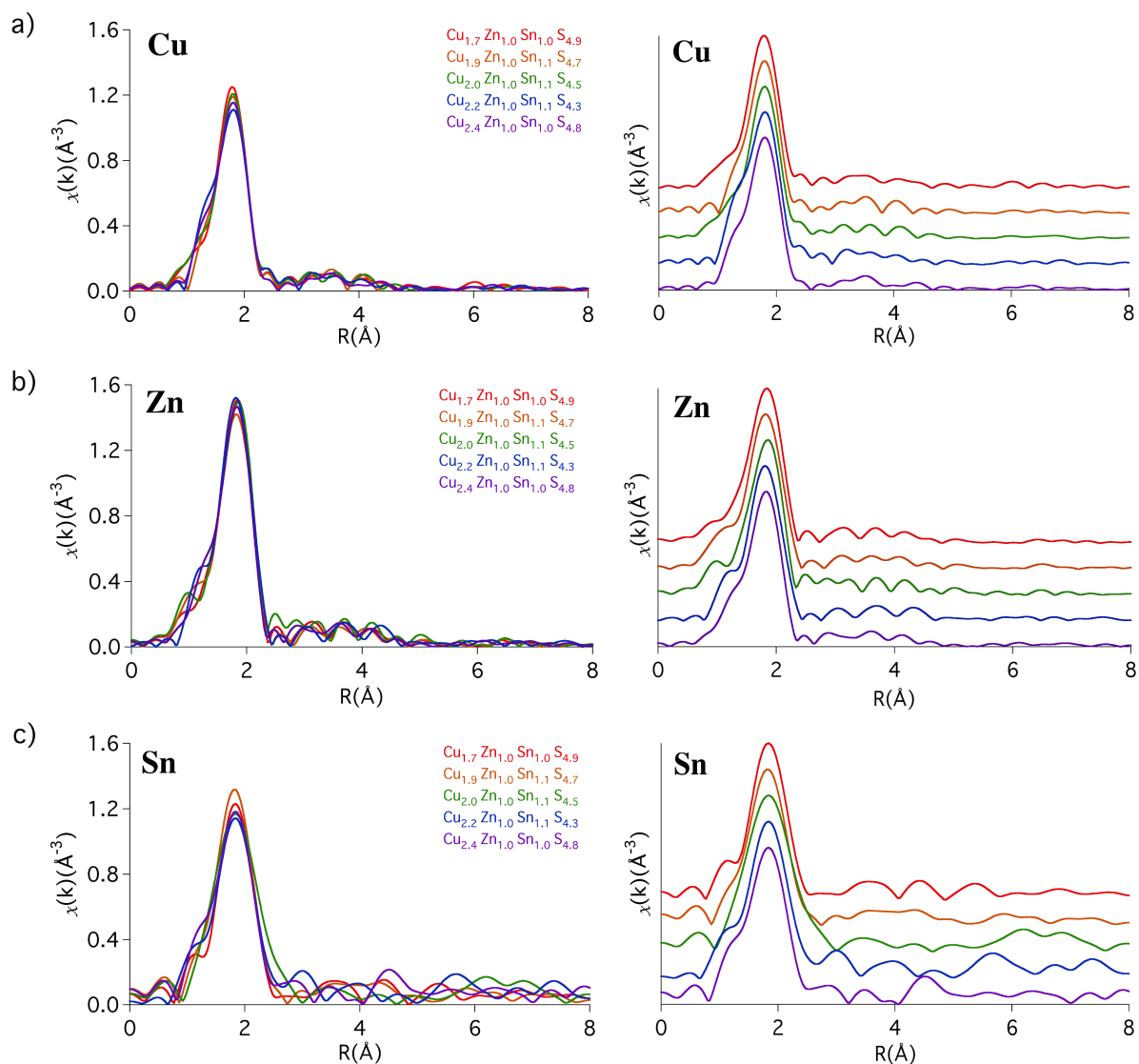
Figure 2.8. Phase shift-uncorrected Fourier Transformed EXAFS spectra for (a) Cu, (b) Zn and (c) Sn, overlapped (left) to indicate the difference in intensities and separated (right) to distinguish the effects of the higher shell neighbors.

The peaks shown represent the uncorrected phase of the radial distribution. When the photoelectron wave travels from the absorbing atom to and back from the backscattering

atom, several phase shifts occur. This causes phase shifts in R that are an underestimation of the true value by 0.2-0.5 Å.[20] The nearest neighbor for all of the metals is S, the peak for this first coordination shell can be seen at approximately 1.81 Å for Cu (Figure 2.8 (a)) and Zn (Figure 2.8 (b)) and at 1.84 Å for Sn (Figure 2.8 (c)). Following this well-defined peak, are smaller peaks indicative of higher coordination shells. Theoretically, the first neighbor shell for Cu and Zn is seen at ~2.33 Å (Figure 2.8 (a) and (b)) and ~2.41 Å for Sn (Figure 2.8 (c)). In accordance with the phase shift, the experimental values fall within the expected radial distribution.

The difference in intensities in the first shell, with varying Cu contents, can be seen for all 3 metals in Figure 2.8 (a). For Cu the height of this peak is highest for the Cu-deficient sample and lowest for the near stoichiometric/somewhat Cu-rich sample (CZTS 4). The peak for the second shell of the Cu-deficient sample ($Cu_{1.7}Zn_{1.0}Sn_{1.0}S_{4.9}$) sample is seen at approximately 3.34 Å. Theoretically this is seen at 3.839 Å for Cu-Cu/Zn and 3.845 Å for Cu-Sn.[21] Considering the phase shift this is in alignment with the Cu-Cu/Zn shell distance. For the remaining CZTS NCs (CZTS 2- CZTS 5), a double peak is seen at the second shell, which is indicative of two scattering pathways at approximately 3.2 Å and 3.5 Å.

The magnitude of the first neighbor peak corresponds to the long-range order of the nanocrystals, indicating higher order for the Cu-deficient sample ($Cu_{1.7}Zn_{1.0}Sn_{1.0}S_{4.9}$). The data suggests that the stoichiometries with lower Cu-contents achieve a more conserved crystal structure. Also, the peak intensity corresponds to the coordination number, which can be affected by thermal motion (Debye-Waller factor).[15] A change in the coordination number would result in apparent shifts/intensity differences in the XANES region[15, 22], which is not visible in Figure 2.5. The Debye-Waller factor corresponds to thermal energy that is absorbed by the molecule, triggering a vibrational motion. The greater the vibrations within a molecule, the higher the signal distortion and as a result, the lower the peak intensity.[23] Thus, disorder within a sample, causes an increase in the Debye-Waller factor, which causes a decrease in peak intensity.[24] As the temperature remained consistent for all samples at around 300K, the higher peak intensity for the Cu-deficient sample corresponds to better long-range order.

A similar trend is seen for the radial distributions of Sn, as the peak intensities for the Cu-poor samples is higher than the Cu-stoichiometric and Cu-rich NCs. Conclusive interpretation for the second shell is difficult, as the peaks following the initial are broad with

little consistency. The high noise level in the k-range and the absence of more detailed features in Figure 2.8 (c), could be the cause of this uncertainty. The overall differences past the first shell could also suggest some local disorder within the lattice. A different trend is seen for the Zn radial distributions as shown in (Figure 2.8 (b)). In this case the peak intensity is equally high for both the Cu-deficient sample and somewhat Cu-rich CZTS. The differences in intensities seem negligible for Zn, suggesting similar order within the lattice. The intensity for the second nearest neighbor is highest for the Cu-deficient and Cu-stoichiometric sample and lower for the higher Cu NCs. There is also a clear shift in this peak for the Cu-rich CZTS, indicative of a shorter radial distance.

2.5. Conclusions

XRF has demonstrated to be an important non-destructive technique for quantitative analysis. This application is essential for photovoltaic fabrication, as stoichiometry plays a crucial role in film quality and ultimately device efficiency. While this method is non-destructive, it can produce inaccurate and non-reproducible results if not calibrated accordingly. Calibration using a reference standard provided the most accurate results.

Upon calibration, the compositional ratio of the CZTS samples was determined and all proceeding measurements were quantified against the standard. The XRF results confirmed that the only variation between the samples were the varying Cu-contents, as the starting ratios for the other elements remained constant. The results indicated a final Cu/Zn stoichiometric ratio of 1.7, 1.9, 2.0, 2.2 and 2.4 for CZTS NCs 1 to 5, respectively.

Upon determining the concentrations of the elements in each sample, XAFS was used to determine variability in the local environment and distribution of the elements with the increasing Cu-content. This technique was used as an element-specific method to probe the physical and chemical states of Cu, Zn and Sn. The K-edge specified in XANES represented the excitation of the 1s electron. The spectra pertaining to the samples for Cu and Zn appeared similar with comparable features, suggesting that the environments of these two metals were somewhat unaffected by the compositional changes. The minor differences in amplitudes seen for the Zn absorption could have been due to the background function as a result of multiple scattering. A bigger difference in amplitude was seen for Sn, primarily due to the enhanced broadening. An important feature that was noted was the difference in the shape of the nodes past the absorption edge for the Cu rich sample. This suggested either a

change in the arrangement or number of neighboring shells. The data was analyzed further using EXAFS.

The peaks were represented as the phase-uncorrected radial distribution. Experimental phase shifts caused an underestimation of the true bond distance value between 0.2-0.5 Å. The most intense peak represented the nearest neighbor for all of the metals (S) which was seen at ~1.81 Å for Cu and Zn and at 1.84 Å for Sn. In accordance with the phase shift, the experimental values were within the expected radial distribution. The magnitude of the first neighbor peak for Cu and Sn, were higher for the Cu-deficient samples vs. the Cu-rich. This suggested that the stoichiometries with lower Cu-contents achieved a more conserved crystal structure. The differences in intensities were negligible for Zn, indicating similar order within the lattice. Overall the data suggested better crystallinity was achieved for the Cu-deficient samples; however, the presence/absence of local lattice distortions is difficult to conclude without further evidence using simulations.

2.6. References

1.   Chen, S.; Gong, X. G.; Walsh, A.; Wei, S.-H., Defect physics of the kesterite thin-film solar cell absorber Cu_2ZnSnS_4. *Applied Physics Letters* **2010,** *96*, 021902.

2.   Berg, D. M.; Dale, P. J., Kesterites. In *Copper Zinc Tin Sulfide-Based Thin-Film Solar Cells*, Wiley: Chichester, 2015, 107.

3.   Shackley, M. S., An Introduction to X-Ray Fluorescence (XRF) Analysis in Archaeology. In *X-Ray Fluorescence Spectrometry (XRF) in Geoarchaeology*, Shackley, M. S., Ed. Springer: New York, 2011, 7.

4.   Xu, M. Crystallization of Zirconium Palladium Copper and Zirconium Nickel Copper Metallic Glass. *PhD. dissertation*. Iowa State University: Iowa, 2008.

5.   Penner-Hahn, J. E., X-ray Absorption Spectroscopy. In *Comprehensive Coordination Chemistry II*, Meyer, J. A., McCleverty, T. J., Ed. Pergamon: Oxford, 2003, 159.

6.   Rehr, J. J.; Albers, R., Theoretical approaches to X-ray absorption fine structure. *Reviews of Modern Physics* **2000,** *72*, 621.

7.   Newville, M., Fundamentals of XAFS. *Reviews in Mineralogy and Geochemistry* **2014,** *78*, 33.

8.   Jenkins, R., X-Ray Fluorescence Analysis. In *X-ray Characterization of Materials*, Lifshin, E., Ed. Wiley: Weinheim, 1999, 171.

9.   Saxena, P. B., *IIT Chemistry-I*. Krishna Prakashan: India, 2001.

10.   Saxena, P. B., *Advanced Inorganic Chemistry*. Krishna Prakashan: India, 2000.

11.   *Thiourea (Thiocarbamide)*. CAS No. 62-56-6; Chem One Ltd.: Texas, 1998.

12.   *2-Mercapto-5-n-propylpyrimidine*. CAS No. 52767-84-7; Alfa Aesar: Massachusetts, 2008.

13.   Sarangi, R., X-ray absorption near-edge spectroscopy in bioinorganic chemistry: Application to M-O systems. *Coordination Chemistry Reviews* **2013,** *257*, 459.

14.   Teo, B. K., *EXAFS: Basic Principles and Data Analysis*. Springer: Oxford, 1986.

15.   Mino, L.; Agostini, G.; Borfecchia, E.; Gianolio, D.; Piovano, A.; Gallo, E.; Lamberti, C., Low-dimensional systems investigated by x-ray absorption spectroscopy: a selection of 2D, 1D and 0D cases. *Journal of Physics D: Applied Physics* **2013,** *46*, 423001.

16.   Ito, K., *Copper Zinc Tin Sulfide-Based Thin Film Solar Cells*. Wiley: Chichester,

2015.

17.   Chen, S.; Wang, L.-W.; Walsh, A.; Gong, X. G.; Wei, S.-H., Abundance of CuZn + SnZn and 2CuZn + SnZn defect clusters in kesterite solar cells. *Applied Physics Letters* **2012,** *101*, 223901.

18.   Zillner, E.; Paul, A.; Jutimoosik, J.; Chandarak, S.; Monnor, T.; Rujirawat, S.; Yimnirun, R.; Lin, X. Z.; Ennaoui, A.; Dittrich, T.; Lux-Steiner, M., Lattice positions of Sn in Cu_2ZnSnS_4 nanoparticles and thin films studied by synchrotron X-ray absorption near edge structure analysis. *Applied Physics Letters* **2013,** *102*, 221908.

19.   Bacewicz, R.; Antonowicz, J.; Podsiadło, S.; Schorr, S., Local structure in Cu_2ZnSnS_4 studied by the XAFS method. *Solid State Communications* **2014,** *177*, 54.

20.   Crichton, R. R.; Louro, R. O., *Practical Approaches to Biological Inorganic Chemistry*. Elsevier: Oxford, 2012.

21.   Espinosa-Faller, F. J.; Conradson, D. R.; Riha, S. C.; Martucci, M. B.; Fredrick, S. J.; Vogel, S.; Prieto, A. L.; Conradson, S. D., Neutron diffraction and X-ray absorption fine structure evidence for local lattice distortions and aperiodic antisite substitution in Cu_2ZnSnS_4 nanoparticles. *The Journal of Physical Chemistry C* **2014,** *118*, 26292.

22.   Mottana, A.; Marcelli, A., The Historical Development of X-ray Absorption Fine Spectroscopy and of Its Applications to Materials Science. In *A Bridge between Conceptual Frameworks*, Pisano, R., Ed. Springer: Dordrecht, 2015, 275.

23.   Fultz, B.; Howe, J. M., *Transmission Electron Microscopy and Diffractometry of Materials*. Springer: Berlin, 2012.

24.   Vila, F. D.; Rehr, J.; Rossner, H.; Krappe, H., Theoretical x-ray absorption Debye-Waller factors. *Physical Review B* **2007,** *76*, 014301.

Chapter 3. Effects of Cu on the Photoelectrochemistry of CZTS Thin Films

As the X-ray absorption spectroscopy (XAS) studies in Chapter 2 focused on elemental variations with the changing Cu-content, this chapter includes further studies on two of the compositions: Cu-poor and Cu-stoichiometric nanocrystals (NCs). A change in the Zn content was also made, as it was increased to yield films with a Zn-rich final composition. The correlation between composition and structure of the nanocrystals were then investigated. Section 3.1 gives relevant background information on the importance of non-stoichiometric growth conditions for Cu_2ZnSnS_4 thin films. Section 3.2 presents the experimental procedures and techniques. The results and discussion of the experimental data using electrochemical methods and characterization techniques are reported in Section 3.3.

3.1. Introduction

3.1.1. Crystal Structures of CZTS

CZTS possesses two main structures: stannite and kesterite.[1] The former is in the $I\bar{4}2m$ space group, while the latter corresponds to the $I\bar{4}$ space group. The difference between the two tetragonal structures is attributed to the varying arrangements of Zn^{2+} and half of the Cu^+ atoms (Figure 3.1). As shown in Figure 3.1 the CuSn metals alternate at the z=0 and z=1/2 planes, while the CuZn atoms alternate at z=1/4 and z=3/4, for the kesterite crystal structure. In reference to the stannite phase, ZnSn alternate at z=0 and z=1/2 while only Cu exists at the z=1/4 and z=3/4 planes. Both structures contain 4 Cu^+, 2 Zn^{2+}, 2 Sn^{4+} and 8 S^{2-} atoms and similarly each S group is bounded to 2 Cu^+, 1 Zn^{2+} and 1 Sn^{4+} atom. Lastly as shown in Figure 3.1, Sn resides on the same site in both phases.
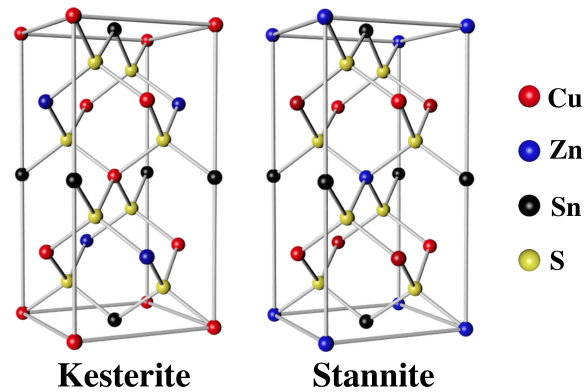
Figure 3.1. The two crystal structures of CZTS.

The kesterite structure is desirable due to the fact that it is thermodynamically more stable, making it an ideal candidate for high performance thin film solar cells.[2] Literature has suggested that under Cu-poor and Zn-rich conditions the ideal kesterite phase is predominantly formed.[3] The dominant Cu_{Zn} antisite, which has the lowest energy of formation, is suppressed under these conditions. Furthermore, the formation of V_{Cu} and Zn_{Cu} (Zn at the Cu site) is enhanced.[4] The defect complex $[V_{Cu}^- + Zn_{Cu}^+]^o$ is presumed to enhance charge separation, similar to $[2V_{Cu}^- + In_{Cu}^{2+}]^o$ in $CuInSe_2$ materials.[4-5] The electronic passivation of In_{Cu}^{2+} by $2V_{Cu}^-$ plays a major role in the high device efficiencies of $CuInSe_2$.[6-7] As a result, these non-equilibrium growth conditions are optimal and beneficial for CZTS devices.

3.1.2. Secondary Phases

A series of potential secondary phases can form during the CZTS synthesis. These can affect the overall properties of the film and subsequently the device performance. Some examples of dominant phase impurities include Cu_2S, Cu_2SnS_3 and ZnS. Cu_2S and Cu_2SnS_3 are conductive secondary phases with small band gaps.[8-9] Their formation would be detrimental as it could enhance recombination and/or cause frequent shunting within a device.[8-10] These are expected to form under Cu-rich and Zn-poor stoichiometries.

The presence of ZnS could contribute to a devices' low photocurrent due to its large band gap (3.5-3.8 eV).[11] Primarily, under Cu-poor, Zn-rich compositions this secondary phase can form; however, unlike the Cu containing secondary phases, ZnS is not detrimental as it does not behave like a recombination center; however it may reduce the photoresponse of the film, if located at the surface.[10, 12]

Cu and Zn play major roles in the optimal film production of CZTS. Literature has shown that the highest efficiency devices for CZTS have been composed of Cu-poor, Zn-rich ratios: Cu/(Zn + Sn) ≈ 0.85, Zn/Sn ≈ 1.1-1.3 and Cu/Sn ≈1.8-2.0.[13-16] Cu-poor and Zn-rich conditions are not only desirable for predominant phase formation but also to prevent the formation of detrimental secondary phases.

3.2. Experimental

Chemicals as described in Section 2.2.1, with the addition of methyl viologen dichloride hydrate (98%) which was purchased from Sigma-Aldrich. Preparation of CZTS NCs were as described in Section 2.2.2. The difference being that the starting ratios of copper: zinc: tin: sulfur for Cu-stoichiometric and Cu poor were 1.00: 1.49: 1.00: 3.95 and 0.89: 1.47: 1.00: 3.79 respectively.

3.2.1. CZTS Thin Films

FTO glass (Sigma-Adrich, 2 mm thickness, surface resistivity ~ 13 Ω/sq) was used as the back contact for the films. They were cleaned via sonication for 10 min in 2% Hellmanex (Hellma Analytics) cleaning solution. They were then rinsed (3-4 times) with milli-Q water and afterwards sonicated in milli-Q water for 10 min. Thereafter, the glass was rinsed using ethanol and sonicated in ethanol for 10 min. Lastly, they were again rinsed with ethanol and dried using argon gas. Once the NCs were dry they were dispersed in isopropanol (20 g/L). The mixture was then sonicated and deposited onto clean FTO coated glass. Prior to dropcast, half of the glass was covered with polyimide tape (Creative Global Services Inc.), leaving only an area of 10 mm^2 exposed for the CZTS film.

3.2.2. Characterization

The quality of the films was assessed using Chronoamperometric-PEC (Chrono-PEC) measurements/PEC measurements with an electrochemical analyzer (CHI 832a, CH Instruments, Austin, TX). The set-up included a 3-electrode system, with the CZTS on FTO as the working, a Pt coil as the counter and a saturated calomel electrode as the reference. The electrodes were immersed in 0.05 M MVCl$_2$ and 0.1M KCl. A 150 W Xenon lamp with D filter, rendering AM1.5 spectrum (Newport, Irvine, CA) was used as the light source. A shutter controller (ThorLabs SC10, Newton, NJ) was used to obtain a 3 s light on/off

alternative exposure onto the sample. Linear potential sweep voltammetry was applied between 0 and -0.4 V, at a scan rate of 5 mV/s. Chrono-PEC measurements were performed using the same instrument and set-up but at a constant potential. iR compensation was measured in the dark, at an applied potential of -0.3V vs. SCE, using the same instrumentation.

The IMPS was measured using an Ivium CompactStat (±30mA @ ±7.5V) and ModuLight Module (20.0 mW/cm^2). White light emitting diodes (wavelength ranging from 460-660 nm), with a modulation amplitude of 2.4 mW/cm^2 and a frequency range of 0.01 Hz to 1000 Hz was used. Measurements were carried out at two potentials: -0.2 V and -0.3 V. The device efficiency was determined using the same instrument.

The crystal structure of the NCs was examined using XRD (Inel CPS Powder Diffractometer with Symphonix software for the JSPDS database) and Raman spectroscopy (AlphaSNOM, Witec, ULM, Germany) with a Nikon 50X objective with numerical aperture of 0.75 (WD 0.48) utilizing a 1800 g/cm^3 grating and a 532 nm laser operating at 10 mW. High-resolution TEM (HRTEM) images and SAED patterns of the samples were obtained using a FEI Tecnai G2 F20 microscope. The samples were dispersed in ethyl alcohol and sonicated for approximately 6 hours, then dropcasted onto carbon coated copper grids and dried under infrared light. The band gaps of the samples were determined using a Varian Cary 5000 spectrophotometer.

Morphology and thickness of the films were obtained using SEM (Hitachi S-4500 field emission SEM with a Quartz XOne EDX system). Composition analysis was carried out using EDX at an operating voltage of 15 kV and XRF (Section 2.2.3).

3.3. Results and Discussion

3.3.1. Compositional Analysis using XRF and EDX

Table 3.1 displays the quantitative results obtained using XRF and EDX for the final composition of both samples. The experiments were repeated three times to acquire more accurate results. EDX showed that the Cu-poor and Cu-stoichiometric ratios for Cu: Zn: Sn: S were 1.8: 1.2: 1.0: 4.9 and 2.0: 1.2: 1.1: 5.0, respectively. Correspondingly, XRF indicated similar results (Cu-poor, 1.8: 1.1: 1.0: 4.8 and Cu stoichiometric, 2.1: 1.2: 1.0: 5.1). The results obtained using the two methods indicated high correlation and negligible variation. It is important to note that for the XRF measurements, the CZTS NCs were digested in HNO_3

prior to analysis. XRF was employed to ensure that variation that might exist due to thickness and/or surface topography following the EDX area scans did not exceedingly alter the final compositions. On the other hand, EDX characterization of the thin films did not require treatment, post-dropcast. Overall, these complementary techniques were used to decrease compositional error.

The excess sulfur is due to the presence of the capping ligand, MPP, still bound to the NCs. As previous studies have indicated, this organic ligand could facilitate in the electron transfer of the material, upon illumination.[17-20] As a result, post-processes, such as annealing were not performed to eliminate the MPP.

Table 3.1. EDX and XRF data for Cu-poor and Cu-stoichiometric CZTS NCs.

	Cu-poor	**Cu-stoichiometric**
EDX	$Cu_{1.8\pm0.1}Zn_{1.2\pm0.1}Sn_{1.0\pm0.1}S_{4.9\pm0.5}$	$Cu_{2.0\pm0.1}Zn_{1.2\pm0.1}Sn_{1.1\pm0.1}S_{5.0\pm0.2}$
XRF	$Cu_{1.8\pm0.1}Zn_{1.1\pm0.1}Sn_{1.0\pm0.1}S_{4.8\pm0.4}$	$Cu_{2.1\pm0.1}Zn_{1.2\pm0.1}Sn_{1.0\pm0.1}S_{5.1\pm0.3}$

As previously mentioned literature has shown that the highest efficiency devices for CZTS have been composed of Cu-poor, Zn-rich ratios: Cu/(Zn + Sn) ≈ 0.85, Zn/Sn ≈ 1.1-1.3 and Cu/Sn ≈1.8-2.0.[13-16] In this work, various starting ratios of Cu/Sn were tested (0.4–2.2), until the composition of the final NCs fell close to the range of the aforementioned ratios.

3.3.2. Electron and X-ray Diffraction

Figure 3.2 (a) illustrates the XRD results obtained for both Cu-stoichiometric and Cu-poor samples, which were dropcast onto microscope slides. The standard diffraction peaks for kesterite CZTS (JCPDS No. 26-0575), stannite CZTS (JCPDS No. 04-016-8345), and possible secondary phases that could form during the synthesis are displayed below the experimental spectra. The XRD 2θ peaks for the Cu-poor sample were at 28.6°, 47.6° and 56.0° and at 28.5°, 46.9° and 55.4° for the Cu-stiochiometric. These peaks correspond to the (112), (220) and (312) planes of kesterite CZTS, respectively. As shown in Figure 3.2 (a), the slight downward peak shift corresponding to the (112) plane and dramatic decrease in

intensity at the (220) Bragg peak seen for the simulated stannite CZTS structure were not observed in the experimental data. While the XRD peaks for the Cu-stoichiometric is broader than that of the Cu-poor, the XRD peak pattern for both samples are very similar. Sharper and more resolved peaks indicate that the lower Cu content has lead to better crystallinity within the film. From the (112) peak, the lattice space was determined to be 0.310 and 0.312 nm for the Cu-poor and Cu- stoichiometric samples, respectively. The tetragonal unit cell parameters, calculated from the (112) and (220) peak positions, found that a=b=5.39 and 5.37 Å, and c=10.67 and 10.63 Å for the Cu-poor and Cu-stoichiometric NCs, respectively. These values are within close proximity of the kesterite margins.[12, 21] The size of the NCs calculated using the Debye-Scherrer equation[22] were 3.35 nm and 2.47 nm for Cu-poor and Cu-stoichiometric, respectively, indicating that the Cu-deficient films contained larger NCs than the Cu-stoichiometric samples.
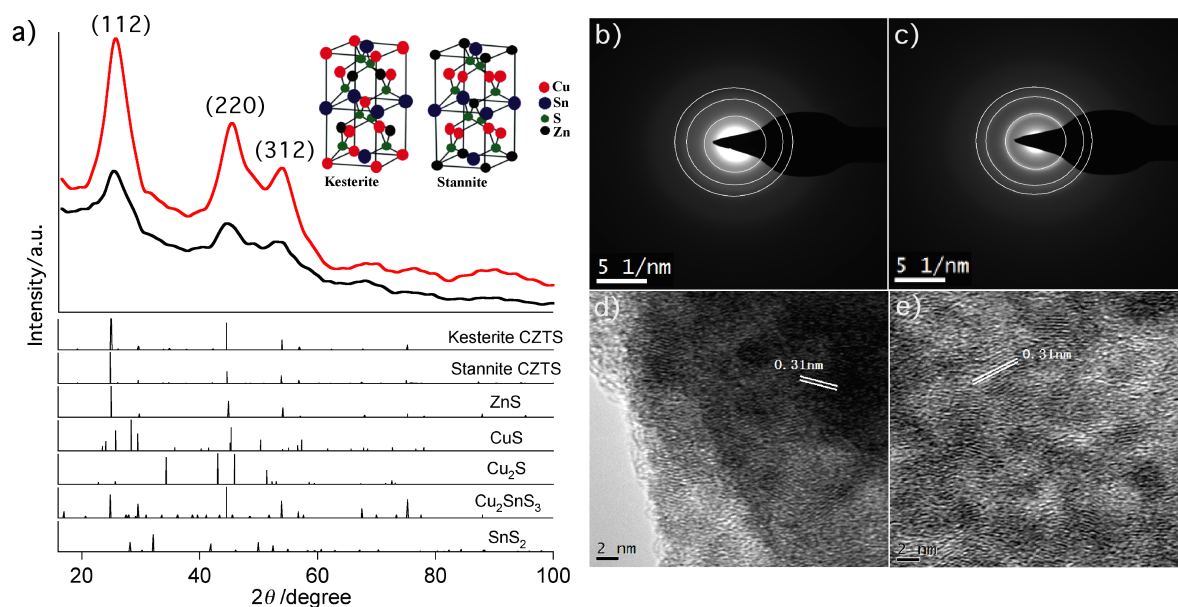
Figure 3.2. (a) The XRD pattern for the Cu-stoichiometric (black) and Cu-poor (red) thin films. The JCPDS data for CZTS and the potential secondary phases that can form during the synthesis are shown below the spectra. The kesterite and stannite CZTS crystal structures are shown in the inset. SAED patterns of Cu-poor (b) and Cu-stoichiometric (c). HRTEM images of Cu-poor (d) and Cu-stoichiometric (e) samples.

As shown in Figure 3.2 (a), the XRD peaks for secondary phases, such as SnS_2 (JCPDS No. 23-0677)[23] and Cu_2S (JCPDS No. 26-1116)[24] exhibit distinguishable patterns from those of CZTS. There are no obvious peaks corresponding to these phases visible in

both Cu-poor and Cu-stoichiometric CZTS XRD spectra; therefore, within the detection limit of XRD we can conclude that these secondary phases are absent from the films.

The SAED patterns are illustrated in Figure 3.2 (b-c) for Cu-poor and Cu-stoichiometric CZTS samples, respectively. The rings 1, 2, 3 occurring in the reciprocal space correspond to the (112), (220), and (312) planes, respectively. The ring patterns reveal the existence of the polycrystalline and NC aggregation nature of the CZTS samples.[25-26] Moreover, Figure 3.2 (d) and (e) show the HRTEM images of the Cu-poor and Cu-stoichiometric, respectively. The lattice fringes of both crystals are visible, further indicating crystallinity. The brightest crystal plane in the SAED rings of CZTS is associated with the (112) plane. The measured interplanar spacings was 0.31 nm for both NCs, as shown in the HRTEM images (Figure 3.2 (d) and (e)). This is consistent with other literature.[27-28] Within these measurements a significant difference between the Cu-poor and Cu-stoichiometric samples is not seen.

3.3.3. Raman Spectroscopy

Figure 3.3 compares the Raman spectra of both samples to confirm the above XRD and TEM observations and further examine if the secondary phase ZnS exists within the NCs. The characteristic peak for CZTS is known to be at 336-339 cm^{-1} (A_1).[26, 29-32] In addition, CZTS has a weak mode at approximately 289 cm^{-1} and shoulder 368-374 cm^{-1}.[29-32] As shown in Figure 3.3 the A_1 mode at 339 cm^{-1} is visible in both spectrums. This peak is well defined for the Cu-poor sample while that for the Cu-stoichiometric is less pronounced. There is a hump between 291-305 cm^{-1} and a shoulder at approximately 371 cm^{-1}. The presence of some peak broadening primarily in the Cu-stoichiometric film corresponds to some structural disorder within the sample. On the other hand, the XRD peak pattern for ZnS overlaps with that of kesterite CZTS (Figure 3.2 (a)), implying that the presence of this secondary phase cannot be distinguished via XRD. In contrast, Raman peak at 275 cm^{-1} and 352 cm^{-1} [29] are not seen, indicating the absence of ZnS. Other secondary phases in which are not visible within the spectrum include $Cu_{2-x}S$ (peaks at 264 cm^{-1} and 475 cm^{-1}), orto-CTS (318 cm^{-1}), cubic-CTS (267 cm^{-1}, 303 cm^{-1} and 356 cm^{-1}) and hexagonal SnS_2 (314 cm^{-1}).[29]
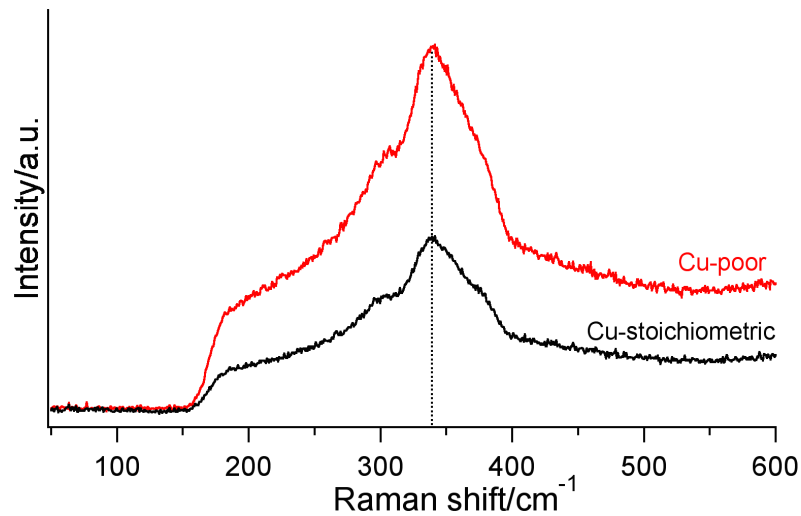
Figure 3.3. Raman spectra of the Cu-poor (red) and Cu-stoichiometric (black) CZTS films.

3.3.4. Surface Morphology

Figure 3.4 shows typical SEM images of both films. Two different solvents were used to dropcast the CZTS NCs: isopropanol (Figure 3.4 (a) and (b)) and acetone (Figure 3.4 (c) and (d)). Evidently, the thin films prepared using acetone appeared to have a more rough and uneven surface. As a result, isopropanol was the solvent of choice for all experiments.

Since the same volume (5 μL) of solvent was dropcast each time, the thickness of the films was approximately 1 μm. An example of the Cu-poor film is shown in Figure 3.4 (e). This is in alignment with the desired CZTS thickness of 1-2μm.[33-34]
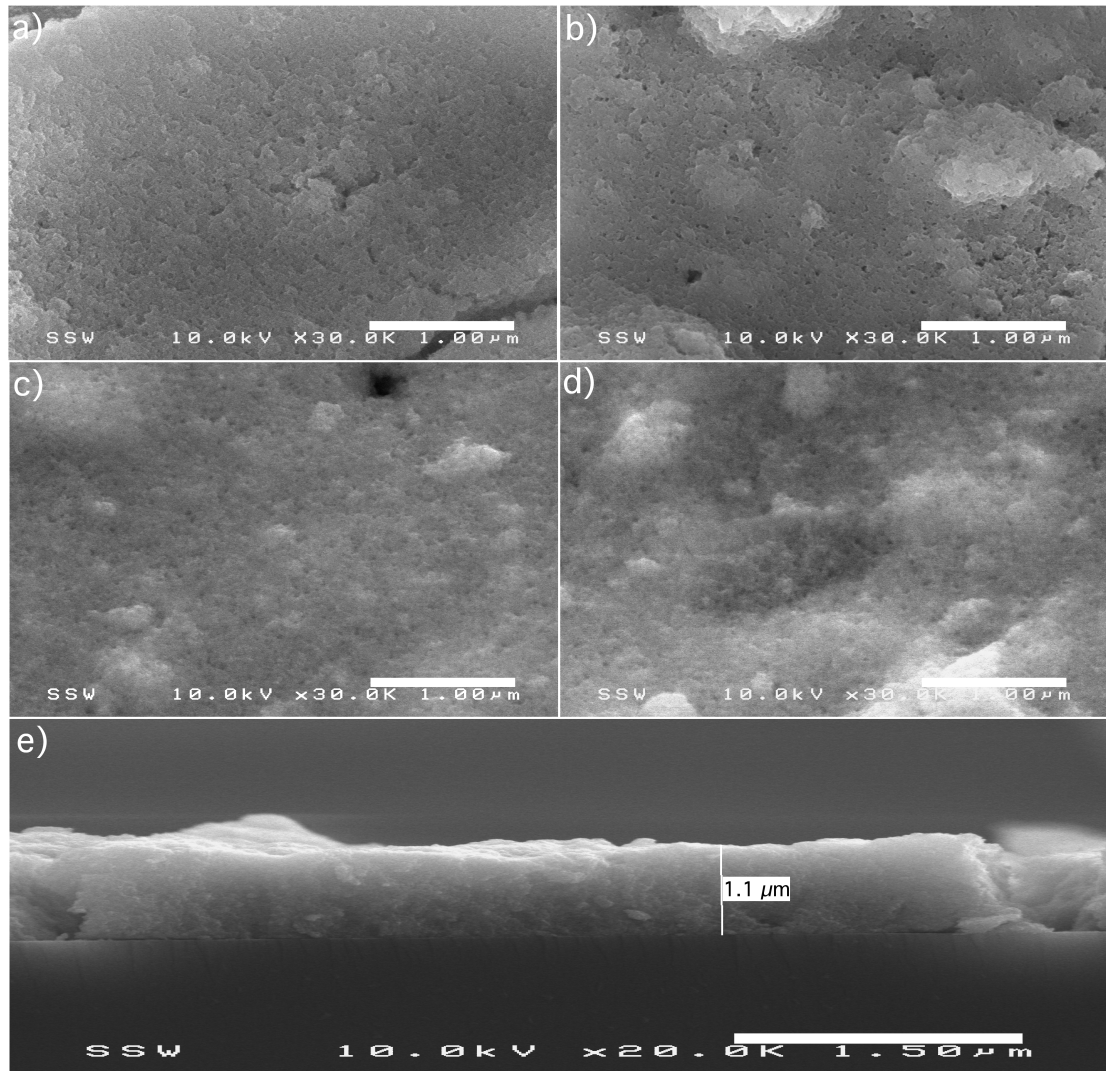
Figure 3.4. SEM images of CZTS for Cu-poor (a and c) and Cu-stoichiometric (b and d) films. NCs dropcasted using isopropanol (a and b) and acetone (c and d). Typical cross-section (e) of the deposited CZTS film with a thickness of 1.1 μm.

Figure 3.4 (a) and (c) represent the Cu-poor films whilst Figure 3.4 (b) and (d) are associated with the Cu-stoichiometric sample. In comparison, the Cu-poor films for both solvents appeared to have a more homogenous, compact and smooth surface, as opposed to the stoichiometric. The lower Cu-content resulted in a more condensed film and lead to an increase in the size of the NCs (indicated by XRD). This caused a decrease in the surface area, which corresponded to a reduction in the number of electron traps and grain boundaries. In theory this should influence the efficiency of the semiconductor.

Small cracks were visible in Figure 3.4 (a). The presence of these cracks are predominantly due to the deposition technique, as it resulted in uneven drying of the NCs.

Considering that these samples were not pre-treated, dropcasted and dried in open air, the length of these cracks were very small (1 μm-2 μm).

3.3.5. Photoelectrochemical Measurements

Figure 3.5 demonstrates the photocurrent over a linear potential sweep of the two light absorbing films on the FTO glass substrate. High photocurrent response is associated with a greater current density difference between the light on and light off responses.
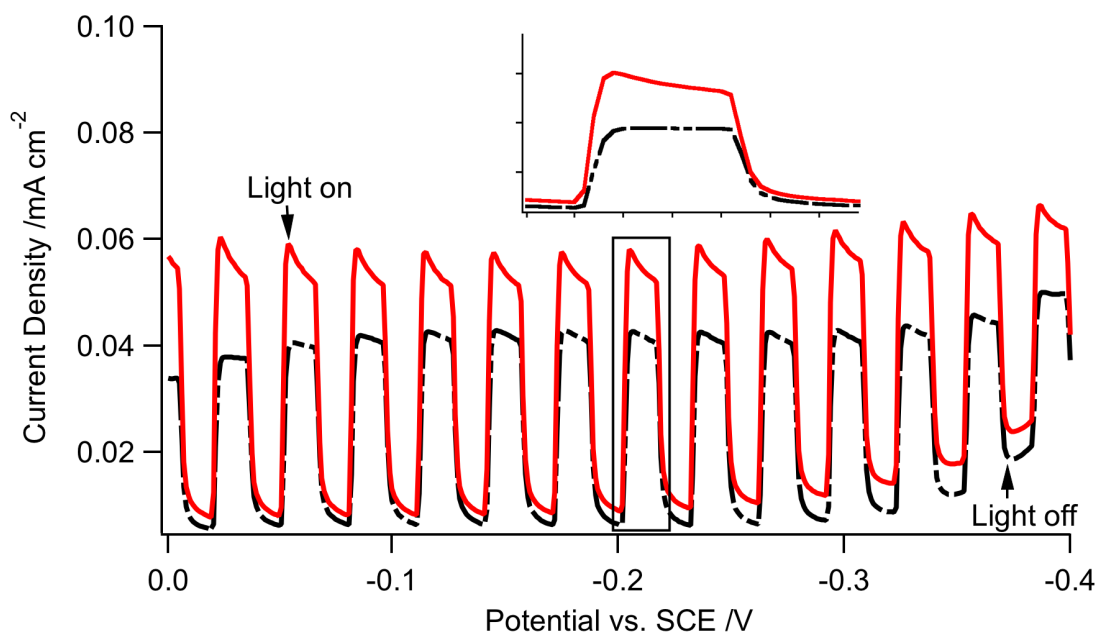
Figure 3.5. Chopped light PEC measurements for Cu-stoichiometric (black dashed line) and Cu-poor (red solid line) thin films, in aqueous 0.05 M MVCl₂ and 0.1 M KCl electrolyte solution. The linear potential sweep was applied at a scan rate of 5 mV/s with a 3 s light on/off exposure period. The inset shows transients at potentials ranging from -0.2 V to -0.22 V. These were magnified to show the difference in decay rates between the two samples.

Upon illumination (labeled light on in Figure 3.5), two initial processes occurred at the CZTS/electrolyte solution interface[35]: photoexcitation and electron transfer,

$$CZTS \xrightarrow{h\nu} e^- + h^+$$

$$CZTS^- + MV^{2+} \xrightarrow{k_{et}} [CZTS - MV^+]_{int}$$
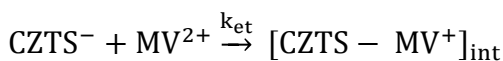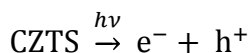
Scheme I

At the pseudo p-n junction, photogenerated electron-hole pairs are produced as a result of

photons striking the film (Scheme I). Electrons are then transferred to MV^{2+}, creating an electron-hole pair intermediate, $[CZTS^--MV^+]_{int}$. This process gives rise to a sharp increase in the photocurrent, which can be expressed as:

$$g_1 = k_{et}[CZTS^-][MV^{2+}] \tag{1}$$

The flux of minority carriers is defined as g. As shown in eqn (1)[36-37] the rate of electron transfer (k_{et}) is reflected in the initial rise of current in both films (Figure 3.5). The transient current density for the Cu-poor sample is larger and sharper, indicating a higher k_{et}. This is expected, as the reduced Cu content would lead to an increase in the overall positive charge in CZTS, causing greater electron flow at the semiconductor/solution interface, in the space charge region (SCR). The higher Cu content (Cu-stoichiometric film) creates a reduction in the number of holes, lowering the k_{et}; therefore, giving rise to a smaller transient. Surface defects also play a large role as they can reduce electron flow, creating a buildup of trapped holes.[38] These are more pronounced for the Cu-stoichiometric film, as seen in Figure 3.5, which further explains the lower and less prominent rise in current.

The electron transfer is followed by two processes,

$$[CZTS - MV^+]_{int} \xrightarrow{k_{ps}} CZTS + MV^+$$

$$[CZTS - MV^+]_{int} \xrightarrow{k_{rec}} CZTS + MV^{2+}$$
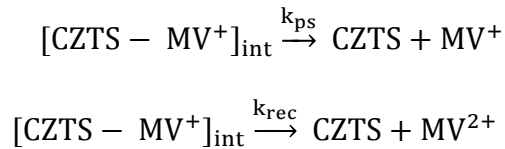
Scheme II

Scheme II describes the two competing processes of charge separation (k_{ps}) and recombination (k_{rec}), respectively. If the supplied external potential overcomes the internal bias, the electron-hole pair separates at the interface (k_{ps}) and produces a current. A reverse reaction can occur at the intermediate in which the electron recombines with MV^+ (k_{rec}), forming MV^{2+}. At this point a decay in the photocurrent could be seen,[36-37]

$$j_{photo} = g_1 \left[1 - \frac{k_{rec}}{k_{ps}+k_{rec}} (1 - \exp(-(k_{ps} + k_{rec})t))\right] \tag{2}$$

in which t represents the time between the initial and final decay.

When the light is turned off, a drop in the current is seen,[36-37]

$$j_{photo} = -\frac{k_{rec}g_1}{(k_{ps}+k_{rec})} \exp(-(k_{ps} + k_{rec})t) \tag{3}$$

This variable is still dependent on g_1. In both transients in Figure 3.5, the current does

not drop below zero, causing an overshoot, and confirms that the charge separation is still dominant in the absence of light. The overshoot effect, corresponding to complete recombination and partial recombination can be seen in Figure 3.6 (a) and (c). These simulation were created using eqns. (1) - (3).
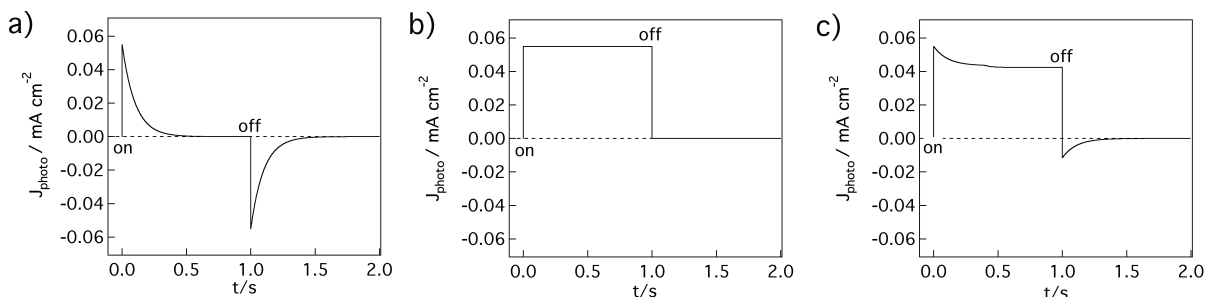
Figure 3.6. The simulations were calculated from equations 2 and 3 with g_1 of 9.3×10^{-3} A cm^{-2}: (a) Complete recombination, $k_{rec} \gg k_{ps}$ ($k_{ps}=0$, $k_{rec}=10$s^{-1}), (b) no recombination, $k_{rec} \ll k_{ps}$ ($k_{ps}=10$, $k_{rec}=0$ s^{-1}) and (c) partial recombination, $k_{rec} = 2.1$ s^{-1} and $k_{ps} = 7.9$ s^{-1}.

When comparing all the transient simulations in Figure 3.6 to that of the PEC measurements (Figure 3.5), both films resemble the "partial recombination", but without the negative overshoot. Furthermore, in reference to the transients seen in the inset of Figure 3.5, both indicate dominant k_{ps} and low k_{rec}, as a steep decay in the current is absent; however, the duration of the decay time is longer for the Cu-poor film reflecting a lower recombination rate than the Cu-stoichiometric. This also indicates that there is negligible metallic surface impurities and that the re-oxidation of MV^+ to MV^{2+} does not occur. The simulation in Figure 3.6 (b) is indicative of no recombination. The plateau at a constant current is not seen in either PEC. The above observations can be explained by the diffusion limitations of the electrons from the CZTS bulk to the interface and the MV^{2+} from the solution bulk to the interface. The effect of the diffusion was confirmed via PEC measurements conducted using various concentrations of MV^{2+} on our CuInS$_2$ working electrode.[39] The photoresponse in PEC measurements showed a slow rise when the MV^{2+} concentration was high, while it displayed a decay when the MV^{2+} concentration was low.[39] The diffusion effect can be distinguished by IMPS. In addition, when the MV^{2+} concentration is too high, film degradation can occur.

Overall, the lower Cu-content resulted in an enhancement in the photocurrent of the CZTS film. The photoresponse at -0.2V (Figure 3.5) is 53 µA/cm^2 for the Cu-poor sample and 36 µA/cm^2 for the Cu-stoichiometric. As several samples were dropcasted and tested, the

general range of the current density for Cu-deficient films was between 45 μA/cm^2 – 53 μA/cm^2 and 28 μA/cm^2 – 36 μA cm^2 for the stoichiometric-Cu samples. As shown via SEM images (Figure 3.4), the composition also affects the quality of the film and as indicated in Figure 3.5, this further influences the electronic properties of the semiconductor.

3.3.6. Intensity Modulated Photocurrent Spectroscopy

The recombination rates were quantified using IMPS. Figure 3.7 (a) displays the IMPS measurements of Cu-poor and Cu-stoichiometric thin films at applied potentials of -0.2 V and -0.3 V.
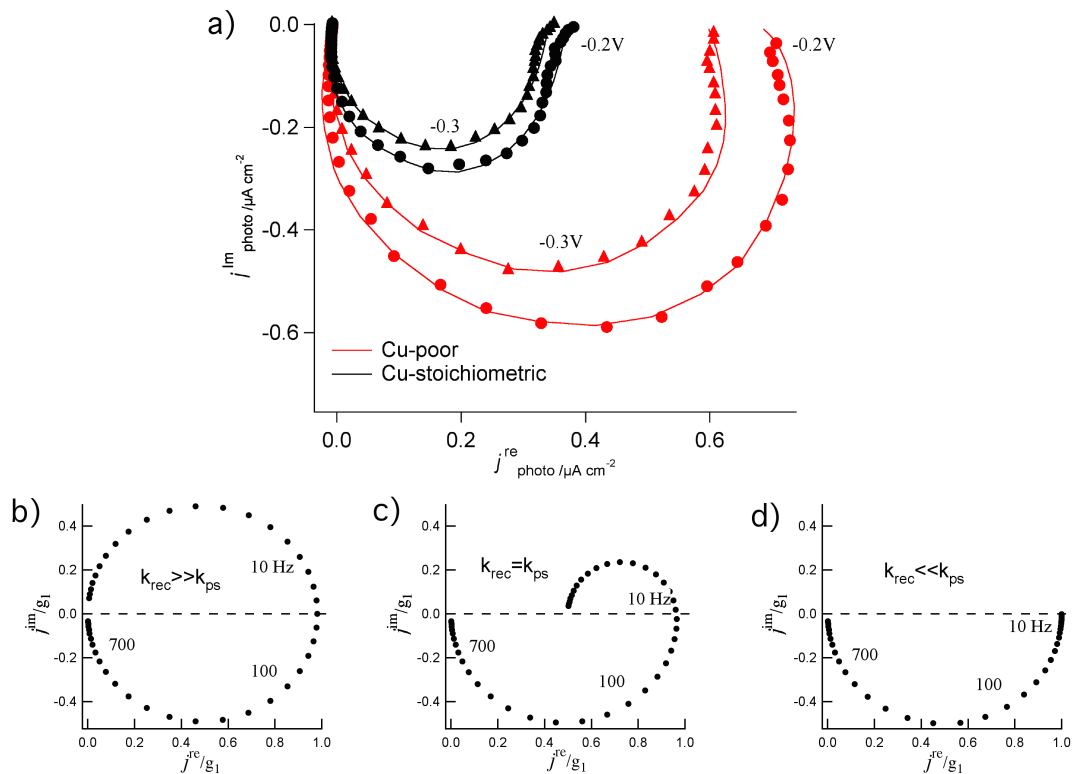
Figure 3.7. IMPS spectra of Cu-poor film and Cu-stoichiometric (a) at applied potentials of -0.2 V and -0.3 V with frequency range of 0.01 Hz – 1000 Hz. Three complex representations shown below the experimental plots indicating (b) $k_{rec} \gg k_{ps}$, (c) $k_{rec} \approx k_{ps}$ and (d) $k_{rec} \ll k_{ps}$.

The IMPS spectra are fitted based on a circuit containing a resistor (R) and capacitor (C) in series. The real and imaginary components of the photocurrent response, under illumination, are plotted as a function of the angular frequency (ω).

The shape of the IMPS plot also provides information associated with the product separation and the recombination conditions. The plots are then fitted using,[40-41]

$$\frac{j_{photo}^{re}}{g_1} = \frac{k_{ps}(k_{ps}+k_{rec})+\omega^2(RCk_{rec}+1)}{(RC^2\omega^2+1)[(k_{ps}+k_{rec})^2+\omega^2]} \qquad (4)$$

$$\frac{j_{photo}^{im}}{g_1} = \frac{\omega\,[k_{rec}-RC(k_{ps}(k_{ps}+k_{rec})-\omega^2)}{(RC^2\omega^2+1)[(k_{ps}+k_{rec})^2+\omega^2]} \qquad (5)$$

Given this, k_{rec} and k_{ps} can be quantitatively determined.

The three complex representations based on eqns. (4) and (5) are shown below the experimental plot.[42] A full circle (Figure 3.7 (b)) correlates to $k_{rec} \gg k_{ps}$, the two-semicircle plot, in which one is in the lower quadrant and one in the upper ((Figure 3.7 (c)) is typical for a process in which $k_{rec} \approx k_{ps}$ and the semi-circle (Figure 3.7 (d)) corresponds to dominant charge separation vs. recombination. At low frequencies the apparent competition between k_{rec} and k_{ps} is more pronounced ($\frac{k_{ps}}{k_{ps}+k_{rec}}$), while at high frequencies the photocurrent is attenuated by the RC time constant.[38] In comparison to these representations, both films depict dominant charge separation (Table 3.2). As shown in Table 3.2 the k_{rec} rate constant for the Cu-deficient was $1.1 s^{-1}$ and $0.89\ s^{-1}$ at potentials of -0.2 V and -0.3 V, respectively. Potentials of 0 V and -0.1 V were disregarded, as the recombination effect is more pronounced at lower potentials. The values obtained for the Cu-stoichiometric (at -0.2 V, 1.2 s^{-1} and at -0.3 V, 0.55 s^{-1}) were similar to that of Cu-poor; however the k_{ps} values confirmed that the Cu-stoichiometric sample contained a lower product separation rate than the Cu-deficient. This corresponds to the PEC transients, during illumination, indicating that the sharp rise and longer decay for the Cu-deficient sample corresponded to a higher separation rate. It is important to note that the RC attenuation alters the IMPS spectrums, whereas the RC is disregarded in the PEC measurements (Figure 3.5 and Figure 3.6). This explains as to why the simulation seen in Figure 3.6 (c) does not correspond to those experimentally obtained in Figure 3.5. The negative overshoot is not seen in Figure 3.5 and this deviation could be associated to the effect of RC and hidden by the diffusion of electrons and MV^{2+}, as explained in Section 3.5.

Table 3.2. k_{rec} and k_{ps} values for Cu-poor and Cu-stoichiometric samples, obtained via IMPS at -0.2V and -0.3V.

	Potential (V)	k_{ps} (s^{-1})	k_{rec} (s^{-1})
Cu-poor	-0.200	7.8 ± (0.1)	1.1 ± (0.8)
	-0.300	5.4 ± (0.9)	0.89 ± (0.1)
Cu-stoichiometric	-0.200	2.3 ± (0.2)	1.2 ± (0.4)
	-0.300	0.99 ± (0.3)	0.55 ± (0.1)

3.3.7. Chrono-Photoelectrochemical Measurements

Figure 3.8 depicts the photocurrent vs. time of both samples. Each scan was carried out for 800 seconds (Figure S1, Appendix) and further zoomed-in between 490 s-610 s (Figure 3.8). The films were tested at three constant potentials: -0.1 V (Figure 3.8 (a) and (b)), -0.2 V (Figure 3.8 (c) and (d)) and -0.3 V (Figure 3.8 (e) and (f)), respectively. The total performance of each film was evaluated for 2400 s. As shown in Figure 3.8 the photocurrent transients are steady and consistent, without any sign of degradation with time. The photoresponse at an applied potential of -0.2 V for the Cu-poor film was 45 µA/cm^2 (Figure 3.8 (c)) and 34 µA/cm^2 (Figure 3.8 (d)) for Cu-stoichiometric.
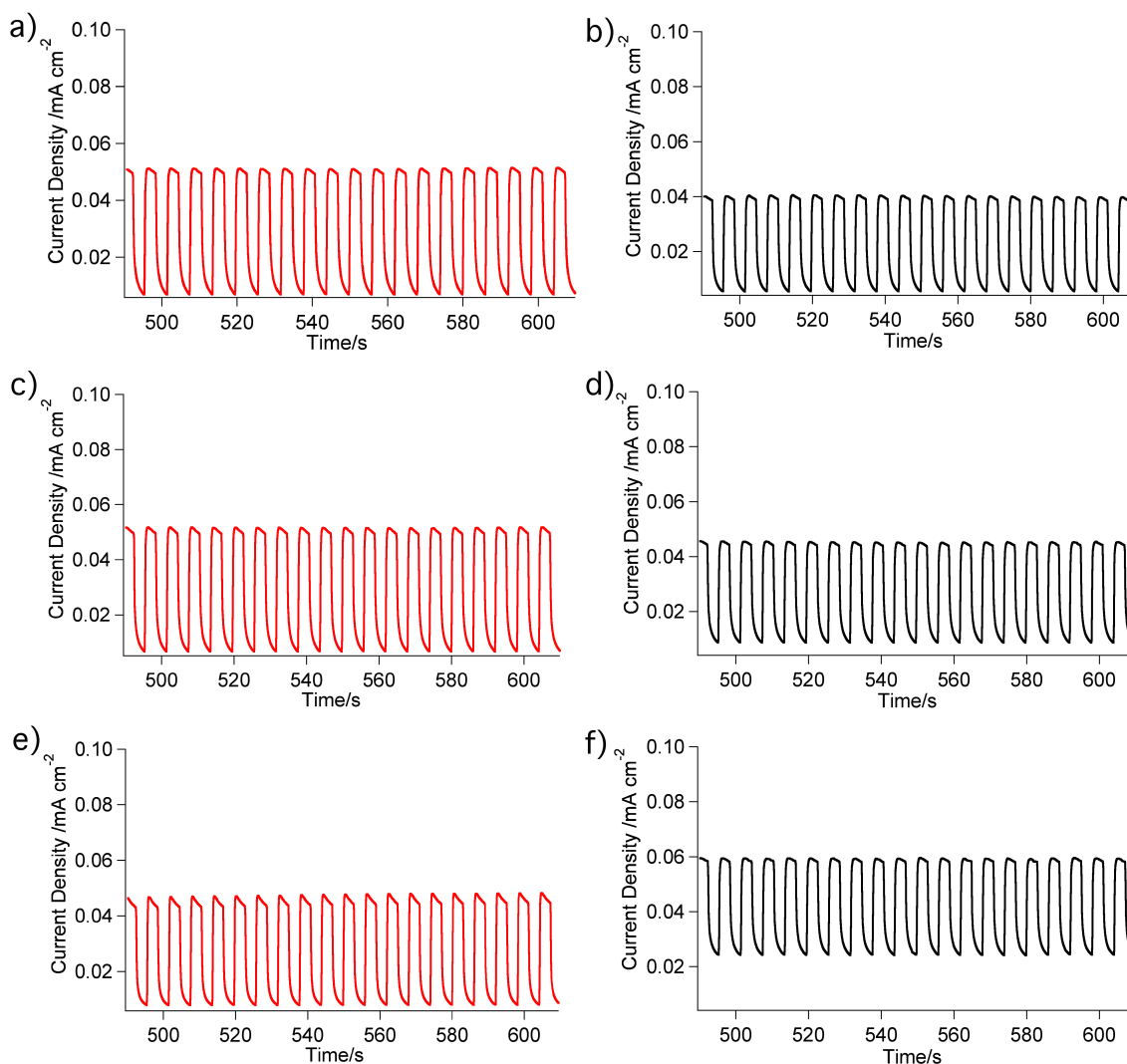
Figure 3.8. Amperometric *I-t* curves for Cu-poor (red) and Cu-stoichiometric (black) at applied potentials of -0.1V (a and b), -0.2V (c and d) and -0.3V (e and f) vs. SCE under chopped light illumination.

An increase in the dark current is seen for the Cu-stoichiometric film at applied potentials of -0.2V (Figure 3.8 (d)) and -0.3V (Figure 3.8 (f)). To further understand this effect, the resistance of both films was measured via the iR compensation method in the instrument. The capacitance was extracted from the RC constant obtained in IMPS. A summary of this data can be seen in Table 3.3.

Table 3.3. Resistance, capacitance and the RC constant values for Cu-poor and Cu-stoichiometric.

	Series Resistance (ohm)	Capacitance (F)	RC Constant (μs)
Cu-poor	5796	7.1×10^{-4}	4.1
Cu-stoichiometric	17792	2.2×10^{-4}	3.9

As the films were consecutively tested, from -0.1 V to -0.3 V, the resistance of the stoichiometric-Cu increased, as apparent in Figure 3.8 (d), Figure 3.8 (f), due to the unfavorable conditions created for the generation of a SCR.

The increase in negative potential (from -0.1 V to -0.3 V) draws from the available positive charge carriers within the CZTS film. This in turn, reduces electron flux within the solution at the interface, resulting in a weaker SCR and an increase in the resistance. The higher resistance is only slightly seen for the Cu-poor film and only starting at -0.3 V (Figure 3.8 (e)). One of the reasons for this could be because the more positively charged film is able to accept additional electrons from the circuit, due to the lower resistance and the higher capacitance. The increase in capacitance of the Cu-deficient film coheres to a decrease in bulk resistance at the SCR. As previously mentioned, the same volume of solution was dropcasted each time; however, the lower Cu content may have induced greater charge transfer by creating a more electron deficient film.

A notable feature that is exhibited in Figure 3.8 /Figure S1 (Appendix) is the stability and resistance of both films against photocorrosion. Corrosion of the films would have caused a significant decrease, followed by the disappearance of the photocurrent. This further confirms the high quality of the CZTS NCs.

3.3.8. Band Gap Evaluation

In order to determine the optical properties of the two samples, absorbance measurements were taken via use of UV-vis spectroscopy. Figure 3.9 illustrates high absorption over the experimental wavelength range (Figure 3.9 (a)) and the direct energy band gap (Figure 3.9 (b)) for crystals of both compositions. The band gap for each composition falls within the expected range for CZTS NCs, indicating the suitability of both compositions for absorber layer usage in solar cell device fabrication.[30, 43-44] The minor

reduction in the band gap as a result of increasing Cu content is within expected error margins, thus showing no significant trends between absorption and Cu content.
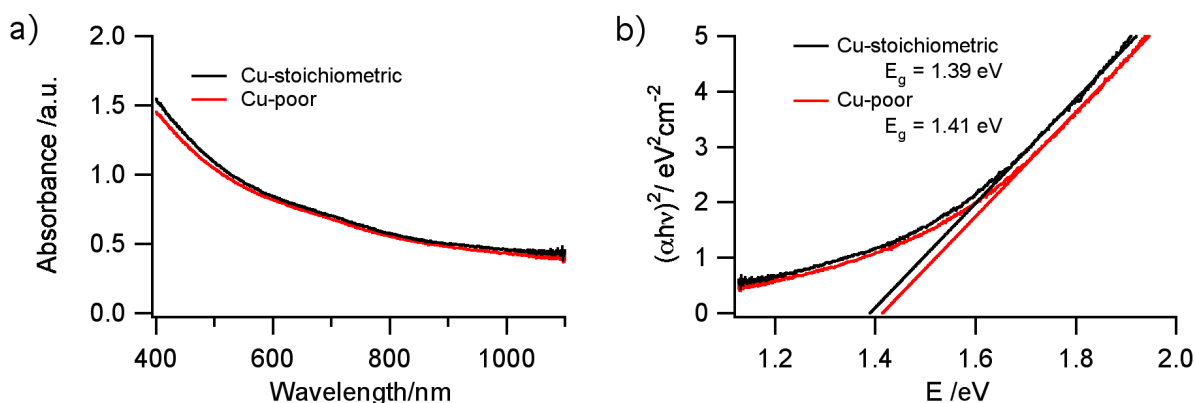
Figure 3.9. UV-vis spectra indicating (a) absorption as a function of wavelength and (b) band gap using Tauc plots for the Cu-stoichiometric (black) and Cu-poor (red) thin films.

3.4. Conclusions

Compositional determination via EDX and XRF confirmed the fabrication of films with different Cu contents. Film qualities were tested using multiple solvents for both compositions. Regardless of solvent choice, films comprised of Cu-poor CZTS showed tighter packing with less defects compared to those of stoichiometric-Cu. The decrease in cracking on film defects suggested that the lower Cu-content led to improved uniformity within crystals. In terms of crystal phase, this suggests a more uniform phase crystal is present in the Cu-poor films. This was confirmed through the use of XRD and Raman via evaluation of the peak intensities and positions. The absence of detrimental secondary phases was further confirmed with Raman spectroscopy.

The Cu-poor film exhibited increased photoconversion and lower resistance over the Cu-stoichiometric sample. The PEC transients indicated that the photoinduced charge separation is dominant over charge recombination in both cases; however, the decay time variation points to a slight increase in charge recombination in the stoichiometric case. The improved product separation in Cu-poor films previously noted in the PEC measurements was verified through the use of IMPS. The product separation rate (k_{ps}) was quantified using IMPS, which showed that the Cu-deficient NC film was more than 3 times that of the Cu-stoichiometric, at both applied potentials of -0.2 V and -0.3 V. Furthermore, iR compensation

measurements indicated that the resistance of the Cu-stoichiometric film was higher than the Cu-poor, this was also observed in the shift in the dark current via Chrono-PEC measurements.

The reduced defects and improved crystallinity appear to be the reason for the improvements noted through PEC and IMPS measurements. This supports the idea that stoichiometry plays a crucial role in not only the physical properties of a CZTS thin film, but also its electronic and interfacial properties.

3.5. References

1. Lafond, A.; Choubrac, L.; Guillot-Deudon, C.; Fertey, P.; Evain, M.; Jobic, S., X-ray resonant single-crystal diffraction technique, a powerful tool to investigate the kesterite structure of the photovoltaic Cu_2ZnSnS_4 compound. *Acta Crystallographica Section B* **2014,** *70*, 390.

2. Suryawanshi, M. P.; Agawane, G. L.; Bhosale, S. M.; Shin, S. W.; Patil, P. S.; Kim, J. H.; Moholkar, A. V., CZTS based thin film solar cells: a status review. *Materials Technology* **2013,** *28*, 98.

3. Zhou, H.; Hsu, W.-C.; Duan, H.-S.; Bob, B.; Yang, W.; Song, T.-B.; Hsu, C.-J.; Yang, Y., CZTS nanocrystals: a promising approach for next generation thin film photovoltaics. *Energy & Environmental Science* **2013,** *6*, 2822.

4. Chen, S.; Gong, X. G.; Walsh, A.; Wei, S.-H., Defect physics of the kesterite thin-film solar cell absorber Cu_2ZnSnS_4. *Applied Physics Letters* **2010,** *96*, 021902.

5. Chen, S.; Yang, J.-H.; Gong, X. G.; Walsh, A.; Wei, S.-H., Intrinsic point defects and complexes in the quaternary kesterite semiconductor Cu_2ZnSnS_4. *Physical Review B* **2010,** *81*, 245204.

6. Stanbery, B. J., Copper indium selenides and related materials for photovoltaic devices. *Critical Reviews in Solid State and Materials Sciences* **2002,** *27*, 73.

7. Zhang, S.; Wei, S.-H.; Zunger, A.; Katayama-Yoshida, H., Defect physics of the $CuInSe_2$ chalcopyrite semiconductor. *Physical Review B* **1998,** *57*, 9642.

8. Flammersberger, H. Experimental study of Cu_2ZnSnS_4 thin films for solar cells. *MSc. dissertation.* Uppsala University: Sweden, 2010.

9. Berg, D. M.; Dale, P. J., Kesterites. In *Copper Zinc Tin Sulfide-Based Thin-Film Solar Cells*, Wiley: Chichester, 2015, 107.

10. Fairbrother, A.; García-Hemme, E.; Izquierdo-Roca, V.; Fontané, X.; Pulgarín-Agudelo, F. A.; Vigil-Galán, O.; Pérez-Rodríguez, A.; Saucedo, E., Development of a Selective Chemical Etch To Improve the Conversion Efficiency of Zn-Rich Cu_2ZnSnS_4 Solar Cells. *Journal of the American Chemical Society* **2012,** *134*, 8018.

11. Nadeem, M.; Ahmed, W., Optical properties of ZnS thin films. *Turkish Journal of Physics* **2000,** *24*, 651.

12. Scragg, J. J., *Copper Zinc Tin Sulfide Thin Films for Photovoltaics: Synthesis and*

Characterisation by Electrochemical Methods. Springer: Berlin, 2011.

13.   Katagiri, H.; Jimbo, K.; Yamada, S.; Kamimura, T.; Maw, W. S.; Fukano, T.; Ito, T.; Motohiro, T., Enhanced conversion efficiencies of Cu_2ZnSnS_4-based thin film solar cells by using preferential etching technique. *Applied Physics Express* **2008,** *1*, 041201.

14.   Tanaka, K.; Oonuki, M.; Moritake, N.; Uchiki, H., Cu_2ZnSnS_4 thin film solar cells prepared by non-vacuum processing. *Solar Energy Materials and Solar Cells* **2009,** *93*, 583.

15.   Araki, H.; Mikaduki, A.; Kubo, Y.; Sato, T.; Jimbo, K.; Maw, W. S.; Katagiri, H.; Yamazaki, M.; Oishi, K.; Takeuchi, A., Preparation of Cu_2ZnSnS_4 thin films by sulfurization of stacked metallic layers. *Thin Solid Films* **2008,** *517*, 1457.

16.   Wang, J.; Zhang, P.; Song, X.; Gao, L., Surfactant-free hydrothermal synthesis of Cu_2ZnSnS_4 (CZTS) nanocrystals with photocatalytic properties. *Royal Society of Chemistry Advances* **2014,** *4*, 27805.

17.   Tapley, A.; Hart, C.; Vaccarello, D.; Love, D. A.; Ding, Z., Effect of annealing on the photoelectrochemical behavior of $CuInS_2$ nanocrystal films. *Journal of the Electrochemical Society* **2014,** *161*, H725.

18.   Tapley, A.; Vaccarello, D.; Hedges, J.; Jia, F.; Love, D. A.; Ding, Z., Preparation and characterization of $CuInS_2$ nanocrystals for photovoltaic materials. *Physical Chemistry Chemical Physics* **2013,** *15*, 1431.

19.   Talapin, D. V.; Lee, J.-S.; Kovalenko, M. V.; Shevchenko, E. V., Prospects of colloidal nanocrystals for electronic and optoelectronic applications. *Chemical Reviews* **2009,** *110*, 389.

20.   Wei, W.; Lu, Y.; Chen, W.; Chen, S., One-pot synthesis, photoluminescence, and electrocatalytic properties of subnanometer-sized copper clusters. *Journal of the American Chemical Society* **2011,** *133*, 2060.

21.   Shavel, A.; Cadavid, D.; Ibanez, M.; Carrete, A.; Cabot, A., Continuous production of Cu_2ZnSnS_4 nanocrystals in a flow reactor. *Journal of the American Chemical Society* **2012,** *134*, 1438.

22.   Jones, F. W., The measurement of particle size by the X-Ray method. *Proceedings of the Royal Society of London A* **1938,** *166*, 16.

23.   Mao, L.; Li, J.; Xie, Y.; Zhong, Y.; Hu, Y., Controllable growth of SnS_2/SnO_2

heterostructured nanoplates via a hydrothermal-assisted self-hydrolysis process and their visible-light-driven photocatalytic reduction of Cr(vi). *Royal Society of Chemistry Advances* **2014,** *4*, 29698.

24.   Zhao, Y.; Burda, C., Development of plasmonic semiconductor nanomaterials with copper chalcogenides for a future with sustainable energy materials. *Energy & Environmental Science* **2012,** *5*, 5564.

25.   Wu, G.; Thind, S. S.; Wen, J.; Yan, K.; Chen, A., A novel nanoporous α-C_3N_4 photocatalyst with superior high visible light activity. *Applied Catalysis B: Environmental* **2013,** *142-143*, 590.

26.   Ji, S.; Shi, T.; Qiu, X.; Zhang, J.; Xu, G.; Chen, C.; Jiang, Z.; Ye, C., A route to phase controllable $Cu_2ZnSn(S_{1-x}Se_x)_4$ nanocrystals with tunable energy bands. *Scientific Reports* **2013,** *3*, 2733.

27.   Sarkar, S.; Bhattacharjee, K.; Das, G. C.; Chattopadhyay, K. K., Self-sacrificial template directed hydrothermal route to kesterite-Cu_2ZnSnS_4 microspheres and study of their photo response properties. *CrystEngComm* **2014,** *16*, 2634.

28.   Tiong, V. T.; Bell, J.; Wang, H., One-step synthesis of high quality kesterite Cu_2ZnSnS_4 nanocrystals - a hydrothermal approach. *Beilstein Journal of Nanotechnology* **2014,** *5*, 438.

29.   Fernandes, P. A.; Salomé, P. M. P.; da Cunha, A. F., Study of polycrystalline Cu_2ZnSnS_4 films by Raman scattering. *Journal of Alloys and Compounds* **2011,** *509*, 7600.

30.   Mitzi, D. B.; Gunawan, O.; Todorov, T. K.; Wang, K.; Guha, S., The path towards a high-performance solution-processed kesterite solar cell. *Solar Energy Materials and Solar Cells* **2011,** *95*, 142.

31.   Kosyak, V.; Karmarkar, M. A.; Scarpulla, M. A., Temperature dependent conductivity of polycrystalline Cu_2ZnSnS_4 thin films. *Applied Physics Letters* **2012,** *100*, 263903.

32.   Lin, X.; Kavalakkatt, J.; Kornhuber, K.; Levcenko, S.; Lux-Steiner, M. C.; Ennaoui, A., Structural and optical properties of Cu_2ZnSnS_4 thin film absorbers from ZnS and Cu_3SnS_4 nanoparticle precursors. *Thin Solid Films* **2013,** *535*, 10.

33.   Guo, Q.; Ford, G. M.; Yang, W.-C.; Walker, B. C.; Stach, E. A.; Hillhouse, H. W.; Agrawal, R., Fabrication of 7.2% efficient CZTSSe solar cells using CZTS nanocrystals.

Journal of the American Chemical Society **2010,** *132*, 17384.

34.   Todorov, T. K.; Reuter, K. B.; Mitzi, D. B., High-efficiency solar cell with earth-abundant liquid-processed absorber. *Advanced Energy Materials* **2010,** *22*, E156.

35.   Peter, L. M., Dynamic aspects of semiconductor photoelectrochemistry. *Chemical Reviews* **1990,** *90*, 753.

36.   Peter, L. M.; Ponomarev, E. A.; Fermín, D. J., Intensity-modulated photocurrent spectroscopy: reconciliation of phenomenological analysis with multistep electron transfer mechanisms. *Journal of Electroanalytical Chemistry* **1997,** *427*, 79.

37.   Fermin, D. J.; Ding, Z. F.; Duong, H. D.; Brevet, P. F.; Girault, H. H., Photoinduced electron transfer at liquid/liquid interfaces. I. Photocurrent measurements associated with heterogeneous quenching of zinc porphyrins. *Journal of Physical Chemistry B* **1998,** *102*, 10334.

38.   Peter, L. M.; Wijayantha, K. G. U.; Tahir, A. A., Kinetics of light-driven oxygen evolution at α-Fe_2O_3 electrodes. *Faraday Discussions* **2012,** *155*, 309.

39.   Vaccarello, D.; Hedges, J.; Tapley, A.; Love, D. A.; Ding, Z., Dynamic aspects of $CuInS_2$ light absorbing nanocrystal thin films. *Journal of Electroanalytical Chemistry* **2015,** *738*, 35.

40.   Schaming, D.; Hojeij, M.; Younan, N.; Nagatani, H.; Lee, H. J.; Girault, H. H., Photocurrents at polarized liquid|liquid interfaces enhanced by a gold nanoparticle film. *Physical Chemistry Chemical Physics* **2011,** *13*, 17704.

41.   Bard, A. J.; Faulkner, L. R., *Electrochemical Methods: Fundamentals and Applications*. Wiley: New York, 2000.

42.   Fermin, D. J.; Dung, D. H.; Ding, Z.; Brevet, P. F.; Girault, H. H., Photoinduced electron transfer at liquid/liquid interfaces Part II. A study of the electron transfer and recombination dynamics by intensity modulated photocurrent spectroscopy (IMPS). *Physical Chemistry Chemical Physics* **1999,** *1*, 1461.

43.   Katagiri, H.; Jimbo, K.; Maw, W. S.; Oishi, K.; Yamazaki, M.; Araki, H.; Takeuchi, A., Development of CZTS-based thin film solar cells. *Thin Solid Films* **2009,** *517*, 2455.

44.   Siebentritt, S.; Schorr, S., Kesterites-a challenging material for solar cells. *Progress in Photovoltaics: Research and Applications* **2012,** *20*, 512.

Chapter 4. Thin Film Deposition and Device Fabrication

Upon optimization of the CZTS recipe, the Cu-poor composition was further analyzed. Considering that dropcast followed by air-drying lead to the presence of cracks, different deposition techniques were investigated. Section 4.1 gives relevant background information on different deposition techniques, in accordance with the ones investigated in this chapter. The necessary layers required for full device fabrication are also described in this section. Section 4.2 and 4.3 include the experimental techniques and a joule heating simulation, respectively. The experimental data presented in Section 4.4 is structured in two parts: the first presents the information involving the three deposition methods used, while the second includes the preliminary results of a full device.

4.1. Background

4.1.1. Deposition Techniques for CZTS Absorbing Layers

Coating methods can influence a solar cells opto-electronic properties, as different fabrication conditions impact a films morphology and structure.[1-3] An ideal deposition process would be one that is simple with high reproducibility and of low cost. Majority of CZTS thin film fabrication processes include two-stages. The first includes preparation and deposition and the second, annealing in a S or Se atmosphere.[4-5] The highest efficiency CZTS devices have involved these two processes.[6-9]

Deposition methods can be broadly subdivided into two categories: physical and chemical.[10] Physical methods generally refer to vapor depositions in a vacuum environment, such as sputtering or co-evaporation.[11] Chemical techniques involve gas phase or solution-based depositions.[12] The CZTS fabrication techniques investigated were dip-coating, joule heating and spin-coating; all of which fall under the chemical liquid deposition (CLD) processes.

The dip-coating method, also known as vertical deposition, involves the immersion of a substrate into the coating solution followed by a gradual withdrawal. A desired thickness can be achieved via multiple dipping cycles and control over the dipping time, with reference to the solvent used. For CZTS thin films this technique has been successfully applied for

preparing precursor films or depositing CZTS during the phase-growth synthesis.[13-14]

Joule heating involves the passage of a current through a material, with an associated resistance, to generate heat. It simply converts electrical energy into thermal energy. A recent study used this technique to assist in the deposition of CuInGaSe$_2$ thin films.[15] Joule heating was applied to heat the Mo-coated substrate during the pulsed electron deposition (PED) of the NCs. Rampino et al. showed a significant improvement in film quality and overall grain size of the samples deposited with assistance using this technique vs. films without. In reference to this work, deposition was done in a similar manner with the difference being that dropcast was used to deposit the NCs as oppose to PED. The idea being that the consistent temperature throughout the film would induce a more homogeneous evaporation of the solvent.

Deposition using the spin-coating method consists of the initial placement of a substrate on a chuck, which is held down via the use of a vacuum. A drop of the sample is then deposited onto the substrate while it is spinning at the desired speed. The centripetal force allows the sample to spread over the back contact and can cause some solvents to simultaneously evaporate. Similar to dip-coating, this process is repeated until the desired thickness is reached. Currently, the highest efficiency CZTS device has been fabricated using this technique.[8] As discussed in the Introduction Todorov et al. used a hydrazine pure-solution to spin-coat the NCs and further annealed the films. They managed to achieve an energy conversion efficiency of 12.6%, which holds the world record for CZTS devices. Overall, spin-coating continues to be a popular deposition technique for CZTS thin films, due to its low cost and uniform output.[8-9, 16-19]

4.1.2. Device Architecture of a CZTS Device

The second layer predominantly used for CZTS device fabrications is CdS (Figure 4.1); however, as previously indicated prior to the deposition of CdS the CZT precursor metals or CZTS thin films are nearly always annealed in the presence of sulfur/selenium. This is done in an inert atmosphere to prevent oxidation. This step has been shown to improve CZTS crystallinity as it induces grain growth and overall film quality.[20-21] This enhancement in grain size can lead to an increase in the final device efficiency.
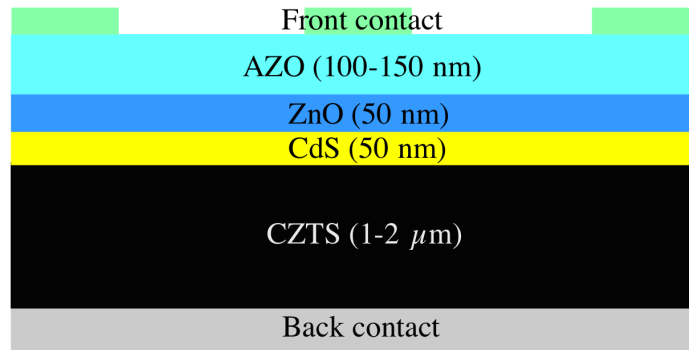
Figure 4.1. Layers of a CZTS solar cell device.

CdS is an n-type buffer layer with a band gap of 2.42 eV.[22] The wide band gap allows for easy light transmission to the CZTS layer without causing substantial absorption loss.[23] It is frequently used in thin film solar cells due to its high photoconductivity, low resistivity, stability and high electron affinity.[22, 24] This layer is commonly deposited using chemical bath deposition (CBD), as it is an inexpensive technique and does not damage the CZTS layer.[23-24] The n-type coating will form a continuous film on top of the p-type semiconductor, blocking any of the exposed back contact. This will minimize charge recombination because the charge carriers would need to travel a shorter distance, resulting in an overall enhancement in the photoresponse. It also creates a pathway for electrons in the preferred direction and creates a built-in p-n junction. Overall it serves to protect the CZTS thin film during the deposition of the final n-type semiconductor.

The layer following CdS is an n-type window layer (Figure 4.1). The most commonly used is a ZnO bilayer comprising of intrinsic ZnO (i:ZnO) and aluminum-doped ZnO (AZO). ZnO contains a wide band gap of 3.4 eV, which lies in the near-UV spectral range.[25] The i:ZnO layer is deposited on top of the CdS buffer and serves to cover pinholes which reduces the potential for shunting effects.[26] The AZO functions as the front contact due to its high transparency (transmittance > 85%) and low electrical resistivity ($1.9 \times 10^{-4} \, \Omega$ cm).[27] These layers are commonly deposited via sputtering; however, atomic layer deposition (ALD) is a growing alternative method.[28-30] ALD is a chemical vapor deposition technique in which produces highly conformal coatings on an atomic scale. It involves alternate exposure of reactants, to synthesize films in successive monolayers.[31]

An anti-reflection coating and a metal top contact (Figure 4.1) is placed on top of AZO. The top contacts most commonly used are Ni/Al grids, as they provide an ohmic

contact with the n-type layer.[6, 32] The current is transferred from the AZO to the metallic contact which is connected to an external load.[33] The top contact enhances the electrical contact, while the anti-reflection coating reduces the loss of light as a result of reflection.

4.2. Experimental

Chemicals were as described in Section 2.2.1 and Section 3.2 with the addition of sulfur (99.98%) and cadmium acetate hydrate (99.99+%), which were purchased from Sigma-Aldrich. Ammonium hydroxide (29.0-30.0%) and ethylene glycol (≥99.0%), from Caledon, were also used. Preparation of CZTS NCs were as described in Section 2.2.2. The starting ratio of copper: zinc: tin: sulfur for the Cu-poor sample was 0.89: 1.47: 1.00: 3.79. The FTO substrates were cleaned using the same procedure described in Section 3.2.1. The Mo coated subsrates (Guardian EcoGuard, 3 mm thickness, sheet resistance ~ 0/55 Ω/sq) were rinsed with ethanol twice and dried using argon gas.

4.2.1. Deposition Techniques used to Prepare CZTS Thin Films

Spin-coating

Upon dispersion of CZTS NCs in isopropanol (Section 3.2.1), a drop of the sample is deposited onto the substrate while spinning at 2500 rpm for 30 s. The centripetal force allows the sample to spread over the substrate. This process was repeated 23 times for FTO and 20 times for Mo. Once completed the sample was left to dry to ensure complete evaporation of the solvent.

Joule heating

Electrodes were attached to opposite sides of the coated substrate. These were connected to a DC voltage generator (Keithley 2400 SourceMeter). The voltage was set to 21V and the desired current was set. A drop of the sample was then dispersed onto the surface and left to dry.
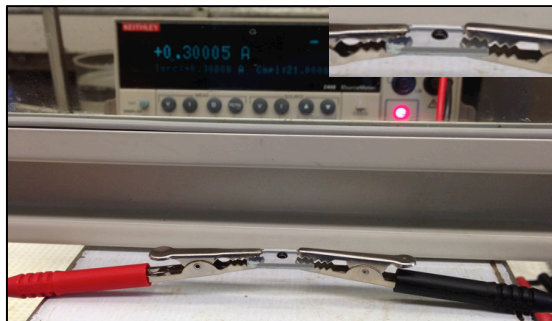
Figure 4.2. Joule heating apparatus. Electrodes attached to both sides of the conductive coated substrate while a current is applied. The inset demonstrates a zoomed-in image of the dropcast CZTS NCs.

Dip-coating

The substrate was placed in the reaction vial as crystallization was occurring at 180°C in atmospheric pressure. The crystallization step has been previously discussed in Section 2.2.2. After 10 min the coated back contact was removed and the nanocrystals remaining in the solvent were discarded. This procedure was repeated for each coating. The samples were then rinsed using isopropanol and left to dry.

4.2.2. Sulfurization of Thin Films

The samples were sulfurized in an annealing furnace (Lindberg/Blue M tube furnace, Thermo Scientific). Initially the samples were placed on a stage and loaded into a quartz tube along with 15mg of solid S. This was then placed in the furnace and sealed. The system was then purged with Ar gas 4-5 times, to remove any oxygen. The temperature was then set to 250°C for 20 min and then ramped up 550°C for 30 min. The chamber was then left to cool and the sulfurized samples were removed at ~25°C.

4.2.3. CdS Deposition

Cadmium sulfide (CdS) was deposited onto the CZTS layer via chemical bath deposition. The procedure used was similar to that reported by Lei, B. and colleagues.[34] Cadmium acetate ($Cd(OAc)_2$), 1M ammonium acetate (NH_4OAc), 0.5M thiourea and ammonium hydroxide were placed in a beaker containing DI water. The bath temperature was set to 65 °C and the CZTS samples were placed in the solution for 30 min. Once completed the samples were rinsed with DI water and placed on a hot plate set to 100 °C for 30 min to remove any trapped water within the samples.

4.2.4. Intrinsic ZnO and Al-doped ZnO Deposition and Top Contact

The i:ZnO and AZO were deposited using atomic layer deposition (Cambridge Nanotech Savannah S200 ALD). To deposit the layers, the system was first purged with Ar gas. Ar was set to 20 sccm, the chamber temperature was set to 200°C and the pressure was ~10^{-1} mbar. To deposit ZnO, first the precusor for zinc (diethyl zinc, 95%, Strem Chemicals Inc.) was pulsed for 15 ms, thereafter the pressure was equilibrated for 15 s. Water was then pulsed into the system for 15 ms and equilibrated for 15 s. The process was repeated for 300 cycles (thickness of 1.67 Å/cycle) to create 50nm of ZnO. AZO was deposited in a similar manner, the only difference was that the pulse time and equilibration times were shortened to 8 ms. After every 10th cycle of Zn and H_2O, Al (trimethylaluminum, 98%, Strem Chemicals Inc) was pulsed into the system to create a 5% Al doping in ZnO. This step was repeated for 51 cycles to create an AZO layer with a thickness of 150nm. A general representation of the sequential pulsing of the precursors is demonstrated in Figure 4.3. The CZTS film, coated with CdS, is placed on what is called a platen and ZnO or AZO is pumped into the system (A). Excess reactants and/or byproducts are removed by purging, thereafter water is introduced (B) and this process is repeated for several cycles until the desired thickness is achieved.

In order test the efficiency of the device after the ZnO and AZO depositions, small pieces of In metal were used as the top contact. Grid lines were made using a razor blade and a very small piece of In was cut and placed in the corner of each rectangle (3x4 mm).
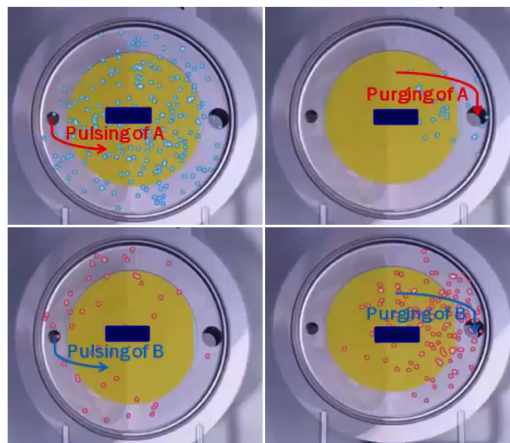

Figure 4.3. The sequential steps which occur to deposit ZnO or AZO, using ALD. Pulse A represents the first precursor (diethyl zinc or trimethylaluminum) and pulse B corresponds to water.

4.2.5. Characterization

The PEC measurements and SEM used for characterization were the same as described in Section 3.2.2. The device efficiency was measured using the same Ivium CompactStat instrument used for IMPS (Section 3.2.2). The IV curves were generated upon the use of standard test conditions. The measurements were recorded at room temperature (~25°C), using a light source that corresponded with the AM1.5 spectrum, which is representative of sunlight. An illumination intensity of 100 mW cm^{-2} was used. These measurements were also repeated in the absence of light.

4.3. Results and Discussion

4.4.1. Thin Film Fabrication using the Dip-coating Method

The dip-coating technique involved the self-assembly of the CZTS NCs onto the substrate during the synthesis, simultaneously. Specifically, the substrate was placed motionless in the hot reaction vial as crystallization was occurring (180 °C), with the intention of CZTS adhering to the coated glass in a more compact and uniform manner. The efficiencies of these films were tested via PEC measurements (Figure 4.4 and Figure 4.5) CZTS was deposited on both FTO (Figure 4.4) and Mo coated glass (Figure 4.5).
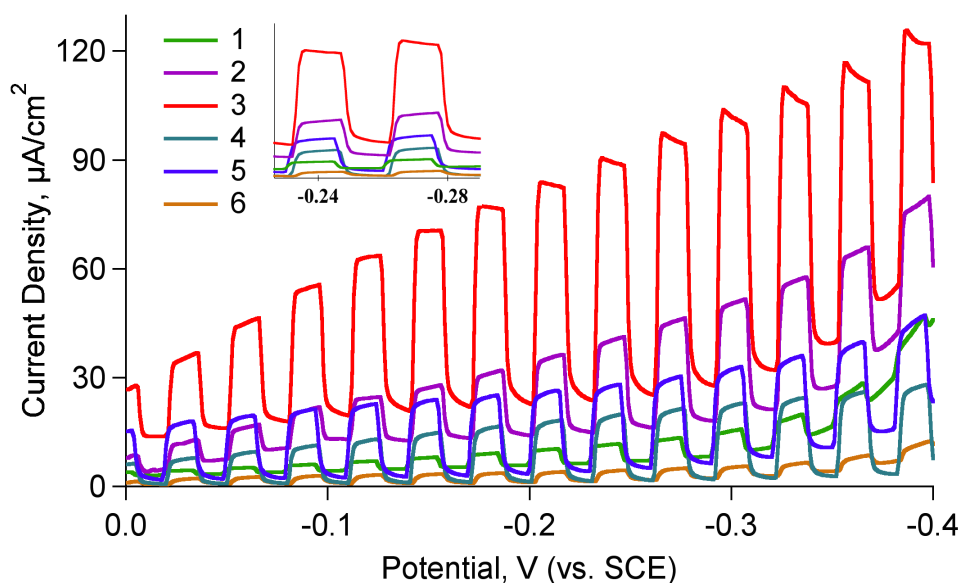

Figure 4.4. The PEC measurements of CZTS deposited on FTO glass. 1-6 represent the number of times the substrate was placed in the reaction vial, corresponding to the number of layers deposited.

In reference to the FTO samples (Figure 4.4) the range of photoresponse between -0.2V and -0.4V, for the 1, 2, 3, 4, 5 and 6 layers were 3-6 $\mu A/cm^2$, 23-35 $\mu A/cm^2$ and 65-76 $\mu A/cm^2$, 15-21 $\mu A/cm^2$, 20-26 $\mu A/cm^2$ and 2-3 $\mu A/cm^2$ respectively. The 3 layer deposition showed the highest photocurrent and this diminished upon additional depositions (4, 5 and 6 layers). The monolayer and bilayer were likely too thin to completely block the exposed back contact and as a result lead to low photocurrents. The third layer of CZTS most likely blocked the exposed substrate and filled in any remaining cracks on the surface, allowing better electron flow. The photocurrent for the 3 layer CZTS is also higher than that of the dropcast sample shown in Figure 4.4 (45-53 $\mu A/cm^2$). This could be because the NCs are more tightly bound and better adhered to the substrate, allowing greater electron flow, in turn a higher photoresponse.

The low photocurrent observed in layers 4, 5 and 6 could be due to the thickness of the film. Most likely, the extra layers lead to a film that was too dense, which limited electron transfer causing a decrease in the photocurrent. Furthermore, as shown in the inset, the transients contain a different shape than the 3 layer CZTS. Clearly visible for the 2, 4 and 5 layers, the initial increase of current is slower and not as distinct as the 3-layer sample. This suggests that the pace in which the electron is able to transfer through the film and into the SCR is occurring at a slower rate vs. the 3-layer CZTS.

The range of the photocurrent for CZTS deposited on Mo (Figure 4.5) between -0.2V and -0.4V, for the 1, 2, 3, 4, 5 and 6 depositions were 6-7 $\mu A/cm^2$, 15-26 $\mu A/cm^2$, 25-42 $\mu A/cm^2$, 85-108 $\mu A/cm^2$, 60-73 $\mu A/cm^2$ and 69-93 $\mu A/cm^2$, respectively. The 4-layer film had the highest photoresponse followed by the 6th and 5th. The differences between the FTO coated CZTS and Mo was that a significant drop in the current was not seen after the ideal deposition thickness was reached (4 layers). Also, the films showed a higher photoresponse and more ideal PEC transients. This is expected as the Mo back contact has lower overall resistance (0.55 Ω/sq) than the FTO glass (7 Ω/sq). The Mo substrates were also placed in the reaction flask in the presence of sulfur, which could have induced the production of MoS_2. If a thin layer of MoS_2, with suitable properties (p-MoS_2), forms at the semiconductor/substrate interface, it can provide a good ohmic contact between the back contact and the absorbing layer.[35] The formation of this could have been possible and the enhanced contact would have reduced the recombination rate of minority carriers.
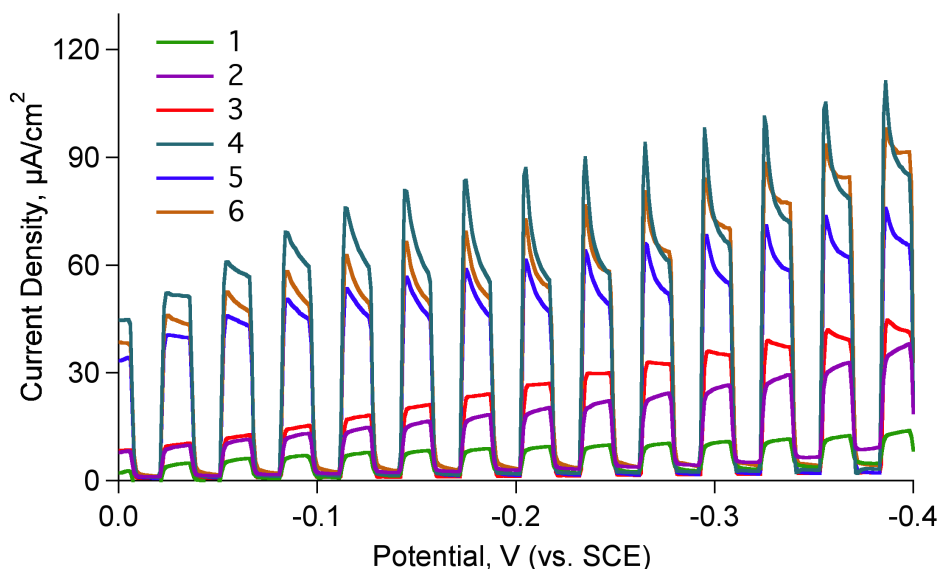
Figure 4.5. The PEC measurements of CZTS deposited on Mo coated glass. Labels 1-6 represent the number of times the substrate was placed in the reaction vial corresponding to the number of layers deposited.

Upon illumination, a sharp peak in the transient is visible, this type of overshoot occurs due to a build-up of trapped charge, as there is an imbalance in electron-hole mobility. The sharp rise is followed by steep decay, indicative of a slow detrapping rate in the system. When the light is turned off, the drop in current is followed by a steady state. This steady state is merely visible for samples deposited on FTO (Figure 4.4). The decay kinetics indicates that the CZTS NCs deposited on Mo had a faster rate of charge extraction vs. ones fabricated on FTO.

The surface morphology of the films deposited on the Mo substrate were analyzed using SEM (Figure 4.6).
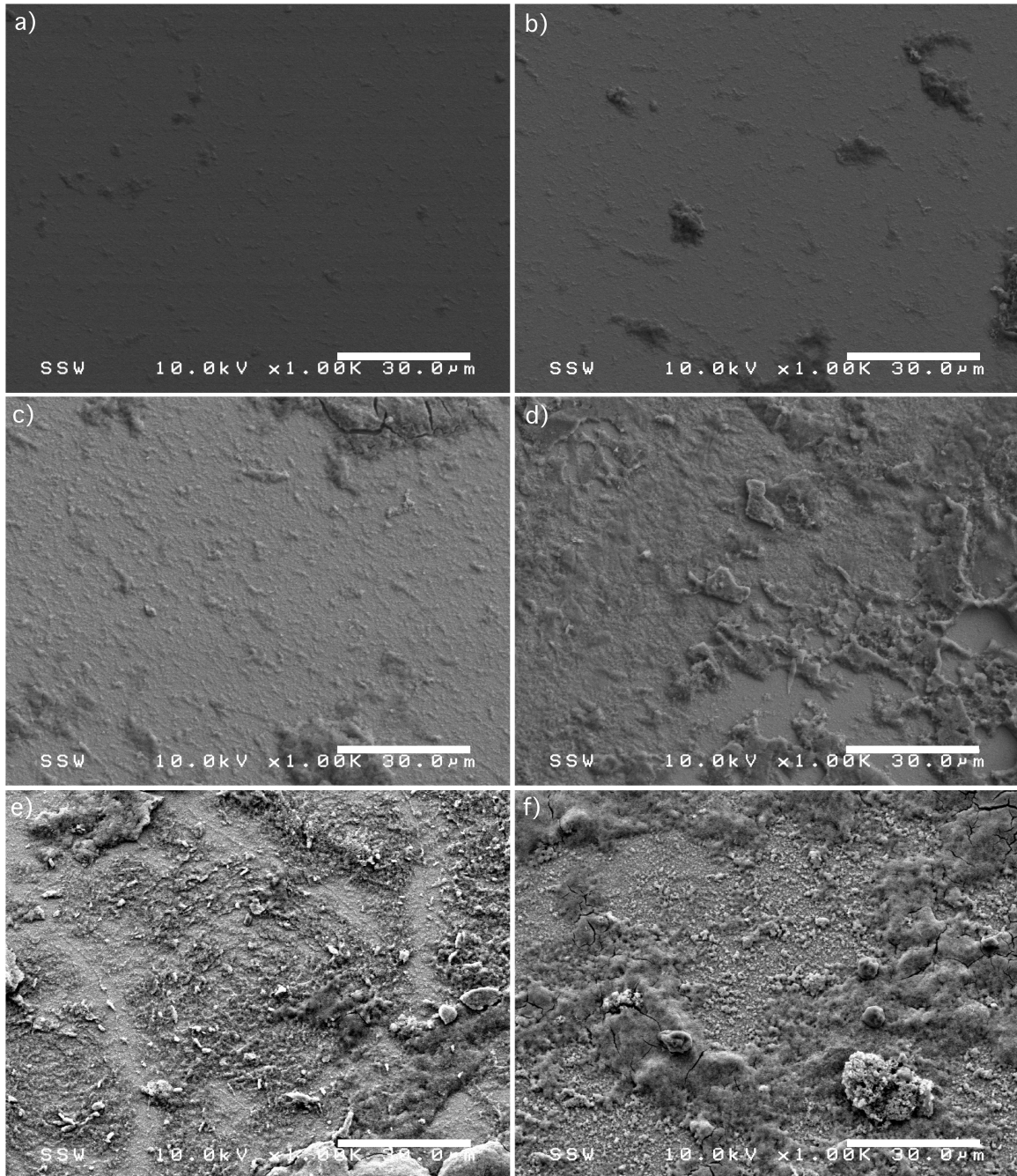
Figure 4.6. SEM images of CZTS thin films on a Mo substrate. The 1-layer (a), 2-layer (b), 3-layer (c), 4-layer (d), 5-layer (e) and 6-layer (f) depositions were done using the dip-coating method.

The 1 (Figure 4.6 (a)) and 2 (Figure 4.6 (b)) layers appeared to have the most uniform and smooth surfaces. As the layer-by-layer depositions increased (Figure 4.6 (c) – (f)) the surface roughness of the films also increased.

As shown in Figure 4.6 (e) and (f), various areas of the film appear dense and this can

be attributed to a build-up of NCs. Besides the temperature, there is no control over various parameters such as speed, amount of CZTS deposited and back contact alignment; therefore, as CZTS adheres onto the substrate, non-uniformities and projecting regions become more apparent with the growing films. The lack of control also results in inconsistencies.

Considering CZTS thin-films have an ideal thickness of 1-2μm the cross-section of the 5 and 6 layered films were detected (Figure 4.7). As shown there are density variations throughout both films and the addition of the 6th layer led to a thickness difference of 3.5 times. It is not only important for a sample to have a constant thickness throughout the majority of the film but also control within depositions, to ensure experimental consistency.
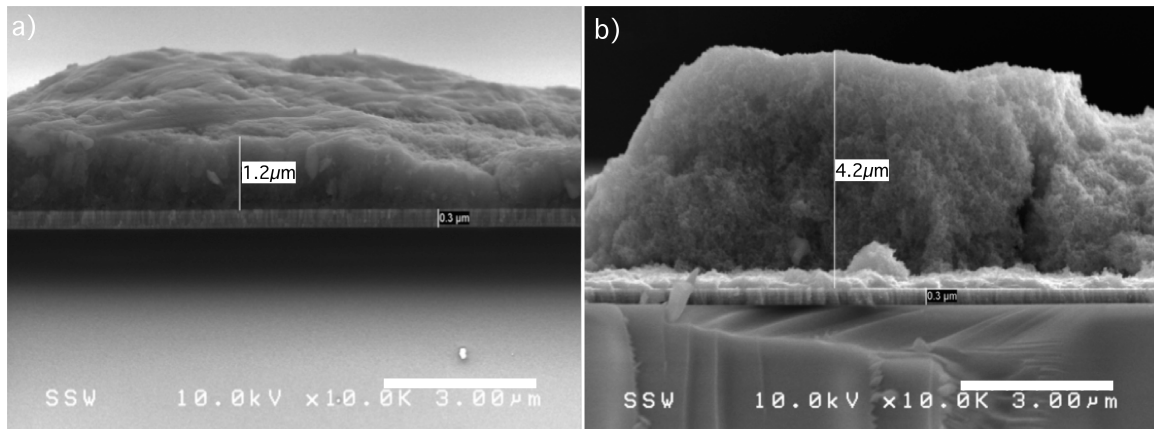
Figure 4.7. Cross section of the 5-layer (a) and 6-layer CZTS films on Mo-coated substrates.

Despite this technique resulting in films in which were more compact and less porous than the dropcast samples, the lack of deposition control and uneven surface were not ideal for device fabrication. High levels of controllability are essential during film formation. Another drawback of this method is that the remaining CZTS NCs in solution, which did not deposit onto the substrate, were no longer required and discarded. For example, the 4-layered film achieved the highest photocurrent; however, it also required 4 batches of CZTS to be synthesized, making the majority of the sample waste and the process costly. The use of this method meant that the low cost associated with the one-pot synthesis was no longer applicable, as it required several batches to be made. If this approach had produced a dramatic increase in photocurrent, in reference to the dropcast method, then the final efficiency could have outweighed the costs. Having established that an important factor in our fabrication is to maintain low levels of cost and waste, another method of deposition was

explored.

4.4.2. Thin Film Fabrication using the Joule Heating Method

Joule heating was used as a method for drying the CZTS thin films upon dropcast. PEC measurements were taken of the CZTS samples deposited onto FTO & Mo-coated glass, after dispersion in either ethylene glycol (EG) or isopropanol. The viscosity of EG is ~8x greater than that of isopropanol,[36] which means it can take up to several days to dry in open air; however using joule heating this can be accomplished in minutes.

Figure 4.8 displays the photocurrent of the Mo-coated thin films, which were determined upon drying using a constant current of 0.8A or 1.0A. In reference to the isopropanol samples, the photocurrent range, between -0.2V and -0.4V, using 0.8A and 1.0A were 31-32 $\mu A/cm^2$ and 17-18 $\mu A/cm^2$, respectively. A noticeable drop in the photoresponse is seen (31-32 $\mu A/cm^2$ to 17-18 $\mu A/cm^2$) with the increase in the applied current. The range of photoresponse for the samples dispersed in EG were 32-33 $\mu A/cm^2$ (0.8A) and 18-19 $\mu A/cm^2$ (1.0A). A similar trend is noted, in which a sudden drop in photocurrent is seen with the increase in applied current.

Figure 4.8. The PEC measurements of the CZTS films dispersed in (a) Isopropanol and (b) EG dried on Mo-coated substrates, at an applied current of 0.8A and 1.0A.

Similar measurements were done using FTO as the substrate (Figure 4.9). Lower currents were applied (0.3A and 0.5A) because the surface resistivity of the Mo coated glass is 0.55 Ω/sq and for FTO it is approximately 7 Ω/sq. This allows for more efficient transformation of heat in a shorter period of time. Despite the lower currents, CZTS deposited on Mo-glass substrates still required a much longer joule heating time vs. ones deposited on FTO.

When using isopropanol as the dispersion solvent, the range of photoresponse

between -0.2V and -0.4V, were 22-24 µA/cm^2 (0.3A) and 25-27 µA/cm^2 (0.5A). The photocurrent range for the EG samples were 48-49 µA/cm^2 and 30-31 µA/cm^2 using an applied current of 0.3A and 0.5A, respectively. Parallel to data shown in Figure 4.8, a decrease in the current density is seen with the increase in applied current. The samples dispersed in isopropanol displayed lower photocurrents than ones dispersed in EG. Overall, the latter films contained the highest photocurrent of all of the other samples. This could be because EG has been found to have a high contact angle on FTO substrates.[37] The better adhesion would result in greater charge transfer and in turn a higher photoresponse.
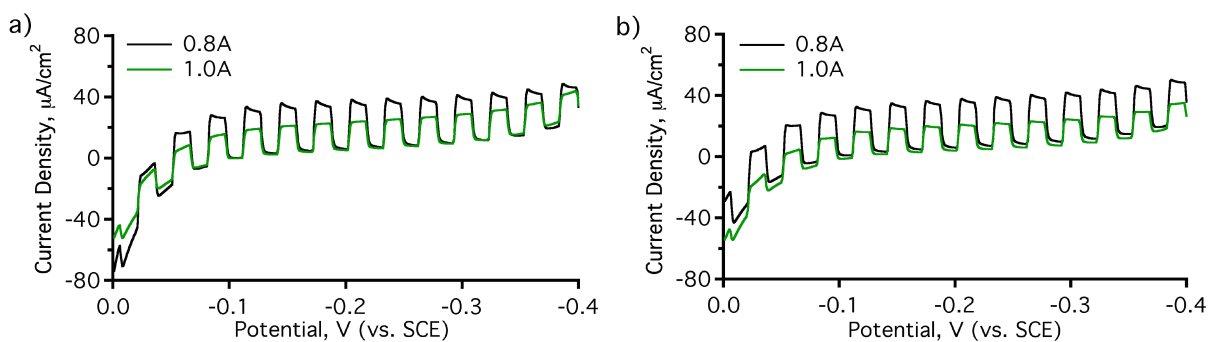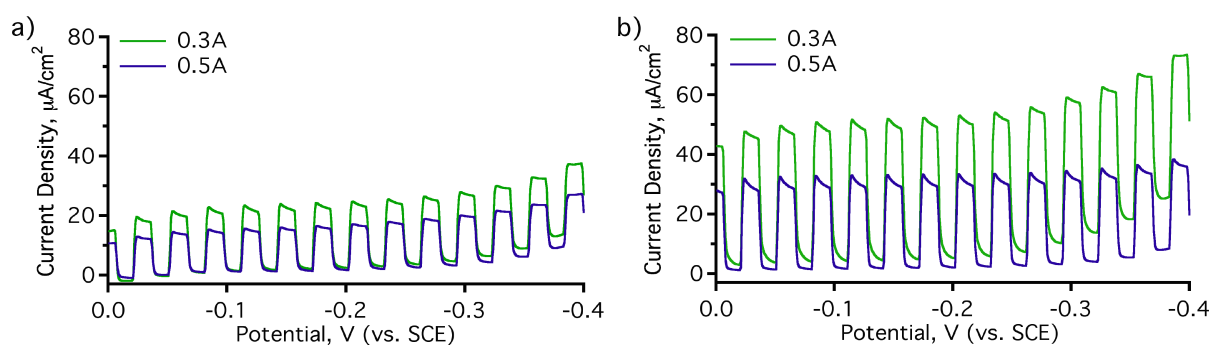

Figure 4.4. The PEC measurements of the CZTS films dispersed in (a) Isopropanol and (b) EG dried on FTO substrates, at an applied current of 0.8A and 1.0A.

To further assess the trends seen in the photoresponse, relative to applied current, surface analysis was done using SEM. The images shown in Figure 4.10 correlates with the films deposited on FTO using EG as the solvent. Figure 4.10 (a) displays the photocurrent transients of the films synthesized using a constant current of 0.3A, 0.4A and 0.5A. The only difference between Figure 4.10 (a) and Figure 4.10 (b) is the addition of the photoresponse of the film dried at an applied current of 0.4A (41-42 µA/cm^2). This was done to further confirm the trend seen in the PEC measurements previously shown. Figure 4.10 (b)-(d), correspond to the synthesized films using a constant current of 0.3A, 0.4A and 0.5A, respectively. The pattern seen in the morphology of the films is an increase in the number of cracks with the increase in current. Overall the number of islands separated by cracking increases. In relation to the PEC measurements the increase in the density of cracks could be the primary reason for the gradual decrease in photocurrent for samples deposited at 0.3A, 0.4A and 0.5A, respectively.
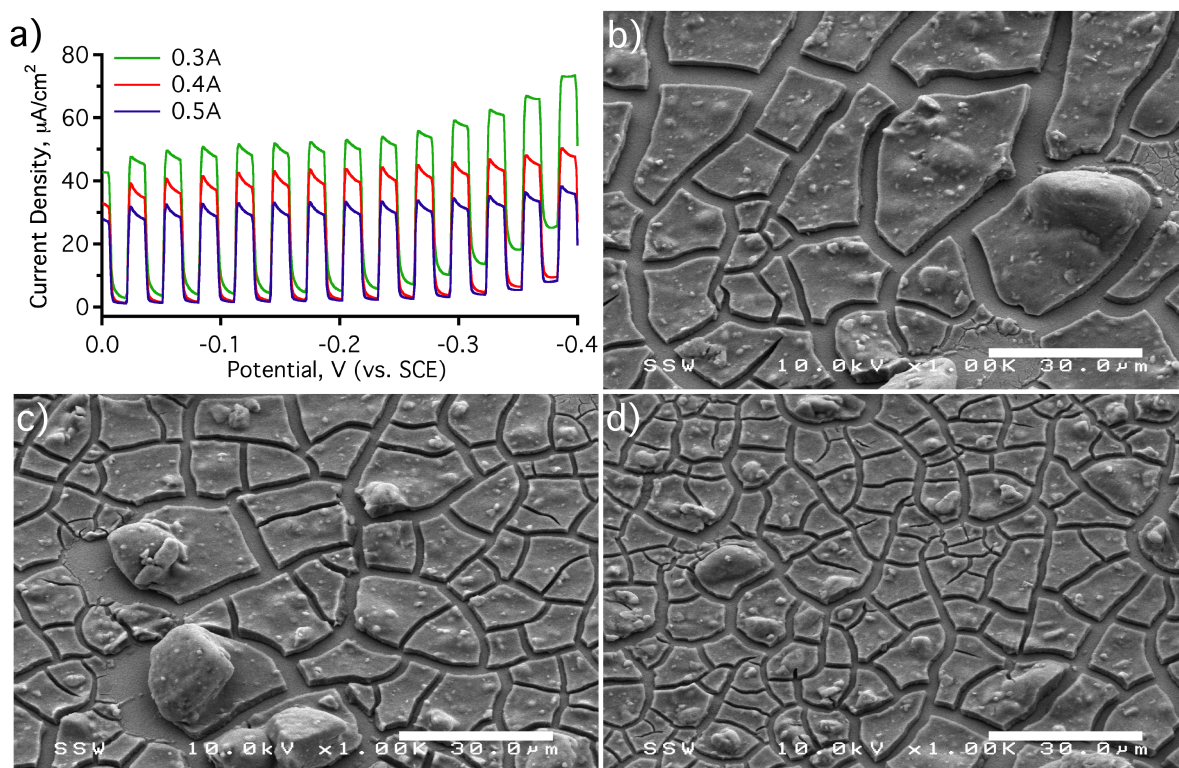
Figure 4.10. CZTS thin films dried at different applied currents. The PEC measurements of the samples dispersed in EG and deposited on FTO at an applied current of 0.3A, 0.4A and 0.5A is shown in (a). The SEM images of the films fabricated at an applied current of (b) 0.3A, (c) 0.4A and (d) 0.5A are also demonstrated.

It is likely that the rise in temperature induces thermal and mechanical stresses due to the different coefficients of thermal expansion of the materials; in turn, the higher the applied current, the greater this stress. This is could be the reason why the increase in film cracking and decrease in photocurrent is seen, with the increase in applied current. Joule heating of the films triggered the formation of cracks. This technique did not cause a photocurrent enhancement, greater than the photoresponse using the dropcast method. With this regard a final deposition technique, using spin-coating, was investigated.

4.4.3. Thin Film Fabrication using the Spin-coating Method

The last method of deposition was via use of spin-coating. This method allowed for a uniform deposition of the CZTS NCs, which were dispersed in iPrOH. Figure 4.11 shows the PEC measurements for the spin-coated samples on multiple FTO and Mo substrates. The range of photocurrent for CZTS deposited on FTO and Mo were between 69-75 $\mu A/cm^2$ and 60-77 $\mu A/cm^2$, respectively. The photocurrent obtained using this technique exceeded that of

the dropcast method. The thickness and overall morphology for each of the multiple samples were consistent and highly reproducible, making it an appealing process for thin film fabrication. Isopropanol was the solvent of choice as its low surface tension (0.021 N/m)[38] allows it spread over the surface of a spinning substrate easily and prior to evaporation; thus creating a more uniform film.
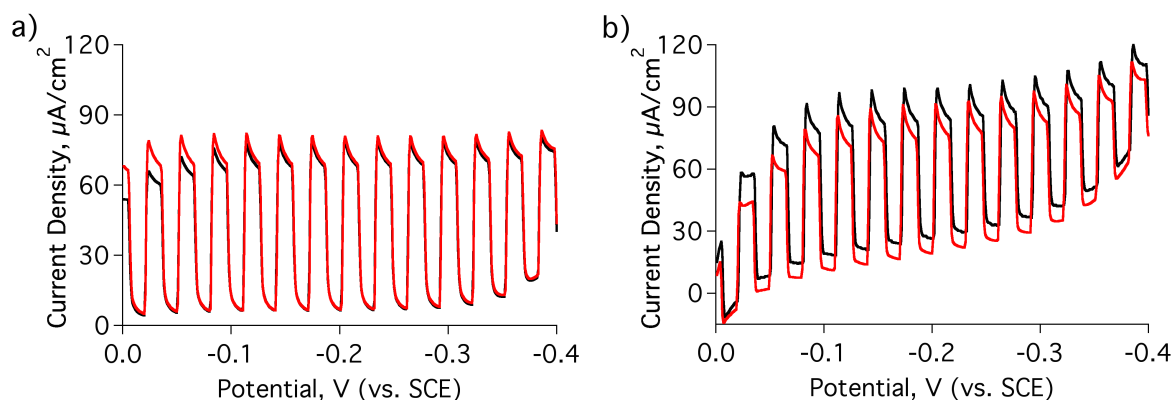

Figure 4.11. The PEC measurements of the CZTS films deposited via spin-coating on (a) FTO and (b) Mo-coated substrates. The black and red colors represent the measurements taken of two different samples.

The SEM images in Figure 4.12 illustrate the surface topography of the thin films deposited on FTO (Figure 4.12 (a)) and Mo (Figure 4.12 (b)).
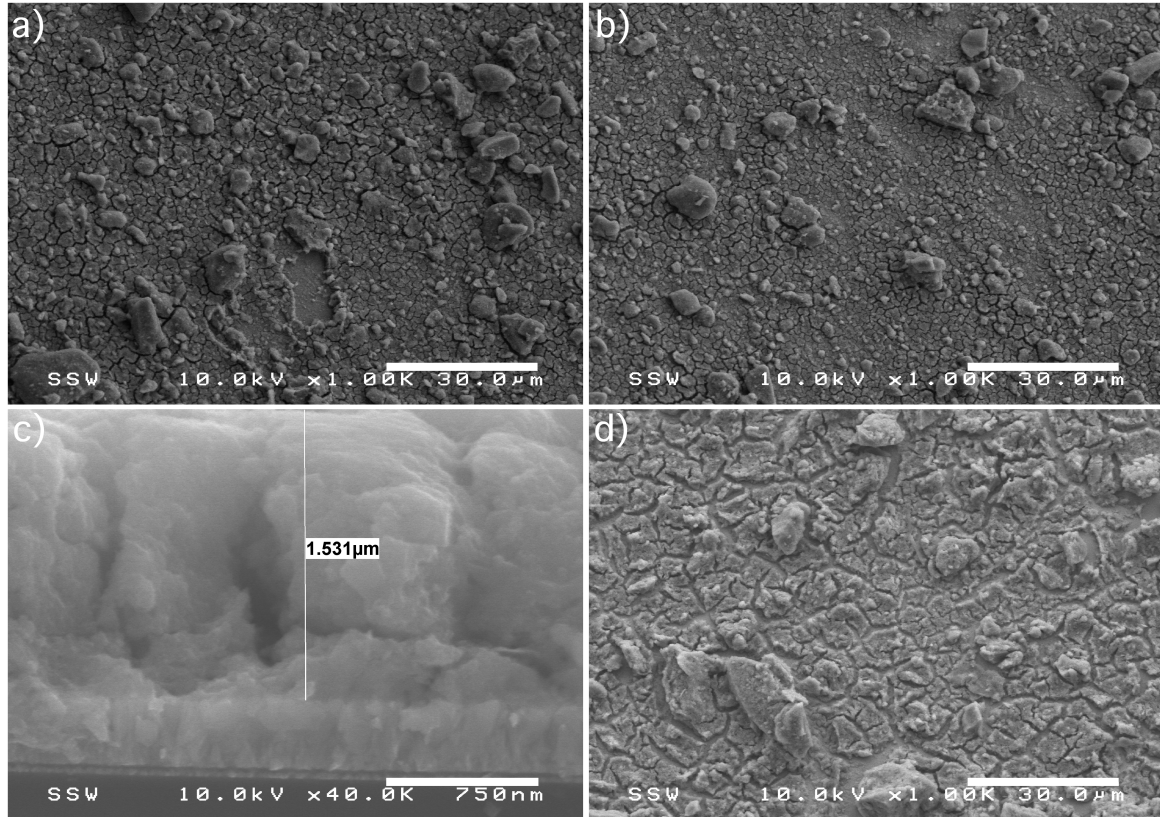
Figure 4.12. SEM images of the CZTS films deposited on (a) Mo and (b,d) FTO. The films fabricated using (a,b,c) spin-coating and (d) dropcast are shown. The cross-section of the spin-coated sample is demonstrated in (c).

The thickness of the films was approximately 1.5 μm, which is in alignment with the desired CZTS thickness of 1-2μm. In comparison to the dropcast method (Figure 4.12 (d)) there is a drastic decrease in the number of cracks. As previously indicated a more uniform film with less defects and grain boundaries will facilitate greater charge transfer from the bulk of the material to the surface. This is primarily because of reduced electron trapping at the surface.

4.4.4. Full Device

Once optimization of the absorbing layer was completed, the subsequent layers were deposited and the opto-electronic properties of the final device were measured. In this investigation, the final device was fabricated via spin-coating the CZTS layer. To induce more desirable films, the samples were annealed in the presence of sulfur. A chemical bath deposition was used to deposit the CdS buffer layer and by means of ALD the final device was fabricated via layering AZO and ZnO.

Figure 4.13 shows the IV curve of the full device under illumination and in the dark. This was plotted upon varying the applied voltage while measuring the current. The device efficiency obtained was 0.0003% (J_{sc}= 3.65 μA/cm², V_{oc} = 0.468V, FF=45%).
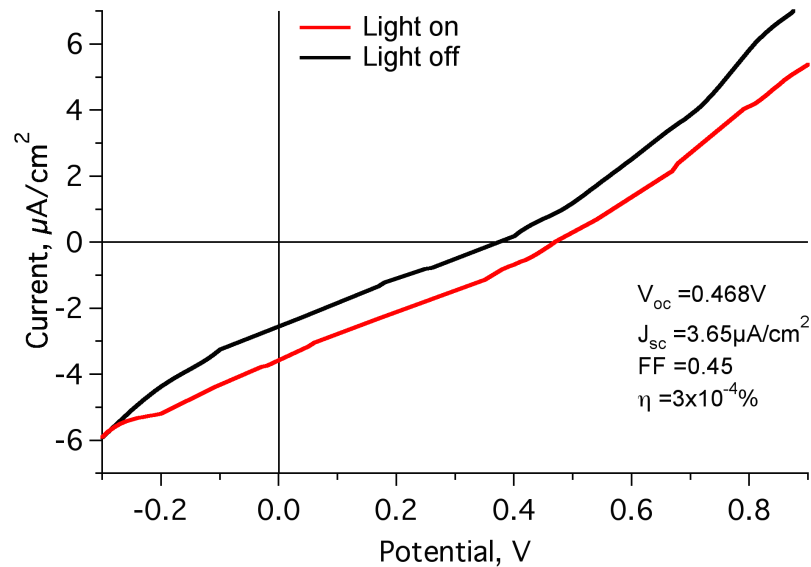
Figure 4.13. Full Device tested under illumination and in the dark.

The low efficiency could have resulted from several factors, including optical and electrical losses. Optical losses refers to light that is lost via reflection. Although majority of light hitting the device is absorbed some of it can be reflected. Experimentally, this could have contributed to the low device efficiency as it causes a reduction in the number of generated electron-hole pairs. To reduce this effect anti-reflection coatings are predominately applied.[39-41] The application of this requires further investigation; however, could have been advantageous in this study.

The second contributing factor for the poor performance can be vastly attributed to electrical losses as a result of imperfections and secondary phases. Certain crystal defects and impurity atoms within the layers can lead to traps and grain boundaries. This would then lead to recombination, which would reduce the J_{sc} and further impact the V_{oc}. Although secondary phases were not detected using Raman (Figure 3.3, Chapter 3), the samples were later annealed in a sulfur atmosphere, which could have induced their formation.

As shown in a publication by Ahmed et al. when the sulfurization parameters are not optimized secondary phases such as Cu_2S and Cu_2SnS_3 phases can form.[42] Phases with small

band gaps, such as $Cu_{2-x}S$ and $Cu_{2-x}SnS_3$, would enhance recombination and cause frequent shunting.[43-44] The formation of ZnS, which has a large band gap (3.5-3.8 eV)[45], may contribute to a devices' low current density, as it could absorb a lights shorter wavelengths;[5] however, as stated in Chapter 3, this contribution is not detrimental, as it does not behave like a recombination center.[5, 46]

Resistive effects can cause frequent shunting within a device. The series resistance (R_s) is caused by three factors: (1) The first being the resistance of the ohmic contact between the coated substrate and the absorbing layer, (2) the resistance of the p- and n-type layers to the flow of minority carriers, (3) the resistance of the top and bottom contacts.[47] The larger the R_s value, the smaller the maximum power output and FF. Secondary phases can increase the R_s, primarily when located at the p-n junction or near the back contact.

The shunt resistance (R_{sh}) can also affect the electronic properties of a final device. R_{sh} provides an alternate path for the photocurrent, thereby minimizing the flow of minority carriers through the device junction. Secondary phases, metal oxides and certain defects would act as current barriers and recombination centers, resulting in a decrease in the R_{sh}. Conductive secondary phases, such as $Cu_{2-x}S$ and $Cu_{2-x}SnS_3$ have been shown to cause shunting pathways and have a large impact on the solar cells J_{sc}.[46] Recombination in the bulk and or at the surface of the material could have caused losses in the J_{sc} and V_{oc}. Lastly defects in the other layers could have assisted in the low efficiency.

4.4. Conclusions

Different deposition techniques were tested as dropcasting followed by air-drying resulted in an uneven surface, presence of cracks and overall low reproducibility. The objective of these studies was to improve the photocurrent of the samples without having to compromise the cost. The deposition methods used included, dip-coating, joule heating and spin-coating.

For the dip-coating technique the 3-layer deposition on FTO showed the highest photocurrent (65-76 $\mu A/cm^2$), while the photoresponse diminished upon additional depositions. As for Mo, the 4-layer film had the highest photoresponse (85-108 $\mu A/cm^2$) followed by the 6th (69-93 $\mu A/cm^2$) and 5th (60-73 $\mu A/cm^2$). The monolayer and bilayer for both samples were likely too thin to completely block the back contact and as a result showed the lowest photoresponse. The drawbacks of this technique were the lack of deposition

control, uneven coatings and the high amounts of waste. The synthesis of multiple batches also increased the overall cost associated with the process.

The second deposition method explored was Joule heating. This technique was used to dry the samples, post-dropcast, via heat transfer from the coated back contact. The PEC measurements from the samples deposited on both FTO & Mo-coated substrates showed a similar trend in that a sudden drop in the photocurrent was seen with the increase in applied current. The SEM images indicated an increase in the number of surface cracks, which was most likely due to enhanced thermal and mechanical stresses, via the increase in applied current. These finding implied that the decrease in current density for the PEC results, were due to the increase in film cracking, as a result of stress.

The final deposition technique investigated was spin-coating. The range of photocurrent for the samples deposited on FTO and Mo were between 69-75 $\mu A/cm^2$ and 60-77 $\mu A/cm^2$, respectively. The high reproducibility and relatively more uniform film (vs. dropcast films) resulted in further fabrication of these films towards a full device.

Upon sulfurization of the CZTS films, the layers were coated with CdS, AZO and ZnO. The full device gave rise to an efficiency of 0.0003% (J_{sc}= 3.65 $\mu A/cm^2$, V_{oc} = 0.468V, FF=45%). The low efficiency could have resulted from optical and/or electrical losses. As these devices did not contain an anti-reflection coating, some of the light hitting the device could have been reflected and lost. Imperfections and secondary phases could have lead to the low efficiency and ultimately impacted the J_{sc}, V_{oc} and FF.

4.5. References

1.   Eslamian, M., Spray-on Thin Film PV Solar Cells: Advances, Potentials and Challenges. *Coatings* **2014,** *4*, 60.

2.   Wengeler, L.; Schmitt, M.; Peters, K.; Scharfer, P.; Schabel, W., Comparison of large scale coating techniques for organic and hybrid films in polymer based solar cells. *Chemical Engineering and Processing* **2013,** *68*, 38.

3.   Krebs, F. C., Fabrication and processing of polymer solar cells: A review of printing and coating techniques. *Solar Energy Materials and Solar Cells* **2009,** *93*, 394.

4.   Scragg, J. J.; Kubart, T.; Wätjen, J. T.; Ericson, T.; Linnarsson, M. K.; Platzer-Björkman, C., Effects of Back Contact Instability on Cu_2ZnSnS_4Devices and Processes.

Chemistry of Materials **2013,** *25*, 3162.

5.   Scragg, J. J., *Copper Zinc Tin Sulfide Thin Films for Photovoltaics: Synthesis and Characterisation by Electrochemical Methods.* Springer: Berlin, 2011.

6.   Todorov, T. K.; Tang, J.; Bag, S.; Gunawan, O.; Gokmen, T.; Zhu, Y.; Mitzi, D. B., Beyond 11% Efficiency: Characteristics of State-of-the-Art $Cu_2ZnSn(S,Se)_4$ Solar Cells. *Advanced Energy Materials* **2013,** *3*, 34.

7.   Shin, B.; Gunawan, O.; Zhu, Y.; Bojarczuk, N. A.; Chey, S. J.; Guha, S., Thin film solar cell with 8.4% power conversion efficiency using an earth-abundant Cu_2ZnSnS_4 absorber. *Progress in Photovoltaics: Research and Applications* **2013,** *21*, 72.

8.   Wang, W.; Winkler, M. T.; Gunawan, O.; Gokmen, T.; Todorov, T. K.; Zhu, Y.; Mitzi, D. B., Device Characteristics of CZTSSe Thin-Film Solar Cells with 12.6% Efficiency. *Advanced Energy Materials* **2014,** *4*, 1301465.

9.   Todorov, T. K.; Reuter, K. B.; Mitzi, D. B., High-Efficiency Solar Cell with Earth-Abundant Liquid-Processed Absorber. *Advanced Materials* **2010,** *22*, E156.

10.   Makhlouf, A. S. H.; Tiginyanu, I., *Nanocoatings and Ultra-Thin Films: Technologies and Applications.* Elsevier: Cambridge, 2011.

11.   Joshi, S. V.; Sundararajan, G., Lasers for Metallic and Intermetallic Coatings. In *Lasers in Surface Engineering*, Dahotre, N. B., Ed. ASM International: Ohio, 1998, 121.

12.   Brinker, C. J., Dip Coating. In *Chemical Solution Deposition of Functional Oxide Thin Films*, Schneller, T., Waser, R., Kosec, M., Payne, D. , Ed. Springer: Wien, 2013, 233.

13.   Sun, Y.; Zong, K.; Zheng, H.; Wang, H.; Liu, J.; Yan, H.; Zhu, M., Ethylene glycol-based dip coating route for the synthesis of Cu_2ZnSnS_4 thin film. *Materials Letters* **2013,** *92*, 195.

14.   Maheshwari, B. U.; Kumar, V. S., Phase transformation of solution-based p-type Cu_2ZnSnS_4 thin film: applicable for solar cell. *International Journal of Energy Research* **2015,** *39*, 771.

15.   Rampino, S.; Annoni, F.; Bronzoni, M.; Calicchio, M.; Gombia, E.; Mazzer, M.; Pattini, F.; Gilioli, E., Joule heating-assisted growth of $Cu(In,Ga)Se_2$ solar cells. *Journal of Renewable and Sustainable Energy* **2015,** *7*, 013112.

16.   Sarswat, P. K.; Free, M. L., Demonstration of a sol–gel synthesized bifacial CZTS photoelectrochemical cell. *Physica Status Solidi (A)* **2011,** *208*, 2861.

17.   Wang, J.; Zhang, P.; Song, X.; Gao, L., Cu_2ZnSnS_4 thin films: spin coating synthesis and photoelectrochemistry. *Royal Society of Chemistry Advances* **2014,** *4*, 21318.

18.   Xin, X.; He, M.; Han, W.; Jung, J.; Lin, Z., Low-Cost Copper Zinc Tin Sulfide Counter Electrodes for High-Efficiency Dye-Sensitized Solar Cells. *Angewandte Chemie International Edition* **2011,** *50*, 11739.

19.   Ki, W.; Hillhouse, H. W., Earth-Abundant Element Photovoltaics Directly from Soluble Precursors with High Yield Using a Non-Toxic Solvent. *Advanced Energy Materials* **2011,** *1*, 732.

20.   Katagiri, H., Sulfurization of Physical Vapor-Deposited Precursor Layers. In *Copper Zinc Tin Sulfide-Based Thin-Film Solar Cells*, Ito, K., Ed. Wiley: Chichester, 2015, 181.

21.   Zhou, H.; Hsu, W.-C.; Duan, H.-S.; Bob, B.; Yang, W.; Song, T.-B.; Hsu, C.-J.; Yang, Y., CZTS nanocrystals: a promising approach for next generation thin film photovoltaics. *Energy & Environmental Science* **2013,** *6*, 2822.

22.   Parameshwari, P. M.; Naik, K. G., Effect of Cd/S molar ratio on the optical and electrical properties of spray deposited CdS thin films. In *Physics of Semiconductor Devices: 17th International Workshop on the Physics of Semiconductor Devices 2013*, Jain, V. K.; Verma, A., Eds. Springer: Switzerland, 2013, 347.

23.   Ito, K., An Overview of CZTS-Based Thin-Film Solar Cells. In *Copper Zinc Tin Sulfide-Based Thin-Film Solar Cells*, Ito, K., Ed. Wiley: Chichester, 2015, 1.

24.   Oladeji, I. O.; Chow, L., Optimization of chemical bath deposited cadmium sulfide thin films. *Journal of the Electrochemical Society* **1997,** *144*, 2342.

25.   Janotti, A.; Van de Walle, C. G., Fundamentals of zinc oxide as a semiconductor. *Reports on Progress in Physics* **2009,** *72*, 126501.

26.   Dhakal, T. P.; Peng, C. Y.; Tobias, R. R.; Dasharathy, R.; Westgate, C. R., Characterization of a CZTS thin film solar cell grown by sputtering method. *Solar Energy* **2014,** *100*, 23.

27.   Yoo, J.; Lee, J.; Kim, S.; Yoon, K.; Park, I. J.; Dhungel, S. K.; Karunagaran, B.; Mangalaraj, D.; Yi, J., High transmittance and low resistive ZnO:Al films for thin film solar cells. *Thin Solid Films* **2005,** *480–481*, 213.

28.   Rovelli, L.; Tilley, S. D.; Sivula, K., Optimization and Stabilization of

Electrodeposited Cu_2ZnSnS_4 Photocathodes for Solar Water Reduction. *American Chemical Society Applied Materials & Interfaces* **2013,** *5*, 8018.

29.   Niu, W.; Li, X.; Karuturi, S. K.; Fam, D. W.; Fan, H.; Shrestha, S.; Wong, L. H.; Tok, A. I. Y., Applications of atomic layer deposition in solar cells. *Nanotechnology* **2015,** *26*, 064001.

30.   Ericson, T.; Scragg, J. J.; Hultqvist, A.; Watjen, J. T.; Szaniawski, P.; Torndahl, T.; Platzer-Bjorkman, C., Zn(O, S) Buffer Layers and Thickness Variations of CdS Buffer for Cu_2ZnSnS_4 Solar Cells. *The IEEE Journal of Photovoltaics* **2014,** *4*, 465.

31.   Van Delft, J.; Garcia-Alonso, D.; Kessels, W., Atomic layer deposition for photovoltaics: applications and prospects for solar cell manufacturing. *Semiconductor Science and Technology* **2012,** *27*, 074002.

32.   Kodigala, S. R., *Thin Film Solar Cells From Earth Abundant Materials: Growth and Characterization of $Cu_2(ZnSn)(SSe)_4$ Thin Films and Their Solar Cells*. Elsevier: Burlington, 2013.

33.   Ghosh, T.; Prelas, M., *Energy Resources and Systems: Volume 2: Renewable Resources*. Springer: Netherlands, 2011.

34.   Lei, B.; Hou, W. W.; Li, S.-H.; Yang, W.; Chung, C.-H.; Yang, Y., Cadmium ion soaking treatment for solution processed $CuInS_xSe_{2-x}$ solar cells and its effect on defect properties. *Solar Energy Materials and Solar Cells* **2011,** *95*, 2384.

35.   Chelvanathan, P.; Hossain, M. I.; Husna, J.; Alghoul, M.; Sopian, K.; Amin, N., Effects of transition metal dichalcogenide molybdenum disulfide layer formation in copper–zinc–tin–sulfur solar cells from numerical analysis. *Japanese Journal of Applied Physics* **2012,** *51*, 1.

36.   Pandley, R. K.; Sahu, S. N.; Chandra, S., *Handbook of Semiconductor Electrodeposition*. CRC Press: New York, 1996.

37.   Bard, A.; Lee, H. C.; Leonard, K.; Park, H. S.; Wang, S., Rapid Screening Methods in the Discovery and Investigation of New Photocatalyst Compositions. In *Photoelectrochemical Water Splitting: Materials, Processes and Architectures*, Lewerenz, H. J.; Peter, L., Eds. The Royal Society of Chemistry: Cambridge, 2013, 132.

38.   *Isopropyal Alcohol (2-Propanol)*. CAS No. 67-63-0; LabChem Inc.: Philadelphia, 2012.

39.   Kuo, S.-Y.; Hsieh, M.-Y., Efficiency enhancement in Cu_2ZnSnS_4 solar cells with subwavelength grating nanostructures. *Nanoscale* **2014,** *6*, 7553.

40.   Zhao, J.; Wang, A.; Altermatt, P.; Green, M. A., Twenty-four percent efficient silicon solar cells with double layer antireflection coatings and reduced resistance loss. *Applied Physics Letters* **1995,** *66*, 3636.

41.   Jackson, P.; Hariskos, D.; Lotter, E.; Paetel, S.; Wuerz, R.; Menner, R.; Wischmann, W.; Powalla, M., New world record efficiency for $Cu(In,Ga)Se_2$ thin-film solar cells beyond 20%. *Progress in Photovoltaics: Research and Applications* **2011,** *19*, 894.

42.   Ahmed, S.; Reuter, K. B.; Gunawan, O.; Guo, L.; Romankiw, L. T.; Deligianni, H., A high efficiency electrodeposited Cu_2ZnSnS_4 solar cell. *Advanced Energy Materials* **2012,** *2*, 253.

43.   Flammersberger, H. Experimental study of Cu_2ZnSnS_4 thin films for solar cells. *MSc. dissertation*. Uppsala University: Sweden, 2010.

44.   Berg, D. M.; Dale, P. J., Kesterites. In *Copper Zinc Tin Sulfide-Based Thin-Film Solar Cells*, Wiley: Chichester, 2015, 107.

45.   Nadeem, M.; Ahmed, W., Optical properties of ZnS thin films. *Turkish Journal of Physics* **2000,** *24*, 651.

46.   Fairbrother, A.; García-Hemme, E.; Izquierdo-Roca, V.; Fontané, X.; Pulgarín-Agudelo, F. A.; Vigil-Galán, O.; Pérez-Rodríguez, A.; Saucedo, E., Development of a Selective Chemical Etch To Improve the Conversion Efficiency of Zn-Rich Cu_2ZnSnS_4 Solar Cells. *Journal of the American Chemical Society* **2012,** *134*, 8018.

47.   Wolf, M.; Rauschenbach, H., Series resistance effects on solar cell measurements. *Advanced energy conversion* **1963,** *3*, 455.

Chapter 5. Conclusions and Future Perspectives

The aim of this project was to compositionally optimize the CZTS NCs and thereafter synthesize and fabricate thin films via a low energy and cost method. The first part of the project focused on determining the effects of stoichiometry on CZTS crystallinity and overall film quality. This was done by initially determining the precursor ratios required to yield the selective final compositions. Upon optimization of the stoichiometry, alternative deposition methods were explored using the Cu-poor, Zn-rich composition. The influence of the fabrication techniques (dip-coating, joule-heating and spin-coating) on the electronic properties of the films was determined via PEC measurements. The spin-coated samples were then selected for device fabrication.

The preliminary results of a device with a working p-n junction yielded a low efficiency. In addition to the optimization of the absorber layer, further work on the subsequent layers is required. The sulfurization conditions can vastly impact a devices efficiency. Although in literature it has consistently been shown to lead to high quality films, the optimization of its parameters, in accordance with the CZTS film, is essential. The lack of this investigation can enhance the formation of secondary phases and ultimately affect a devices efficiency.

Future research should also explore the impact and optimization of the subsequent layers. CdS has been commonly used as the n-type buffer layer for CZTS; however, its toxicity raises environmental concerns. Also, as previously indicated the band gap of CdS is 2.42 eV, which causes some of the photons hitting the sample to be absorbed before reaching the CZTS layer. Investigations using an alternative, such as Zn(O,S) have been reported, but require optimization. The replacement of this layer could deem advantageous for future device fabrication and application.

Lastly, the deposition conditions for the i-ZnO and Al doped ZnO layers need to be optimized as the temperature and deposition time can vastly affect their sheet resistance. Further investigations into the aforementioned properties/conditions, followed by a final anti-reflection coating, can improve the overall device performance.

Curriculum Vitae

Name:	Saghar Khoshmashrab
Post-secondary Education and Degrees:	University of Toronto Ontario, Canada 2006-2011 BSc Honors
	The University of Western Ontario London, Ontario, Canada 2013-2015 MSc
Honours and Awards:	Western Graduate Research Scholarship 2013-2014, 2014-2015
Volunteer Experience:	March Break Open House 2014
	Elementary School Outreach 2014
	Thames Valley Science & Engineering Fair 2015
	March Break Open House 2015
Related Work Experience	Teaching Assistant The University of Western Ontario 2013-2015

Publications:

Effects of Cu content on the photoelectrochemistry of Cu_2ZnSnS_4 nanocrystal thin films. S. Khoshmashrab, M.J. Turnbull, D. Vaccarello, Y. Nie, S. Martin, D.A. Love, P.K. Lau, X. Sun*, Z. Ding*. Electrochimica Acta. 2015, 162, 176-184.

Controlling Cu_2ZnSnS_4 photocatalytic ability through alterations in sulfur availablility. M.J. Turnbull, S. Khoshmashrab, Z. Wang, R. Harbottle, T.K. Sham*, Z. Ding*. Catalysis Today. 2015, In Press.